Fe-ZSM-5 and Fe-SAPO-34 Catalysts for Low-Temperature Selective Catalytic Reduction of NO_X by NH_3

Lisa Leganger Landfald

Master's Thesis

NTNU – Norwegian University of Science and Technology

February 2019

Abstract

Iron based catalysts supported by the zeolite ZSM-5 and the zeotypes conventional and hierarchical SAPO-34 were prepared to analyze the catalytic performance towards selective catalytic reduction (SCR) of NO_X by NH_3 at lower temperatures (450-250 ℃). The catalysts were prepared by different preparation routs and precursors: Incipient wetness impregnation with $Fe(NO_3)_3$, ion-exchange with $Fe(NO_3)_3$ and ion-exchange in an inert atmosphere with $FeCl_2$.

The samples were characterized by X-Ray Diffraction (XRD), inductively coupled plasma-mass spectrometer (ICP-MS), N_2 physisorption, temperature-programmed reduction of H_2 (H_2-TPR) and CO chemisorption. The NH_3-SCR was carried out in a packed bed reactor with a feed gas composition of 600 ppm NO, 600 ppm NH_3 and 10% O_2.

Different supports, preparation routes and precursors resulted in parameters that could influence the catalytic performance. Trends in the results indicate that to ion-exchange in an inert atmosphere with a Fe^{2+}-precursor could results in higher NO-conversion at lower temperatures. The catalysts which showed highest NO-conversion at lower temperatures were prepared by this preparation route, one supported by ZSM-5 and one by conventional SAPO-34. More presence of more monomeric iron as active sites for these catalysts could explain the increased conversion at lower temperatures.

The catalysts supported by hierarchical SAPO-34, was not found reported in literature, and could be a new catalysts for the NH_3-SCR. Activity measurements showed catalytic activation for NH_3-SCR. However, characterization results indicate that the pore structure could have collapsed upon the ion-exchange. Therefore, no conclusion of the impact of mesopores of the catalytic performance was made.

Sammendrag

Jernbaserte katalysatorer med zeolitten ZSM-5 og zeotypene konvensjonell SAPO-34 og hierarkisk SAPO-34 som bærere ble laget for å undersøke katalytiske opptredenen for selektiv katalytisk reduksjon av NO_X med NH_3 ved lavere temperaturer (250-450 ℃). Katalysatorene ble fremstilt med ulike fremgangsmåter og jernkilder: Tørr impregnering med $Fe(NO_3)_3$, ionebytte med $Fe(NO_3)_3$ og ionebytte i inert miljø med $FeCl_2$.

De ulike prøvene ble karakterisert ved X-Ray Diffraksjon (XRD), element analysen ICP-MS, N_2 fysisorpsjon, temperatureprogrammert reduksjon (TPR) av H_2 og CO kjemisorpsjon. Aktivitetsmålinger av NH_3-SCR var utført i en rørreaktor med en fødegass sammensatt av 600 ppm NO, 600 ppm NH_3 og 10 % O_2.

Ulike bærere, syntesemetoder og jernkilder resulterte i mange parametere som kunne påvirke den katalytiske utførelsen. Resultatene indikerte at det å ionebytte i inert miljø med Fe^{2+} som jernkilde kunne resultere i høyere NO-omsetting ved lavere temperaturer. De to katalysatorer som viste høyest NO-omsetting ved lave temperaturer var fremstilt ved denne metoden, en med ZSM-5-bærer og en med konvensjonell SAPO-34 bærer. Resultatene kan være en konsekvens av tilstedeværelse av mer monomeric jern som aktivt sete for disse katalysatorene.

Katalysatoren syntetisert med mesoporøse hierarkisk SAPO-34 som bærer, var ikke funnet rapportert i litteraturen, og kunne dermed være en ny katalysator for NH_3-SCR. Aktivitetsmålinger viste katalytisk aktivitet for NH_3-SCR, men karakteriseringsresultatene indikerte derimot at porestruktren til zeotypen hadde endret seg etter ionebyttinga. Dette resulterte i at virkning av mesoporer på aktivitet ikke kunne bekreftes.

Preface

I would first like to give a big thank you to my co-supervisor Magnus Rønning, for his guidance and support during this work. And my co-supervisor Ole Håvik Bjørkedal, for his patience and guidance. A sincere thank you for always answering my questions, assisting me at the lab and encourage me through the writing of this thesis. I would also like to thank the Catalysis Group at IKP and the Inorganic Chemistry Group at IKJ, under my supervisor Karina Mathisen, for being cooperative and giving me the possibility to write a thesis about catalysis for the Science Education (MLREAL).

Further, thanks to the inorganic group at IKJ for assisting me at the lab. Especially thanks to Guro Sørli, also my co-supervisor, for all the help and support during catalyst preparation, and Daniel Ali for taking SEM-images.

I would also like to thank all my classmates, both all my soon-to-be teacher classmates and my fellow master students in the catalysis group. Thanks for coffee breaks, laughter and support. And thanks to Sunniva and Leiv Jørgen for the nice board and lodging these final weeks.

Finally, thanks to the support from family and friends. Thank you, Petter, for patience and that you always believe in me. And mum and dad, thanks for always be there for me.

I declare that this is an independent work according to the exam regulations of the Norwegian University and Technology (NTNU).

Lisa Leganger Landfald, February 2019, Trondheim

Contents

List of Figures

List of Tables

List of Symbols

Symbol	Unit	Description
A_s	$\mathrm{m^2\,g^{-1}}$	Total surface area per gram catalyst
A_0	$\mathrm{nm^2}$	Surface area of one molecule
C	$\mathrm{m^{-1}}$	Curvature
D	-	Metal dispersion
d	nm	Distance between two lattice planes
M	$\mathrm{g\,mol^{-1}}$	Molar mass
m	g	Sample mass
m/z	-	Mass-to-charge ratio
N_0	-	Number of adsorbed molecules
n	-	Order of reflection
n_S	-	Number of surface atoms
n_T	-	Total number of atoms
P	mmHg	Pressure
P_0	mmHg	Equilibrium Pressure
R	$\mathrm{J\,K^{-1}\,mol^{-1}}$	Gas Constant
r	m	Radius
s	-	Stoichiometry factor
T	K	Temperature
V	$\mathrm{cm^3}$	Volume
V_M	$\mathrm{cm^3}$	Molar volume
V_0	$\mathrm{cm^3}$	Volume of one monolayer
v_m	$\mathrm{cm^3}$	Volume chemisorbed gas
$wt.\%$	-	Metal loading (weight percent)
α	$\mathrm{\mu L^{-1}}$	Slope of the BET-curve
η	$\mathrm{\mu L^{-1}}$	y-intercept of the BET-curve
θ	-	Angle
λ	nm	Wavelength
σ	$\mathrm{N\,m^{-1}}$	Surface tension
ϕ	-	contact angle
χ	-	Desorption rate constant ratio for the first and second adsorbed layer (BET)

Abbreviations

ASC	Ammonia Slip Catalyst
BET	Brunauer-Emmet-Teller
BJH	Barrett-Joyner-Halenda
CHA	Zeotype structure: Chabazite
DPF	Diesel Particulate Filter
ICP-MS	Inductively Coupled Plasma-Mass Spectrometry
I.E.	Ion-Exchange
IKJ	Department of Chemistry
IKP	Department of Chemical Engineering
IMO	The International Maritime Organization
I.W.I.	Incipient Wetness Impregnation
IZA	International Zeolite Association
MFI	Zeolite structure: Mordenite Framework Inverted
MS	Mass Spectroscopy
NA	Not Analyzed
NTNU	Norwegian University of Science and Technology
SAPO	Silicoaluminophosphate
SEM	Scanning Electron Microscopy
SCR	Selective Catalytic Reduction
SDA	Structure Directing Agent
TPR	Temperature-Programmed Reduction
TWC	Three Way Catalyst
VESTA	Visualization for Electronic and Structural Analysis
XRD	X-Ray Diffraction
ZSM-5	Zeolite Socony Mobile Five

Chapter 1

Introduction

Emission of different pollutants need to be reduced in order to maintain a sustainable future. Greenhouse gas emissions are causing global warming, which results in climate changes, and other pollutants are causing local environmental issues such as acidic rain and human health issues [1, 2]. A large amount of these emissions come from the exhaust from combustion engines used in for example vehicles or marine vessels [3]. The pollutants present in exhaust from such engines are mainly carbon monoxide (CO), hydrocarbons (HC) and nitrogen and sulfur oxides. The nitrogen oxides are nitrogen oxide (NO) and nitrogen dioxide (NO_2), often referred to as NO_X, and the sulfur oxides are reffered to as SO_X and is primarily SO_2 [3]. Clean-up systems are integrated in the exhaust system to prevent emissions of the pollutants. Typically, different catalysts are used for this task. A catalyst makes it energetically favourable for clean-up reactions to occur and possible to favor a specific reaction.

There are several challenges to overcome in order to obtain efficient clean-up of all the pollutants. For instance temperature fluctuations, different conditions regarding amount of oxygen present in the exhaust and traces of compounds which deactivate the catalyst. For combustion engines an additional challenge occur since incompatible conditions are required for the different conversion for the pollutants: CO and HC is oxidized in contrast to NO_X which is reduced, as shown in the following equations [4]:

$$\mathrm{CO} + \text{oxidant}\,(\mathrm{O_2}) \longrightarrow \mathrm{CO_2} \tag{1.0.1}$$

$$\mathrm{HC} + \text{oxidant}\,(\mathrm{O_2}) \longrightarrow \mathrm{CO_2} \tag{1.0.2}$$

$$\mathrm{NO_X} + \text{reductant} \longrightarrow \mathrm{N_2} \tag{1.0.3}$$

If O_2 is not in excess, then CO can be used as a reductant. However, if O_2 is in excess

CO will be reduced, and a different reductant is necessary.

Today, an increasing demand for efficient use of fuels result in combustion at lean conditions and lower exhaust temperatures [5]. Lean conditions are oxygen rich conditions. This changes the conditions for the clean-up systems, resulting in a need for new systems that work efficiently in oxygen rich environments and also at lower temperatures. Under these conditions the reducing of NO_X is more challenging [5]. A solution for the clean-up system can be to split it into different sections: One section for pollutants that need to be oxidized and one for the pollutants that need to be reduced. In this way, NO_X can be reduced even with a high content of oxygen in the exhaust. This requires a catalyst that can selectively reduce NO_X in lean conditions.

1.1 Emission of NO_X

When air is exposed to temperatures above 2000 ℃, as in for example flames, nitrogen and oxygen will react and form thermal NO_X [6]:

$$N_2 + O_2 \longrightarrow 2\,NO \tag{1.1.1}$$

$$2\,NO + O_2 \longrightarrow 2\,NO_2 \tag{1.1.2}$$

A challenge with NO_X-emission is that NO_X is produced regardless of the type or quality of the fuel. It is produced whenever air is present at high temperatures.

These compounds have several unwanted impacts on both the environment and the climate. First, NO_X is an indirect greenhouse gas since ground level ozone is produced when NO_X is both present in the atmosphere and in contact with sunlight [2]. Second, the oxides can form acidic rain, reduce visibility, damage animal life and damage forests [2, 3]. Third, these gases are a direct health issue for humans in small concentrations affecting both the respiratory and immune system [7].

Catalysts are installed in the exhaust system such that NO_X is reduced to nitrogen, preventing NO_X-emission. There are many types of clean-up system, with different catalysts that are in use today. The choice of clean-up system depends on the type of engine, for example if the engine is a diesel, gasoline or a liquid natural gas engine [4]. The Three Way Catalyst (TWC) is one example, and is a very successful catalyst used for gasoline engines. It consist of Pt and Pd catalysts that enable O_2 to oxidize CO and HC, and Rh and Pd catalysts that reduces NO_X [4]. The TWC's solution is to simultaneously reduce and oxidize the gases in the same environment by having a carefully chosen air-to-fuel-ratio, with excess air, that enables both a reduction and an oxidation to occur over the same catalyst. This is called stoichiometric combustion, which corresponds to a

stoichiometric mixture of oxygen and fuel. However, the ratio limits the applications for which engines this catalyst can be integrated in and it is not an optimal ratio regarding efficient use of fuels [4].

The increasing demand for more efficient use of fuels due to both economical and environmental issues, has resulted in new conditions for the clean-up system. Engines are now driven more efficiently at lean conditions with an air-to-fuel ratio of 20:1, in contrast to stoichiometric combustion which has an air-to-fuel ratio of 14.7:1 [4]. This leads to a new challenge: it is now very difficult to reduce NO_X at lean conditions [4]. In addition, engines that are more energy-efficient are expected to produce exhaust at lower temperatures, below 500 ℃, due to more complete combustion resulting in less excess heat [8]. To summarize, modern engines are ideally operating at high temperatures in oxygen rich conditions with a lower exhaust temperature at the outlet of the engine. These changes in conditions results in a demand for a new catalyst, one that can operate at lean conditions and be active at temperatures below 500 ℃.

1.2 The NH_3-SCR system

Selective catalytic reduction (SCR) is one example where NO_X is selectively reduced to N_2 in lean conditions. A reducing agent is introduced into the exhaust such that NO_X is reduced to N_2. Introducing a reducing agent to the exhaust solves the issue of reducing NO_X in the presence of oxygen [4]. This is also the only available clean-up system that fulfill the now very strict NO_X-emissions regulations [9]. The catalysts used in NH_3-SCR can for example be Vanadium based or metal-zeolites, and common for them is the challenge of being active at lower temperatures [8]. There is a need to find a more efficient catalyst that has high performance even at the lower outlet temperatures of the now more efficient engines.

When ammonia (NH_3) is used as the reducing agent, the system is named NH_3-SCR. This clean-up system is used today for both vehicles and ships [4, 9]. A sketch of the overall system is shown in Figure 1.1.

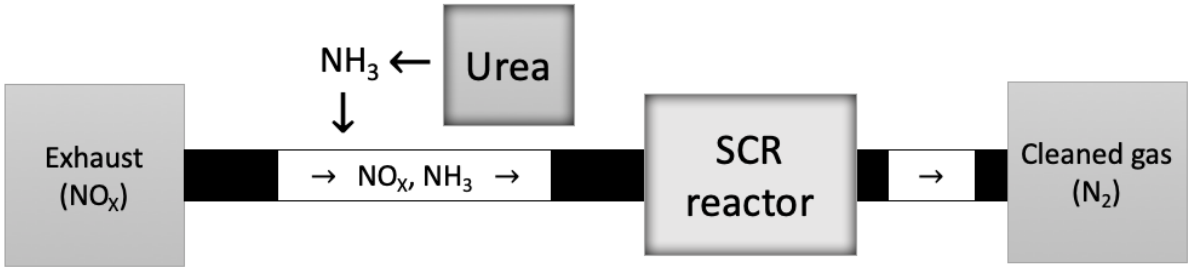

Figure 1.1: Overview of the clean-up system from combustion engine to cleaned exhaust when SCR is integrated in the system. The figure is inspired by Charkendorff and Niemantsverdriet [4].

From the combustion engine the pollutants CO_2 and HC are oxidized over a separate oxidizing catalyst upstream for the SCR [10]. In addition, a Diesel Particulate Filter (DPF) is removing the particulates from the exhaust before they enter the SCR-system. For the SCR-system, NO_X is reduced by introducing ammonia as a reducing agent in the exhaust as shown in Figure 1.1. Since NH_3 is toxic it is stored as urea and converted *in situ* to ammonia by hydrolysis and thermal decomposition [5]. Finally, the ammonia left over in the exhaust is removed over a Ammonia Slip Catalyst (ASC) [10]. It is important to ensure that leaching of NH_3 do not occur since ammonia is toxic [5].

1.3 Catalysts for NH_3-SCR

The most common catalyst in the industry for stationary NH_3-SCR is the V_2O_5/TiO_2. The Vanadium catalyst has the disadvantages of being efficient in only a small temperature range (300-400 ℃) and that Vanadium is carcinogenic [11]. For mobile applications the possibility for using the active Vanadium catalyst is less ideal, since it is more likely for catalyst leaching due to movement and unstable conditions [5].

As replacements, catalysts based on copper or iron supported on zeolites has been shown to be promising candidates [12]. Zeolites are porous and non-toxic materials with high specific surface area [13]. These new catalysts can be active in a range of temperatures. The Fe-zeolites is shown to be the most active at temperatures above 400°C, whereas Cu-zeolites are more active at lower temperatures [12]. Catalysts based on metal-zeolites for NH_3-SCR are already used in e.g. diesel trucks [13]. Some of the challenges with zeolites are hydrothermal deactivation, which happens at higher temperatures in the presence of water, and HC-poisoning [12, 5].

The preparation route of the Fe-zeolite influences the chemical state of Fe as active site, which has an impact on the performance for the Fe-zeolites. Which reaction that occurs depends on the oxidation state of Fe [11]. The catalysts can be prepared by impregnation or ion-exchange, in an inert environment or in air, or by different Fe-

precursors. All these parameters can impact the Fe species present as active metals, such as isolated monomeric Fe^{3+} or Fe_2O_3 particles [5]. During ion-exchange is the active metal introduced by exchanging it with an ion placed in the framework of the support, in contrast to impregnation where the metal is dispersed over the support [14].

Molecular sieves, such as zeolites and zeotypes, can be used as support. Zeolites and zeotypes are porous materials built from tetrahedrally coordinated atoms, called T-atoms, arranged in different structures [4]. The difference between the two is the type of T-atom present. A zeolite used for NH_3-SCR is a ZSM-5 zeolite which has a MFI structure [15]. This structure has the drawbacks of having low hydrothermal stability, coke formation and being vulnerable to hydrocarbon-poisoning [12]. Material development has shown that molecular sieves that have the chabazite structure (CHA) improves hydrothermal stability and yield smaller pore size which inhibit coke and hydrocarbon poisoning [12]. The zeotype SAPO-34 has this CHA structure, and can be synthesized either with micropores only or with micro- and mesopores combined in the same framework. They are called conventional SAPO-34 (C-SAPO-34) or hierarchical SAPO-34 (hi-SAPO-34) respectively.

Introducing the metal when molecular sieves are used as support is typically done by ion-exchanged compared to impregnated, however both preparation methods have been studied [11, 16, 17]. An advantage with impregnation is the upscale for industry. On the other hand, the exchanged molecular sieves has shown very good activity towards NH_3-SCR [5]. The ZSM-5 support have bigger pores than the SAPO-34 supports, which could make the ion-exchange process easier, because the ions can penetrate the pores more easily. Furthermore, the hi-SAPO-34 have mesopores in addition, which may introduce an alternative transport option for easier ion-exchange.

1.4 Goal of Thesis

In this thesis different Fe-ZSM-5 catalysts and Fe-SAPO-34 catalysts were synthesized with the goal of studying the catalytic performance towards NH_3-SCR at lower temperature (< 500 °C). Commercial ZSM-5 zeolites and hydrothermally synthesized conventional and hierarchical SAPO-34 was used as supports for the catalysts. The iron catalysts were prepared by changing certain parameters: Two choices of iron-precursor, iron(III)nitrate and iron(II)chloride; and two synthesis methods, incipient wetness impregnation and ion-exchange. The catalysts were characterized by XRD, N_2-physisorption, H_2-TPR, CO-chemisorption and ICP-MS. Finally, the performance of the catalysts for NH_3-SCR were tested to compare the different catalysts.

As a result, quite a few catalysts are synthesized during this project. Studies concerning NH_3-SCR found in the literature inspired the choice of preparation route. However, the use of iron(III)nitrate as precursor was due to issues regarding diluting first pur-

chased iron(II)chloride, resulting in a possibility to compare preparation with iron(III) and iron(II). The motivation for the preparation of the different catalysts were archiving a high performance towards NH_3-SCR at lower temperatures. Fe-ZSM-5 catalysts and Fe-SAPO-34 catalysts are common catalysts for studies towards this reaction. The Fe-hi-SAPO-34 catalysts, however, seem not to have been reported on in the literature.

Chapter 2

Theory

The theory behind the molecular sieves ZSM-5 and SAPO-34, the NH_3-SCR reaction and the different synthesis and characterization techniques used for this work is described in the following chapter. A descriptions of the structures of the supports is outlined. The relevant reactions for the NH_3-SCR, as well as iron as active metal, deactivation and consequences of water present over the process are also given. Further, the theory of the synthesis methods ion-exchange and incipient wetness impregnation are described. Finally, theory on the characterization techniques used for this work is explained: XRD, N_2 physisorption, H_2-TPR, ICP-MS and chemisorption.

2.1 Molecular sieves: ZSM-5 and SAPO-34

Zeolites and zeotypes are solids which both are crystalline oxides molecular sieves with a porous framework and has high surface area [18, 6]. These materials are good fits for both being a catalyst and as a catalyst support [18]. They are built up of different T-atoms which are bonded together through an oxygen bridge [6]. A zeolite is built up from SiO_4 and AlO_4 tetrahedra, whereas a zeotype has other T-atoms for example phosphorous [4]. This framework enables the material to have an especially open structure with pores, cages and channels. The pores can be micro- or meso sized, which have IUPAC defined sizes of less than 20 Å and 20-500 Å respectively [6]. In this thesis, a ZSM-5 zeolite and two SAPO-34 zeotypes are studied.

ZSM-5 is short for Zeolite Socony Mobile Five, and it has an MFI structure and the chemical formula is $Na_n{}^+Al_nSi_{(96-n)}O_{192}\, x\, 16\, H_2O$, $n > 27$ [15]. The chemical structure of this zeolite is illustrated in Figure 2.1. The structure is build up from SiO_4 tetrahedra with AlO_4 tetrahedra substituting some of the SiO_4. The protons shown in the figure are placed at Brønsted acid sites. A Brønsted acid is able to donate protons. For a zeolite, the amount of Brønsted acid sites is equal to the amount of aluminium atoms, because

the protons neutralize the one unit charge aluminium has less than silicon [5].

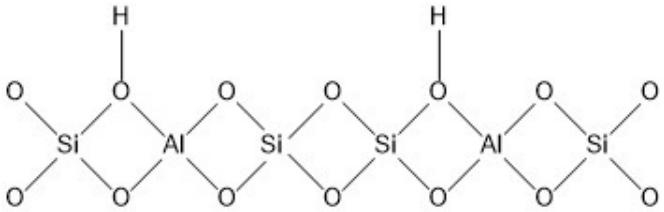

Figure 2.1: Chemical structure of a zeolite. The protons are located at Brønsted acid sites.

This material has different ring channels, and the biggest ring is a 10-membered ring with a diameter of approximately 5-6 Å, which is illustrated in Figure 2.2 [6]. In addition, a ZSM-5 does not have cages in contrast to the SAPO-34. It has a specific surface area of approximately 425 $m^2\,g^{-1}$, with some small variations depending on the Si/Al-ratio [19]. The particle size is in the range of 2 to 5 µm [20].

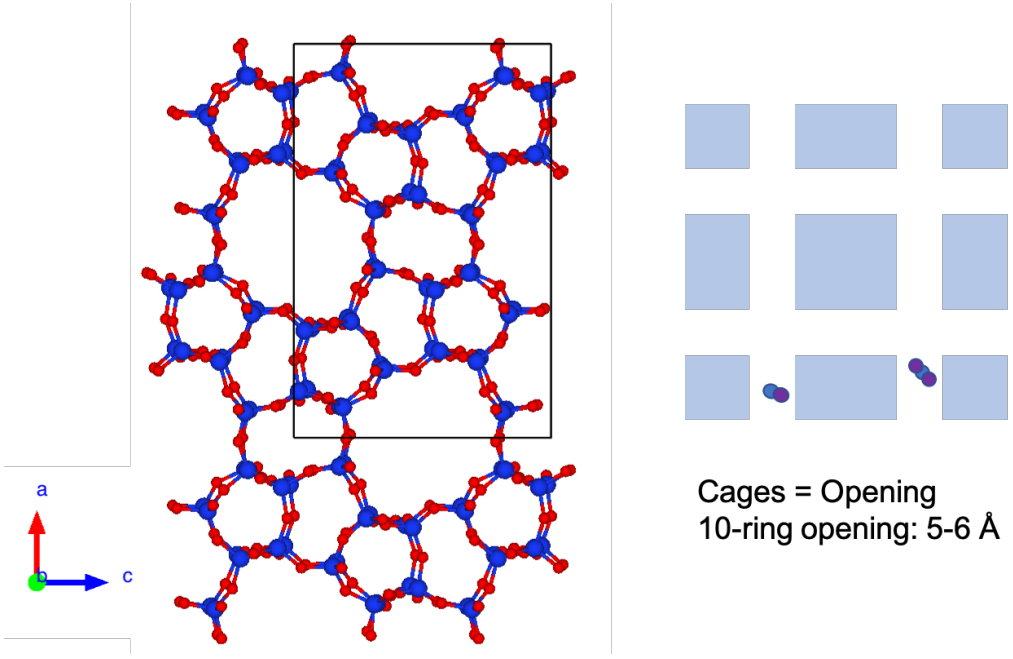

Figure 2.2: Framework of MFI-structure projected along [010] and an illustration of the molecular channels for the MFI structure for ZSM-5 for the 10-ring opening. Figure inspired by Ertl et al. [6] (pages 2952-2954). Framework created in Vesta [21].

One particular group of molecular sieves is materials structured from SiO_4, AlO_4 and PO_4 tetrahedra, named SAPO-θ, where the θ indicate a certain type of 3D framework [18]. The zeotype with the CHA structure, a structure that is topological related to zeolites, is labeled SAPO-34. The chemical formula for SAPO-34 is $(SiO_2)_x(P_2O_5)_y(Al_2O_3)_z$ [22]. Figure 2.3 shows the chemical structure of the zeotype SAPO, and that the proton is also here located at a Brønsted acid site. For this structure the tetrahedras AlO_4 and PO_4 are alternating, with SiO_4 tetrahedra replacing some of the Al- or P-tetrahedra [4]. For this

zeotype the amount of Brønsted acid sites are equal to the amount of Silica present as T-atoms. The framework is neutral if no silicon is present since the one positive unit charge of aluminum is neutralized by the one negative unit charge of phosphorus. However, if silicon is present, the charge will not be neutralized due to silicon having a net zero charge as a T-atom, therefore a proton is added to balance the framework.

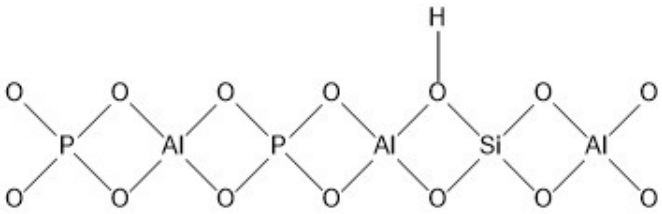

Figure 2.3: Chemical structure of a zeotype. The proton is located at a Brønsted acid site.

The biggest ring channels are the 8-membered rings with a diameter of approximately 4 Å [6]. This material is structured with a cage, with a dimension of 7.3 x 12 Å, in addition to the channels [6]. The 8-membered ring channel and the cages are illustrated in Figure 2.4. The average particle size is in the range of 2 to 15 µm and the specific surface area is approximately 550 $m^2\,g^{-1}$ [22].

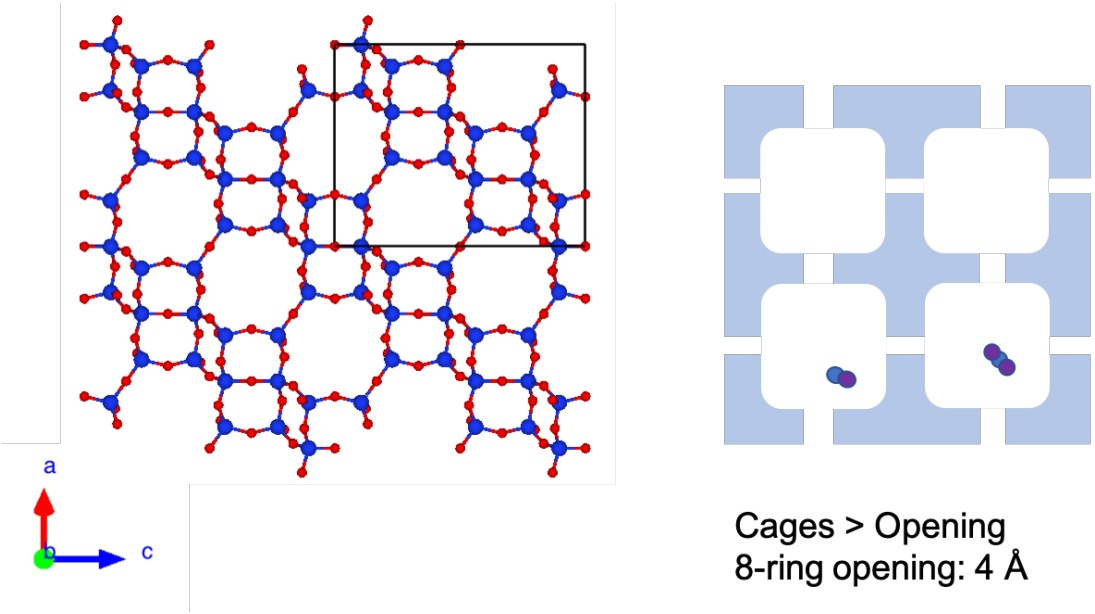

Figure 2.4: Framework of CHA-structure projected along [010] and an illustration of the molecular channels and cages for this structure. The 8-ring pore opening are shown. Figure inspired by Ertl et al. [6] (pages 2952-2954). Framework created in Vesta [21].

The zeotypes SAPO-34 can be synthesized with different pore structures. Conventional SAPO-34 (C-SAPO-34) have micropores, whereas hierarchical SAPO-34 (hi-SAPO-34) have meso- and micropores [23]. The mesoporous network for hi-SAPO-34 zeotypes is added to the bulk which still consists of micropores. These mesopores provides a new

transport alternative for the molecules, which could improve the diffusion [23]. Zeotypes can be made by using different structure directing agents (SDA) for the preparation which gives it the specific pore property. A hi-SAPO-34 zeotype can be made by using a meso-SDA in addition to a micro-SDA [23].

2.2 NH_3-SCR

In this section, the aspects of the NH_3-SCR system using metal-zeolites or zeotypes as catalysts is described. The NH_3-SCR reduction takes place over three different reactions where NO, NO_2 and NH_3 are reactants producing N_2 and H_2O: The standard reaction (2.2.1), the fast reaction (2.2.2) and finally a reaction with only NO_2 involved (2.2.3) [5]:

$$4\,NH_3 + 4\,NO + O_2 \longrightarrow 4\,N_2 + 6\,H_2O \tag{2.2.1}$$

$$2\,NH_3 + NO + NO_2 \longrightarrow 2\,N_2 + 3\,H_2O \tag{2.2.2}$$

$$4\,NH_3 + 3\,NO_2 \longrightarrow \frac{7}{2}\,N_2 + 6\,H_2O \tag{2.2.3}$$

The amount of NO compared to NO_2 determined which of the reaction that occur. In the exhaust NO is dominating, and therefore reaction 2.2.1 is the standard reaction [24]. More than 90 % of the nitrogen oxides in exhaust are NO [25]. However, for an efficient NO_X conversion the fast SCR-reaction is needed, and this is favoured when the reaction mixture is 1:1 of NO and NO_2 [24]. Therefore some NO is oxidized to NO_2 before reaching the catalyst [5]. This is normally done over an oxidation catalyst prior to the SCR system. The oxidation of NO can also occur as a gas phase side reaction. This is desired due to more NO_2 being formed, and therefore the fast SCR-reaction is favoured. This oxidation reaction is shown in Equation 2.2.4 and is assumed to be the rate determining step for the overall NH_3-SCR [5]:

$$NO + \frac{1}{2}\,O_2 \rightleftarrows NO_2 \tag{2.2.4}$$

The last SCR-reaction, Equation 2.2.3, occurs if the ratio of NO:NO_2 is less than 0.5 [5]. For this condition the reaction will happen with only NO_2.

It is important to avoid side reactions that produce undesired side products, such as the greenhouse gas N_2O, to have an efficient reduction of NO_X [7]. Important side reactions are the formation of N_2O shown in the following Equations 2.2.5, 2.2.6 and 2.2.7 and the oxidation of NH_3 shown in the Equations 2.2.8 and 2.2.9 [5]:

$$2\,NH_3 + 2\,O_2 \longrightarrow N_2O + 2\,H_2O \tag{2.2.5}$$

$$4\,NH_3 + 4\,NO + 3\,O_2 \longrightarrow 4\,N_2O + 6\,H_2O \tag{2.2.6}$$

$$4\,NH_3 + 4\,NO_2 + O_2 \longrightarrow 4\,N_2O + 6\,H_2O \tag{2.2.7}$$

$$4\,NH_3 + 5\,O_2 \longrightarrow 4\,NO + 6\,H_2O \tag{2.2.8}$$

$$4\,NH_3 + 3\,O_2 \longrightarrow 2\,N_2 + 6\,H_2O \tag{2.2.9}$$

2.2.1 Iron species as active sites

There are several iron species that can be the active iron specie towards NH_3-SCR for Fe-zeolite systems, and which one of them is the active site is not concluded in the literature [5, 26]. Some possible species found in literature are: monomeric iron, such as isolated Fe^{3+}; dimeric iron, such as $[OH\text{-}Fe\text{-}O\text{-}Fe\text{-}OH]^{2+}$; or larger or smaller iron species, such as FexOy particles and nanoparticles [5, 26, 27]. Figure 2.5 illustrates the active sites monomeric iron, dimeric iron and the iron particle Fe_2O_3. Monomeric iron means one iron atom, whereas dimeric means two iron atoms present in the complex.

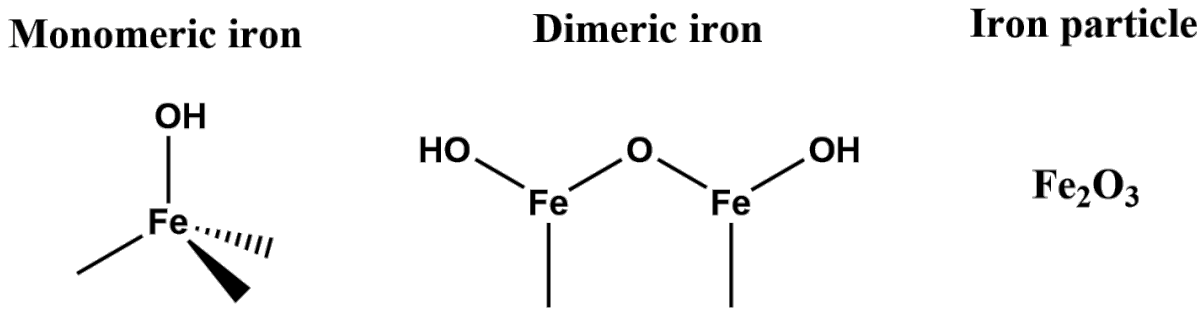

Figure 2.5: Possible iron species present as active sites Fe-zeolites for NH_3-SCR. Monomeric iron, dimeric iron and an iron particle are shown. Figure is inspired by Shwan [28].

It is the temperature that determines the type of iron specie as active site for the activity towards NH_3-SCR. At temperatures below 300 ℃, the monomeric isolated Fe^{3+} species are the dominating active sites. At temperatures between 300-500 ℃, contributions from dimeric and larger iron clusters, such as Fe_2O_3, are more dominating. And at temperatures above 500 ℃, the dimeric species are dominating [5, 27]. For the activity towards the side reaction NH_3-oxidation (see Equation 2.2.8, 2.2.9), is it reported that below 500 ℃, dimeric iron species is active. Above this temperature are both monomeric and larger iron clusters active, such as Fe_2O_3 [27]. An overview of the temperature dependency is shown in the following Table 2.1:

Table 2.1: Different iron species as active sites for different temperature towards the NH_3-SCR and NH_3-oxidation.

Temperature (℃)	Iron specie as active site	Reaction
< 300	Monomeric iron	NH_3-SCR
$300 - 500$	Dimeric iron, larger iron clusters (e.g. Fe_2O_3)	NH_3-SCR
> 500	Dimeric iron	NH_3-SCR
< 500	Dimeric iron	NH_3-oxidation
> 500	Monomeric iron, larger iron clusters (e.g. Fe_2O_3)	NH_3-oxidation

The activity is still a matter of debate, and for example, it is reported that Fe_2O_3 particles are inactive for NH_3-SCR, and only active for the NO-oxidation [29]. For an Fe-catalyst supported by the zeotype chabazite, the monomeric iron specie $[Fe(OH)_2]^+$ and the dimeric iron specie $[OH\text{-}Fe\text{-}O\text{-}Fe\text{-}OH]^{2+}$ are suggested as active sites [26].

It is mainly reported that monomeric isolated Fe^{3+} iron is the active specie for low temperature SCR. These monomeric iron can be introduced for Fe-zeolite systems by ion-exchange with Fe^{2+}, which is small enough to penetrated the pores and form the monomeric isolated Fe^{3+} [26]. In addition, it is suggested that optimal conditions towards low temperature activity for a Fe-ZSM-5 catalyst with Si/Al-ratio of 14, could be to ion-exchange with a degree of approximately Fe/Al=0.4 [27]. For this value more monomeric iron could be present at the surface.

When metal-exchanged zeolites are used as catalysts for the NH_3-SCR the reaction scheme is more complex [5]. A suggested reaction mechanism is shown in Figure 2.6 [26]. As can be seen, there are several iron species present for the NH_3-SCR. For this thesis, the catalysts were tested towards the standard SCR, which is illustrated in the blue reaction route.

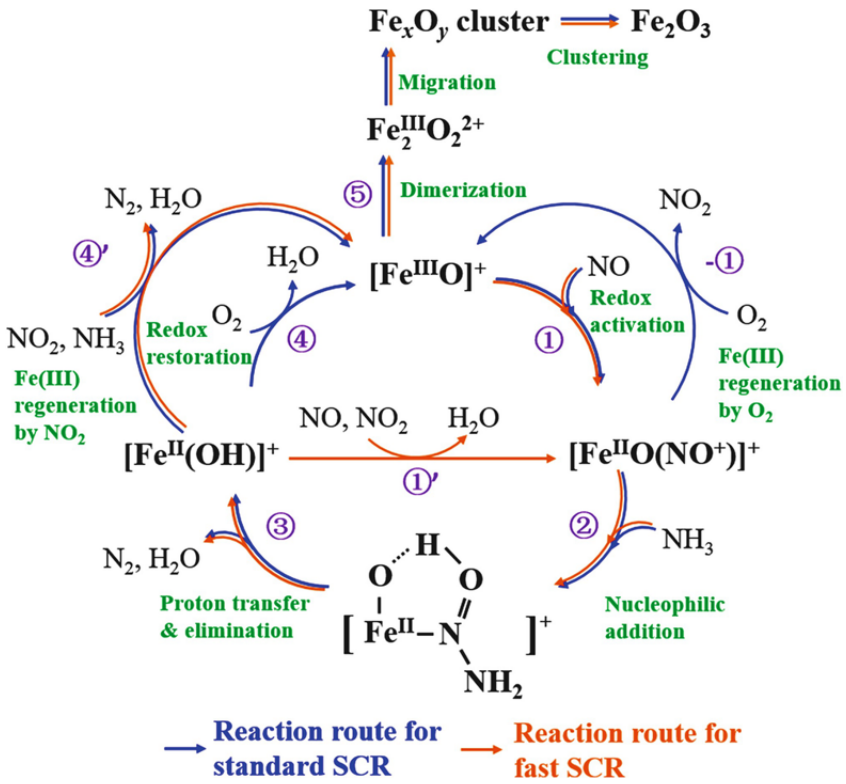

Figure 2.6: Proposed NH_3-SCR reaction mechanism for Fe-zeolites. Reaction route for both standard and fast SCR are shown. Figure reproduced from Jiang and Lobo [26].

The iron specie $[Fe^{III}O]^+$, a monomeric isolated Fe^{3+}, is the starting point for the catalytic cycle. The oxidation state of the iron species are changing during the different reactions steps. The reaction 5 is suggested to be the consequence of hydrothermal deactivation (see Subsection 2.2.2) where active sites are lost [26].

2.2.2 Aspects influencing the catalytic performance: Diffusion, water effects and deactivation

For a catalytic reaction, diffusion can limit the reaction rate [30]. For small pores, such as micropores, the specific surface area is increasing, however this also may have a negative impact on the diffusion rate of the reactants or products. The reaction rate, and therefore the specific activity, may be decreasing with a microporous catalyst due to diffusion limitations [30]. If the surface reaction is fast, it is even more likely that diffusion limits the overall reaction. The transport of molecules in and out of pores are easier if the pores are bigger. Therefore, the diffusion may be faster and less limiting for the overall reaction for bigger pores. A consequence of this is that the transport of molecules may be different for micro- and mesopores.

Presence of water for the SCR reaction has a significant influence on the performance of the different reaction and side reaction for SCR, as well as the stability for zeolites [27,

5]. The exhaust from the combustion engine contains approximately 10 % steam as a product from the combustion reaction. In presence of water both the NH_3 oxidation, NO-oxidation and the conversion of the reactants is greatly influenced by presence of water [11]. Presence of water can also result in an improved catalytic selectivity, due to oxidation activity being reduced [24]. In addition, the SCR reaction is prohibited and the formation of the undesired side product N_2O is reduced [24].

A Fe-ZSM-5 catalyst is thermally unstable at temperatures above 500 ℃ in the presence of water, due to hydrothermal deactivation [5]. This loss in catalytic performance is due to presence of water at higher temperatures, and as an example active iron sites can be lost [26]. SAPO-34 has shown much improved hydrothermal stability. This is because the CHA structure has smaller pores which results in much better stability in the presence of water [8]. The ZSM-5 zeolite has a bigger pore size, which results in less hydrothermal stability. In addition, it is claimed that absence of alkali metals in the framework, which is the case for SAPO-34 and not for ZSM-5, also improves the hydrothermal stability [26].

Metal-zeolites have three main challenges due to deactivation: tolerance for chemical poisoning, blocking of pores from hydrocarbons and, as previously mentioned, deactivation due to pore hydrothermal stability [5]. The SAPO-34 is shown to deactivate faster than a ZSM-5 catalyst, regarding a study of converting methanol to hydrocarbons [6]. SAPO-34 is more sensitive to coke formation due to the cage structure [6]. However, SAPO-34 is more resistant to irreversible deactivation, suggested to be because of, among other things, weaker acid strength. A Cu-ZSM-5 catalysts has shown to have improved performance at lower temperatures, however the Fe-ZSM-5 catalyst has better tolerance for chemical poisoning and lifetime in hydrothermal conditions [8]. Pretreating a Fe-ZSM-5 catalyst with H_2 has improved activity and stability for SCR reactions [5].

2.3 Introduction of metal in supports

For this thesis, iron catalysts with ZSM-5, C-SAPO-34 and hi-SAPO-34 as supports were synthesized. The iron is introduced by ion-exchange and incipient wetness impregnation, which are explained in the following sections.

2.3.1 Ion-Exchange in aqueous solutions

In ion-exchange, the metal is introduced by exchanging ions in the framework by an other metal-ion. Typically, the ions exchanged are the protons present at Brønsted acid sites with other metal cations, however in some cases other cations are present in stead of protons at the acid sites.

For aqueous ion-exchange several challenges present themselves. First, achieving a high exchange degree and, second, enable the solution to penetrate the small pores of a zeolite [5]. The exchange degree is the amount of exchanged metals compared to available ions at Brønsted sites. The higher the exchange degree, the more active metal are present in the framework. A high exchange degree can be accomplished by repeating the exchange process several times. The exchange degree is maximum 50 % for M/Al when a Fe-ZSM-5 catalysts is used [24].

For the second challenge, the pore size of ZSM-5 (5-6 Å) is shown to be large enough to enable ion-exchange with iron. In contrast, for C-SAPO-34, the pore size is smaller (4 Å) and as a consequence the ion-exchange with iron may be more challenging [12]. The hi-SAPO-34 zeotype has even larger pore size with mesopores, which may results in the ion-exchange being easier compared to the conventional SAPO-34. Using iron with smaller ion size, such as Fe^{2+}, could result in the ions penetrating the pores more easily. The hydrated Fe^{2+} ions has an ionic diameter of 6 Å, whereas the bulky and hydrated Fe^{3+} ion has an ionic diameter of 9 Å [31]. Fe^{2+} ions can easily oxidize to the bulky hydrated Fe^{3+} ions in atmospheric conditions. Therefore it is suggested to exchange under an inert atmosphere with a low pH to maintain Fe^{2+} cations instead [26].

Studies show that having isolated Fe^{3+} as active sites in the zeolites results in an increased activity at lower temperatures [32]. These Fe^{3+} are likely formed inside of the pores when Fe^{2+} is used as the iron precursor for the ion-exchange [26].

Studies for Cu-exchanges C-SAPO-34 have proposed a different approach for ion-exchange, namely a two step aqueous ion-exchange [33]. When the SAPO-34 support, in its proton form, is directly exchanged with the active metal, the structure may be damaged. For example, the Si-O-Al bond can be destroyed [33]. An alternative approach is to first exchange the proton placed at Brønsted acid sites by $NH_4{}^+$ ions, then exchange these $NH_4{}^+$ ions by a metal ion. In this thesis, this approach was tested for iron-exchanged SAPO-34 catalysts.

2.3.2 Incipient Wetness Impregnation

Incipient wetness impregnation is a procedure where the metal is introduced via a precise volume of metal aqueous solution, so that the support is saturated with liquid: the pores are filled with the metal solution and no excess solution is outside the pores [14]. It is capillary forces that enable the solution to diffuse into the pores and the metal to be dispersed in the support. This is a straightforward process which is easy to upscale in industry [11]. After introducing the metal solution, the impregnation, the sample is dried. This enables the solution to escape from the pores, leaving only the metal left in the support. The drying time may influence the dispersion of metal. The metal could follow the solution out of the pores with too slow drying, and with too fast drying the

dispersion is uneven due to metal solution being trapped deep in the pores [14].

2.4 Characterization techniques

In the present subsection are the theory behind the characterization techniques described.

2.4.1 X-Ray Diffraction

The crystal phases of a sample can be identified by the bulk analysis X-ray diffraction (XRD) by applying Bragg's law. If a monochromatic X-ray with a wavelength λ is equal or less than two times the interatomic distance d between two crystal planes, $\lambda \leq 2d$, then the added path difference for the reflected X-ray is $2d\sin\theta$ [4]. This is illustrated in Figure 2.7. The angle θ is the measured angle between the incident X-ray and the crystal plane.

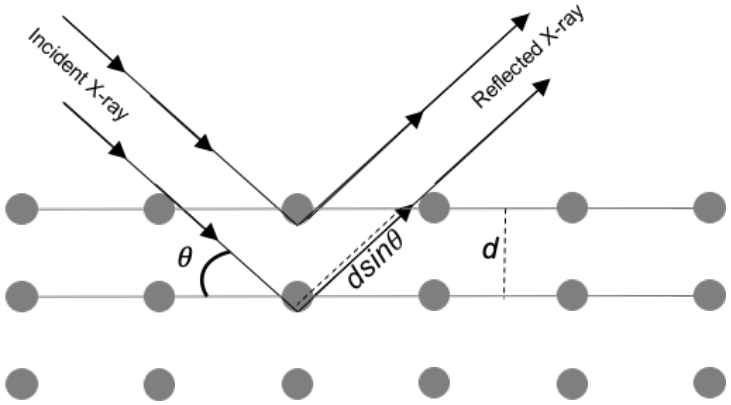

Figure 2.7: Illustration of Bragg's law. It is illustrated how the incident X-ray is scattered over a an ordered lattice. The angle θ is shown as the angle between the X-ray and the crystal plane, d the interatomic distance and $d\sin\theta$ the added path difference. Figure inspired by Charkendorff and Niemantsverdriet [4].

Diffraction will then occur if the added path difference is an integer, n, multiplied with the wavelength, λ, as described in Bragg's law [4]:

$$n\lambda = 2d\sin\theta, \quad n = 1, 2, ... \tag{2.4.1}$$

From this relation, the diffraction patterns of powder samples can be predicted by an X-Ray Powder Diffraction experiment. When diffraction occur, the intensity is plotted as a function of 2θ in a diffractogram. This shows the resulted diffraction pattern, which reflects the possible crystal phases of a sample [4].

A sample's identity can also be confirmed with XRD, since XRD gives an indication of the structure of a material. The diffractogram of the sample can be compared to diffractograms of known materials. In this way, an XRD-analysis can provide "fingerprint" information about a sample.

An XRD-analysis detects a lot of crystal phases, however some may not be detected [4]. Peaks can overlap in the diffractogram, making it more difficult to distinguish them. Further, the XRD-instrument does not have a very high sensitivity, which may results in low-concentrated crystal phases, such as highly dispersed particles, and then too small crystals are not detected [34, 35].

The ZSM-5 zeolite has the MFI structure whose the crystal phases is given in the diffractogram shown in Figure 2.8 [15].

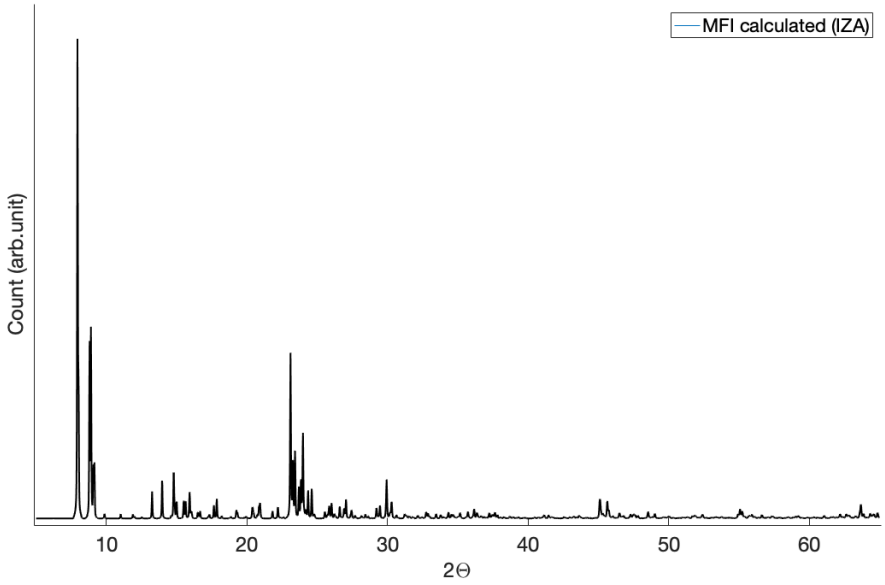

Figure 2.8: Diffractogram for the MFI structure. Structure data plotted is collected from IZA Synthesis Commission [15].

The diffractogram for the CHA structure for the zeotype SAPO-34 is as shown in Figure 2.9 [15].

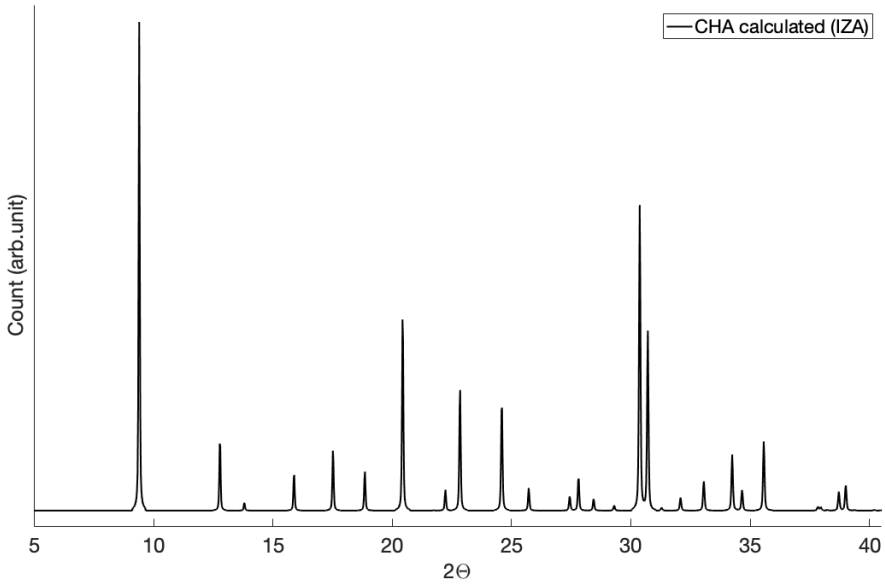

Figure 2.9: Diffractogram for the chabazite structure. Structure data plotted is collected from IZA Synthesis Commission [15].

2.4.2 N_2 Physisorption

From N_2-physisorption techniques an adsorption and desorption isotherm is calculated. This isotherm can provide estimates about the specific surface area of a solid sample, $m^2\,g^{-1}$, by the Brunauer, Emmett and Teller (BET) model, and the pore distribution by the Barret, Joyner and Halenda (BJH) theory [36]. The N_2-adsorption isotherm is found by measuring the amount of an inert gas molecule, typically N_2 molecules, that is physisorbed onto the surface, as a function of relative pressures. Physisorption is adsorption to the surface without chemical bonding between the adsorbate and the surface molecules, only weak bonds such as Van der Waals forces are interacting [4]. An isotherm describes the relationship between the surface coverage and the pressure above the surface [4].

The adsorption shape of the isotherm differ depending on the porosity of the sample, as shown in Figure 2.10. Type IV is a typically isotherm shape for mesoporous samples, and Type I for microporous samples, e.g. zeolites.

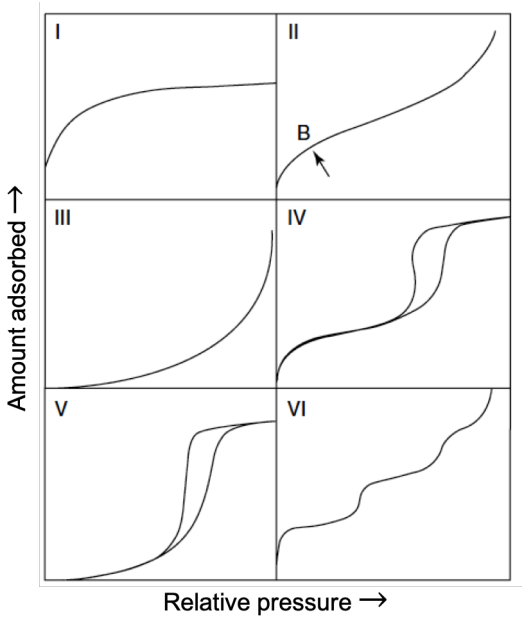

Figure 2.10: N_2 adsorption and desorption isotherms from IUPAC classification [6].

For mesoporous materials, a hysteresis loop is observed at higher pressures due to the effect of capillary forces: The gas molecules will adsorb and desorb at different equilibrium pressures in the pores. For microporous materials, such as zeolites, the curve is shaped as a continuous function at intermediate pressures. This effect is due to the volume not changing when all pores are filled, explaining the plateau like shape of the curve. The pore size also limits the formation of multilayers, which is an assumption for the BET-model [4].

When finding the surface area by the BET-model a sample with a known mass, m, is cooled down to 77 K in a glass tube with a small volume and covered with the inert gas. One N_2 molecule covers an area of 0.162 nm^2 at 77 K, this area is named A_0. The total surface area per gram catalyst, A_S, can then be calculated by knowing the A_0 and, in addition, analyzing the number of N_2 molecules needed for complete cover of one monolayer at the sample surface, N_0. A monolayer is a single layer of adsorbed molecules at the sample's surface. This calculation is shown in Equation 2.4.2:

$$A_S = \frac{A_0 N_0}{m} \tag{2.4.2}$$

The measure of N_0, the volume of one monolayer, V_0, is found from the BET analysis. An A_S-plot is made: the expression $P/(V(P_0\text{-}P))$ is plotted against the equilibrium pressure, P/P_0. The expression is shown in Equation 2.4.3, and is derived from the BET isotherm [4]:

$$\frac{P}{V(P_0 - P)} = \frac{1}{\chi V_0}\frac{(\chi - 1)P}{\chi V_0} = \eta + \alpha \frac{P}{P_0} \tag{2.4.3}$$

The pressure measured is P, the equilibrium pressure of the inert gas at 77 K is P_0, V is the total volume of adsorbed inert molecules on the sample, and χ is the ratio of the desorption rate constant of the first and second adsorbed layer [4]. The BET isotherm is linear at lower pressure regions, $P/P_0 \in [0.05, 3]$, which reflects the region for monolayer formation [37]. For these points, a linear regression gives an estimate of the slope, α, and the y-intercept, η. From these values V_0 is calculated as in Equation 2.4.4.

$$V_0 = \frac{1}{\alpha + \eta}. \tag{2.4.4}$$

This calculation can be subjective since the linear regression depends on the values that are consider to lay within the linear region of the BET isotherm [37]. Two criteria gives a guidance for how to choose the linear region. First, the value η should be positive. Second, within the pressure range used, the estimate the values for $V(P/P_0)$ should increase with P/P_0 [37]. For smaller pores, such as micropores, the BET range is often below the normal BET range mentioned above.

Some limitations of this analysis technique are the assumptions of ideal conditions such as all sites being equal, adsorbed molecules covers only one monolayer in the BET isotherm region, and a continuous growth of layers corresponding to adsorption on a free surface. The last assumption does not hold for very small pores, which is the case for zeolites. For microporous materials, the literature suggests that the adsorption is filling the pores instead of building up layers [37]. The consequence is an adsorption where the pores are filled instead of covering the surface area. Nevertheless, the surface area can be estimated despite the limitation of multilayers [37]. In addition, defects in the sample can effect the surface area, such as blocked pores or defects in the structure destroying pore channels [37].

As mentioned before, the pore size distribution can be found from the N_2-adsorption isotherm, by applying the BJH-theory. For mesoporous samples with a hysteresis loop, the pore size radius, r, can be estimated with the assumption that this pore size is controlling the meniscus curvature, C [38]. The Kelvin equation, shown in Equation 2.4.5, relates the curvature and the relative pressure, P/P_0, such that the distribution can be measured from the N_2-adsorption isotherm [38]:

$$\frac{RT}{V_M} ln(P/P_0) = \sigma C = \sigma \frac{-2\cos\phi}{r}, \tag{2.4.5}$$

where R is the gas constant, T is the temperature, V_M is the molar volume, σ is the surface

tension and ϕ is the contact angle. The pore size distribution is different for the adsorption and the desorption of the N_2 gas. This equation describes the capillary condensation phenomena which is the reason for the hysteresis loop for mesoporous samples.

It is important to be aware of the tensile strength effect (TSE) for the desorption curve, due to forced closure of the hysteresis loop [39]. The result is a peak at 38 Å, which is important to not conclude being part of the sample's pore distribution. This is also visible for the N_2-isotherm around $P/P_0 = 0.45$ as an extra drop in the isotherm.

2.4.3 Temperature-programmed reduction of H_2

For a temperature-programmed analysis, the sample is studied as a function of temperature. Temperature-programmed reduction of H_2 (H_2-TPR) provides information about the reduction process, such as reduction temperatures and if the reduction occur over one or multiple steps [6]. H_2-TPR uses H_2 as the reducing agent.

The sample is pretreated in a flow of oxygen followed by a flow of an inert gas at higher temperatures and then cooled to room temperature, such that all active phases are oxidized and adsorbed molecules at the surface are removed. Then, a flow of H_2/Ar is sent through the reactor with the sample, and the temperature is increased linearly [6]. The H_2-uptake is continuously measured by monitoring the outlet gas mixture. The peaks can reveal reduction of several oxidation states before metallic state [4]. This can also indicate which oxides that may be present for the different samples. Where the peaks do occur depends on the conditions for the experiment, so some caution is needed when comparing TPR-results to others work [40].

Equation 2.4.6 show an example of the reduction process of a metal ion in a zeolite [6]:

$$M^{n+} + \frac{n}{2}H_2 = M^0 + nH^+. \tag{2.4.6}$$

2.4.4 ICP-MS

Inductively coupled plasma-mass spectrometry (ICP-MS) is an element analysis which determines the chemical composition of the bulk [6]. This technique enables detection of elemental concentrations down to 0.01 ppm. The sample is dissolved in a strong acid, such as hydrofluoric acid, then ionized over a plasma and the ions' mass-to-charge ratio, m/z, is determined by a mass spectrometer (MS) [6].

2.4.5 Chemisorption

In chemisorption the specific surface area of metal per gram catalyst is measured, $m^2\,g_{cat}^{-1}$, and from that value the metal dispersion can be estimated. It is assumed that the number of active sites is proportional with metal area measured by chemisorption [4]. Metal dispersion is the fraction of active and accessible surface atoms, n_S, relative to the total amount of metal, n_T. This relation is described in the following equation:

$$D = \frac{n_S}{n_T}. \tag{2.4.7}$$

For the analysis, the sample is completely reduced such that the active metal is present in its metal phase. Then, a gas molecule, typically H_2 or CO, is adsorbed onto the sample as a function of equilibrium pressure which gives an adsorption isotherm [6]. The gas molecules are chemisorbed to the surface, meaning an electron-sharing valence bond is shared between the metal and the adsorbed molecules.

The chemisorption can be both irreversible and reversible. Irreversible chemisorption is the strong bonding between the metal and the adsorbing molecule [41]. The reversible chemisorption could occur over both the metal and over the support, and is a weaker interaction which is not permanent after evacuation of the adsorbing molecules [6]. The aim is to measure metal sites available for strong interactions, the irreversible chemisorption, since these act as active sites for the catalytic reaction.

In order to only study the irreversible chemisorption, a readsorption of the sample is done, such that two isotherms are measured, an upper and a lower isotherm. The upper isotherm represent the total amount of adsorbed gas molecules, both reversible and irreversible [41]. Then an evacuation step is done, where the reversible adsorbed molecules are removed. Finally, the lower isotherm is found by the readsorption where only the reversible adsorption occur again [41]. The irreversible adsorbed gas isotherm is then found by calculating the difference between the upper and lower isotherms.

From an chemisorption analysis, the volume of chemisorbed gas, v_m, is measured. This is found by back-extrapolating the isotherm representing the irreversible adsorbed gas to zero pressure, and the value is found as the intercept of the vertical axis [6]. From this value the metal dispersion, D, is calculated as shown in Equation 2.4.8 [6]:

$$D = \frac{v_m\ s\ 100M}{V_M\ m\ wt} \tag{2.4.8}$$

where s is the chemisorption stoichiometry, m is the sample mass in gram, wt is the metal loading, M is the molar mass. The value 22414 is the molar volume, V_M, amount of gas one mole occupies at standard temperature and pressure.

To estimate the dispersion the stoichiometry factor is important. This factor describes how the gas molecule bonds to the surface, which influences the number of bonding gas atoms per metal atom [4]. The bonding can for example be dissociative, associative or a combination. In this thesis CO adsorption is studied over a Fe/molecular sieve catalyst. In the literature, CO is recommended for studying for iron, however the stoichiometry factor is debated. For this thesis, it is assumed a dissociative adsorption of CO, $s = 2$, based on the work reported by Boudart et al. [42].

Chapter 3

Methods

The preparation procedures, the characterization techniques and catalytic testing for NH_3-SCR are described in this chapter. In total, 16 samples were prepared: six SAPO-34 supports and 10 catalysts. The synthesis of the SAPO-34 supports are described in Section 3.1. Solid iron-based catalysts supported by ZSM-5, C-SAPO-34 and hi-SAPO-34 zeolites were prepared using different preparation routes which are described in Section 3.2. Then Section 3.3 outlines details regarding the characterization techniques. Finally, in Section 3.4, the activity testing for measuring NO_X-reduction is described.

3.1 SAPO-34 support preparation

The Fe-SAPO-34 catalysts were prepared by first preparing conventional and hierarchical SAPO-34 (Si/Al=0.3, 0.2) by hydrothermal synthesis, followed by a two-step ion-exchange of the zeotypes by $Fe(II)Cl_2$ under nitrogen at 70 ℃ (see Subsection 3.2.2).

Table 3.1 display both the different crystallization time and the SAPO-34 zeotypes synthesized. These were two C-SAPO-34 and four hi-SAPO-34 zeotypes, with Si/Al-ratio of 0.2 and 0.3. The samples are labeled with the following abbreviations shown in Table 3.1: C-SAPO is short for conventional SAPO-34, hi-SAPO is short for hierarchical SAPO-34, the values 02 or 03 represent the theoretical Si/Al-ratio, and the values 24 or 119 represent the different crystallization time (hours) for the hi-SAPO-34 samples.

Table 3.1: Different crystallization times for C-SAPO-34 and hi-SAPO-34. The sample name is also described: C-SAPO is short for conventional SAPO-34, hi-SAPO is short for hierarchical SAPO-34, the values 02 or 03 represent the theoretical Si/Al-ratio, and the values 24 or 119 represent the different crystallization time (hours) for the hi-SAPO-34 samples.

Sample	Zeotype	Si/Al (theo.)	Crystallization time (h)
C-SAPO_02	C-SAPO-34	0.2	24
C-SAPO_03	C-SAPO-34	0.3	24
hi-SAPO_02:24	hi-SAPO-34	0.2	24
hi-SAPO_03:24	hi-SAPO-34	0.3	24
hi-SAPO_02:119	hi-SAPO-34	0.2	119
hi-SAPO_03:119	hi-SAPO-34	0.3	119

The sources of Si, Al and P were AS-40 Ludox (SiO_2 colloidal suspension in water, 40 wt.%), aluminium isopropoxide ($Al[OCH(CH_3)_2]_3$) and phosphoric acid (H_3PO_4, 85 wt.%) respectively, and the SDA used was tetraethylammonium hydroxide (TEAOH, 35 wt.%). The theoretical molar ratios are:

$$Al : P : (0.2, 0.3)Si : 0.9TEAOH : 28H_2O.$$

The meso-SDA used for the hi-SAPO-34 synthesis was TPOAc (dimethyloctadecyl [3-(trimethoxysilyl) propyl] ammonium chloride) and added with a theoretical molar ratio of meso-SDA/Al equal 0.1

An exemplified SAPO-34 procedure with a Si/Al equal 0.3 is described in the following. First, the phosphoric acid (9.2 g) and deionized water (20.9 g) was stirred before aluminium isopropoxide (16.3 g) was added slowly to a homogeneous mixture which was further stirred for 2 hours. Then, SiO_2 (3.6 g) and SDA (26.5 g) was added and the stirring continued for 15 minutes. For the hi-SAPO-34 samples, the meso-SDA (4.7 g) was then added and the mixture was stirred for another 15 minutes. Then the samples were placed in autoclaves in an oven at 190 ℃. The oven-time, which is the crystallization time, for the different SAPO-34 samples are, as mentioned, given in Table 3.1.

3.2 Fe-catalyst preparation

Detailed descriptions about the preparation of the Fe-catalysts are given in this section. In addition, the naming of the different samples are explained.

Difference between the ten catalysts are highlighted in Table 3.2, as well as the samples' name. The sample names uses the following abbreviations, given in the following parentheses: the catalysts Fe-ZSM-5 (FeZ), Fe-C-SAPO-34 (FeSA) and hi-Fe-SAPO-34 (hi-FeSA), and the preparation routes incipient wetness impregnation (W), ion-exchange (IE) and ion-exchange in an inert atmosphere (IEn). Five different groups of catalysts

were prepared: impregnated ZSM-5 (FeZ.W), ion-exchange ZSM-5 with $FeNO_3$ (FeZ.IE), ion-exchange ZSM-5 inert with $FeCl_2$ (FeZ.IEn), ion-exchange C-SAPO-34 inert with $FeCl_2$ (FeSA.IEn) and ion-exchange hi-SAPO-34 inert with $FeCl_2$ (hi-FeSA.IEn).

Table 3.2: Catalysts prepared for this thesis: six Fe-ZSM-5 catalysts (FeZ), two Fe-C-SAPO-34 (FeSA) and two hi-Fe-SAPO-34 (hi-FeSA). Support, iron precursor, which method used for introducing the metal (ion-exchange (I.E.) or incipient wetness impregnation (I.W.I.)), and the Si/Al-ratios for the support are listed. The solvent used for impregnation is given in parentheses for the I.W.I. samples.

Sample	Support	Iron precursor	Preparation route	Si/Al (theo.)
FeZ.W_13.5	H-ZSM-5_13.5	$Fe(III)(NO_3)_3$	I.W.I. (methanol/water)	13.5
FeZ.W_30	H-ZSM-5	$Fe(III)(NO_3)_3$	I.W.I. (water)	30
FeZ.IE_13.5	H-ZSM-5_13.5	$Fe(III)(NO_3)_3$	I.E.	13.5
FeZ.IE_30	H-ZSM-5_30	$Fe(III)(NO_3)_3$	I.E.	30
FeZ.IEn_13.5	NH_4-ZSM-5_13.5	$Fe(II)Cl_2$	I.E. (inert)	13.5
FeZ.IEn_30	NH_4-ZSM-5_30	$Fe(II)Cl_2$	I.E. (inert)	30
FeSA.IEn_02	C-SAPO_02	$Fe(II)Cl_2$	I.E. (inert, two-step, 70 °C)	0.2
FeSA.IEn_03	C-SAPO_03	$Fe(II)Cl_2$	I.E. (inert, two-step, 70 °C)	0.3
hi-FeSA.IEn_02	hi-SAPO_02:119	$Fe(II)Cl_2$	I.E. (inert, two-step, 70 °C)	0.2
hi-FeSA.IEn_03	hi-SAPO_03:119	$Fe(II)Cl_2$	I.E. (inert, two-step, 70 °C)	0.3

3.2.1 Fe-ZSM-5 preparation

The Fe-ZSM-5 catalysts were prepared from the zeolites NH_4-ZSM-5 Si/Al=13.5 and 30 (purchased from Süd Chemie and Zeolyst International respectively). Three different methods of introducing iron to the zeolite were performed: Incipient wetness impregnation, ion-exchange with iron(III)nitrate ($Fe(III)(NO_3)_3$) as iron-source, and ion-exchange under an inert atmosphere using iron(II)chloride ($Fe(II)Cl_2$) as iron-source. The different preparation routes are shown in Figure 3.1.

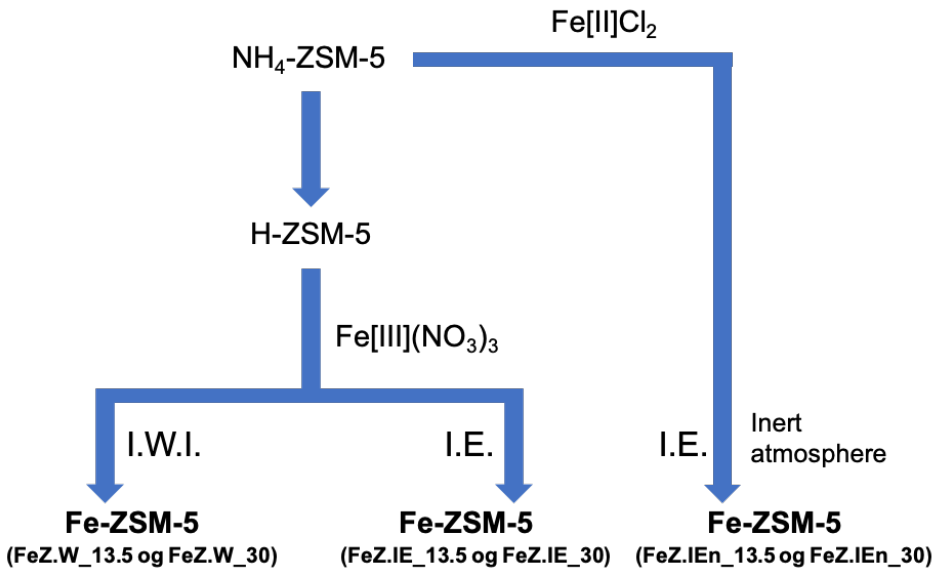

Figure 3.1: Overview of the preparation routes for the different Fe-ZSM-5 catalysts synthesized in this thesis. Six catalysts were prepared, labeled FeZ.W_13.5, FeZ.W_30, FeZ.IE_13.5, FeZ.IE_30, FeZ.IEn_13.5 and FeZ.IEn_30.

The samples FeZ.W_13.5 and FeZ.W_30 were prepared by incipient wetness impregnation with an iron loading of 5 wt.%. Water and methanol/water solution (50 vol.%) was used as solvents (see table 3.2). To use methanol as a solvent should improve an even distribution of the metal in the pores, due to the lower surface tension of the methanol solvent enabling the solvent to penetrate the pores more easily [11]. First, NH_4-ZSM-5 zeolites (Si/Al=13.5, 30) were pre-calcined under air at 550 ℃ for 6 hours with ramp rate of 1 ℃ min^{-1} to convert it to H-ZSM-5, and then dried at 110 ℃ for 12 hours prior to the impregnation.

For the impregnation, a volume equal to the pore volume of iron solution is introduced to the support. The iron solution used was prepared by measuring 1.7 g $Fe(NO_3)_3$ x $9\,H_2O$ (purchased from Sigma-Aldrich) and dissolve it in the solvent, so that the total volume of the solution equalled the measured pore volume. The amount of $Fe(NO_3)_3$ was calculated to give a theoretical 5 wt.% metal loading.

The pore volume was calculated by knowing the specific pore volume ($mL\,g^{-1}$), a, determined by a pore-volume test with the solvent and a known amount of zeolite ($\sim$ 1 g). For this synthesis, the value of a was 2.0 $mL\,g^{-1}$ and 0.8 $mL\,g^{-1}$ for FeZ.W_13.5 and FeZ.W_30 respectively. Then, a chosen amount of sample, m, was weighing out to calculate the pore volume, V_{pore}, from the value a: $V_{pore} = am$.

The H-ZSM-5 supports were impregnated by dropping iron solution equal to the pore volume slowly with a pipette over the support while mixing carefully. The impregnated samples were then dried for 30 minutes in air at room temperature whilst stirring occa-

sionally, followed by 12 hours at 110 ℃ in a furnace. Finally, the samples were calcined at 550 ℃ for 4 hours with a ramp rate of 5 $^{\circ}\mathrm{C\,min^{-1}}$. This method was inspired by the procedure used in Zhang and Yang [13].

The samples FeZ.IE_13.5 and FeZ.IE_30 were prepared by ion-exchange of H-ZSM-5 with $Fe(NO_3)_3$. This method was also inspired by the procedure done by Zhang and Yang [13]. First, NH_4-ZSM-5 zeolites (Si/Al=13.5, 30) were pre-calcined to H-ZSM-5 at 550 ℃ for 6 hours with ramp rate of 1 $^{\circ}\mathrm{C\,min^{-1}}$. Following, 2 g of H-ZSM-5 was added to 250 mL of a 0.1 $\mathrm{mol\,L^{-1}}$ $Fe(NO_3)_3$ solution, made from $Fe(NO_3)_3$ x $9\,H_2O$ (purchased from Sigma-Aldrich) diluted with deionized water. This mixture was stirred for 24 hours at room temperature, and then filtered and dried overnight at 40 ℃. Finally, the samples were calcined in air at 550 ℃ for 4 hours with a ramp rate of 1 $^{\circ}\mathrm{C\,min^{-1}}$. The exchange degree used was 125 $\mathrm{mL_{sol}\,g^{-1}_{zeolite}}$, where *sol* is short for the 0.1 $\mathrm{mol\,L^{-1}}$ Fe-solution.

The samples FeZ.IEn_13.5 and FeZ.IEn_30 were prepared by ion-exchange of NH_4-ZSM-5 (Si/Al=13.5, 30) with $Fe(II)Cl_2$ under an inert atmosphere. This procedure was based on the work proposed by Skoglundh et al. and Brandenberger et al. [11, 16]. The iron solution used was 0.1 $\mathrm{mol\,L^{-1}}$ $Fe(II)Cl_2$, prepared from $Fe(II)Cl_2$ x4 H_2O (Purchased from Sigma-Aldrich) dissolved in deionized water under nitrogen. The exchange degree was 22 $\mathrm{mL_{solv}\,g^{-1}_{zeolite}}$. The NH_4-ZSM-5 was added to $Fe(II)Cl_2$-solution under nitrogen and stirred overnight. The resulting Fe-ZSM-5 products were centrifuged and washed with deionized water until the washing water was chlorine free. This was confirmed by a simple chlorine test using 0.8 $\mathrm{mol\,L^{-1}}$ HNO_3 and 1 $\mathrm{mol\,L^{-1}}$ $AgNO_3$. Finally, the products were dried overnight in air at 70 ℃ and heat treated under N_2 at 500 ℃ for 3 hours with a ramp rate of 4 $^{\circ}\mathrm{C\,min^{-1}}$.

3.2.2 Hierarchical and conventional Fe-SAPO-34 preparation

The four Fe-C-SAPO-34 and Fe-hi-SAPO-34 catalysts, FeSA.IEn_02, FeSA.IEn_03, hi-FeS.IEn_02 and hi-FeS.IEn_03, were prepared by a two-step ion-exchange method, inspired by the procedure by Xu et al. [33]. For the first step, the SAPO-34 samples in its proton form were ion-exchanged with a 0.1 $\mathrm{mol\,L^{-1}}$ ammonium nitrate solution, NH_4NO_3 (Purchased from Sigma-Aldrich). The zeotypes were added to a pre-heated NH_4NO_3-solution (80 ℃) under nitrogen and stirred for 1 hour, followed by centrifuging and washing with deionized water several times and, finally, dried overnight in air at 70 ℃. This resulted in NH_4-SAPO-34 products.

For the second step, the samples were ion-exchanged with 0.1 $\mathrm{mol\,L^{-1}}$ $Fe(II)Cl_2$, prepared from $Fe(II)Cl_2$ x $4\,H_2O$ (Purchased from Sigma-Aldrich) under nitrogen. The NH_4-SAPO-34 was added to a pre-heated $Fe(II)Cl_2$-solution (70 ℃) under nitrogen and stirred for 2 hours, followed by centrifuging and washing with deionized water until it was confirmed that the washing water was chlorine free with the same test as mentioned above. Finally,

the samples were dried overnight in air at 70 ℃, and heat treated under nitrogen at 500 ℃ for 3 hours with a ramp rate of 4 $^{\circ}\mathrm{C}\,\mathrm{min}^{-1}$. For both steps the exchange degree was set to 30 $\mathrm{mL}_{\mathrm{solv}}\,\mathrm{g}^{-1}_{\mathrm{zeotype}}$.

3.3 Characterization

The samples were characterized by XRD, ICP-MS, N_2 physisorption, TPR and chemisorption. Details about those techniques are described in this section.

3.3.1 X-Ray Diffraction

The XRD analysis of the powder samples were performed using a Bruker D8 Fucos X-Ray Diffractometer with a Copper-anode. The 2θ scanning was set from 5° to 65° for the ZSM-5 samples, and from 5° to 55° for the SAPO-34 samples. The divergence slit was 0.2 mm, and the step size was 0.02285° used with one second per step. The XRD-data was analyzed by the analysis program DIFFRAC.EVA, and the diffraction patterns were plotted by offsetting the y-values and were not normalized.

3.3.2 N_2 Physisorption

The sample's specific surface area and pore size distribution was estimated by N_2 physisorption. For this thesis, two instrument were available: S Micrometrics Tri Star II 3020 and a Tri Star 3000 Surface Area and Porosity Analyszer with N_2 as adsorbent. The amount of sample analyzed was approximately 100 mg. First, the sample was weighed. Second, the sample's surface and pores were cleaned for any adsorbed contaminates by degassing with a VacPrep 061 Degasser. In the degassing procedure the sample was put under vacuum at room temperature for approximately one hour, followed by 12 hours under vacuum at 200-250 ℃. Finally, the sample was placed in the instrument. The sample was cooled down to 77 K by liquid nitrogen during the analysis.

3.3.3 Temperature-Programmed Reduction of H_2

The H_2-TPR experiment was carried out using a TPX Altamira BenchCAT Hybrid with TCD detection. The samples were not pretreated in oxygen due to errors with the instrument's gas supply of oxygen. As a consequence, the samples may not have been completely oxidized prior to the analysis. The analysis was run over three steps, and a sample mass of approximately 0.1 g was used. First, the sample (0.1 g) was loaded in an

u-shaped quartz reactor with quartz wool and treated with argon for one hour at 150 ℃. Second, the sample was cooled down to room temperature (40 ℃). Third, the TPR-analysis was performed by flowing 7% H_2/Ar over the sample up to 900 ℃ with a ramp rate of 10 °C min^{-1}. For this thesis, H_2-TPR was analyzed to estimate the reduction temperatures for further analysis of dispersion by chemisorption. Four samples were tested, one from each synthesis: FeZ.W_30, FeZ.IE_13.5, FeZ.IEn_13.5 and FeSA.IEn_03.

3.3.4 ICP-MS

ICP-MS was performed mainly to investigate the iron loading of the different samples, but the Si/Al-ratios could also be checked for the molecular sieves. The analysis was performed by Syverin Lierhagen (IKJ, NTNU) using a high-resolution ICP-MS ELEMENT 2 instrument.

The sample preparation was done by weighing the samples (15-40mg) in a Teflon tube (25 ml) and decompose it with the acids HNO_3 (1.5 ml, concentrated) and HF (0.5 ml, concentrated (40%)). Then the decomposed sample was added to a larger Teflon flask and diluted with deionized water to a total mass of approximately 216.6 g. Finally, the solution was added to Teflon tube (16 ml) before the ICP-MS analysis. Three blank samples were also analyzed.

3.3.5 Chemisorption

The metal dispersion was determined by CO chemisorption using a Micromeritics ASAP 2020 instrument. The sample (0.2-0.23 g) was loaded in an u-shaped quartz reactor with quartz wool. Then the sample was evacuated in He at 35 ℃ for 60 minutes, followed by a reduction step under H_2 at 700 ℃ for 60 minutes, before cooled down to room temperature under He atmosphere. The chemisorption was measured at 35 ℃ over a pressure range of 0.1 to 450 mmHg using CO gas for the first adsorption-isotherm and for the readsorption. The dispersion was calculated from the difference results for the two isotherms. It was assumed a stoichiometric Fe:CO = 2.

3.4 Selective catalytic reduction of NO_X (NH_3-SCR)

Activity measurements towards NH_3-SCR were performed for five Fe-catalysts, their support and SiC, listed in the following Table 3.3.

Table 3.3: Samples tested for catalytic activity. Iron precursor, which method used for introducing the metal and the Si/Al-ratio of the zeolite or zeotype are listed. The crystallization time is given in parentheses for the hi-SAPO-34 samples.

Sample	Iron precursor	Synthesis method	Si/Al (theo.)
H-ZSM-5			13.5
FeZ.W_13.5	$Fe(III)(NO_3)_3$	I.W.I. (methanol/water)	13.5
FeZ.IE_13.5	$Fe(III)(NO_3)_3$	I.E.	13.5
FeZ.IEn_13.5	$Fe(II)Cl_2$	I.E. (inert)	13.5
C-SAPO_03			0.3
hi-SAPO_03:119			0.3
FeSA.IEn_03	$Fe(II)Cl_2$	I.E. (inert, two-step, 70 °C)	0.3
hi-FeSA.IEn_03 (119h)	$Fe(II)Cl_2$	I.E. (inert, two-step, 70 °C)	0.3
SiC			

The catalytic performance towards NH_3-SCR was tested in a packed bed reactor using a PID microactivity-efficient unit coupled with a quadrupole MS (Hiden Analytical). The gas supply used for the experiment was Ar, NO, O_2, NH_3 and NO_2. The gas flow was controlled by El-Flow thermal mass flow controllers which were calibrated using a bubble column. The calibration is shown in Appendix C.5. The reactor was a Stainless Steel (316SS) tubular Fixed Bed Reactor (length = 304.8 mm, internal diameter = 9.1 mm) with a porous plate (20 µm) ensuring the sample to be located in the isothermal zone of the furnace.

The samples were prepared by measuring 0.100 g of the sample and 3.5269 g of SiC (53-90 µm) and then mechanically mix it together in a mortar. The amount of catalyst and SiC correspond to a reactor volume of 3 mL.

For the experiments, the total gas flow was set to 250 $mL\,min^{-1}$ which gave a space velocity of 15000 h^{-1} or 30000 $mL\,g_{cat}^{-1}\,h^{-1}$. The temperatures tested were in the range of 250 °C to 450 °C, and the feed gas composition was 600 ppm NO, 600 ppm NH_3, 10 % O_2 and Ar. The overall session is shown in Figure 3.2 and the flows used for the session are listed in Table 3.4.

Figure 3.2: Overview of the session used for activity measurements towards NH_3-SCR. The red zones illustrates when bypass is off, gas flow through the reactor and the blue zone illustrates when bypass in on. It is also shown the times: activation for 60 minutes, bypass on for 10 minutes, SCR for 30 minutes and the cooling time is fixed at 15 minutes.

Table 3.4: Overview of the flow used for the NH_3-SCR session.

	Ar flow ($mL\,min^{-1}$)	O_2 flow ($mL\,min^{-1}$)	NO flow ($mL\,min^{-1}$)	NH_3 flow ($mL\,min^{-1}$)	Total flow ($mL\,min^{-1}$)
Activation	87.5	125	37.5	0	250
Bypass on	57.5	125	37.5	30	250
SCR (bypass off)	57.5	125	37.5	30	250
Cooling (bypass off)	250	0	0	0	250

The catalysts were activated prior to the measurements under a feed gas composition of 600 ppm NO and 10 % O_2 at 450 ℃ for 60 minutes. Degreening of the catalyst occur under the activation, which for example deactivates very active and unstable sites. The SCR reactions was tested for five different temperature, 450 ℃, 400 ℃, 350 ℃, 300 ℃ and 250 ℃. For each temperature there were two stages with the same feed gas composition: First 10 minutes with bypass on for calibrating the MS, then the SCR reaction for 30 minutes. Bypass means leading the gas flow past, and not through, the reactor. Cooling under Ar was performed between the temperatures.

The resulting MS-data was analyzed in ExCel and the analysis is described in Appendix C.3. The calculations were based on the MS-data (pressure), and not converted to concentration as a consequence of the time limit.

Chapter 4

Results

Results from the characterization techniques and the catalytic testing are given in this chapter and will be discussed in the next chapter. First are the characterization results for the SAPO-34 zeotypes prepared shown. These are results from elemental analysis, XRD and N_2 physisorption. Then, results from the characterization of the Fe-catalysts are presented: XRD, N_2 physisorption, TPR, ICP-MS and chemisorption. Finally are the results from the activity measurements shown as NO-conversion and the MS-data for NO and N_2. Additional results not presented in this chapter, are shown in Appendix B. Further, results given as *NA* means not analyzed, and results given as "-" had errors in the analysis such that no valid results were measured.

4.1 Characterization of synthesized SAPO-34

In this section the results of the synthesized SAPO-34 samples are presented. Of all synthesized zeotypes, four samples were believed to be synthesized more successfully and therefor ion-exchanged with iron to Fe-catalysts. The background for the choice is outlined in the discussion section. XRD, ICP-MS and N_2 physisorption results are shown in this section. In addition SEM-images were taken by Daniel Ali (IKJ, NTNU) for two samples and are given in Appendix B.1.

Elemental analysis by ICP-MS was used to measure the Si/Al-ratio. These results are presented in Table 4.1, and the calculations are explained in Appendix C.3. The samples hi-SAPO_02:24 and hi-SAPO_03:24 were not analyzed for ICP-MS because XRD, SEM and N_2 physisorption results showed collapse in the structure. This is explained in the discussion (Section 5.1).

Table 4.1: ICP-MS results: Si/Al-ratio for the synthesized SAPO zeotypes. Calculations are shown in Appendix C.1, and descriptions of the sample names are given in Table 3.1.

Sample	Si/Al (theo.)	Si/Al
C-SAPO_02	0.2	0.2
C-SAPO_03	0.3	0.2
hi-SAPO_02:24	0.2	NA
hi-SAPO_03:24	0.3	NA
hi-SAPO_02:119	0.2	0.3
hi-SAPO_03:119	0.3	0.4

The samples were analyzed by XRD, and the diffractogram are listed in the following figures. The two figures, Figure 4.1 and Figure 4.2, show the diffractogram for the C-SAPO-34 samples and the hi-SAPO-34 samples respectively. In addition, a diffractogram which compare a C-SAPO-34 and a hi-SAPO-34 sample are shown in Figure 4.3, to highlight the difference in the intensity. The CHA-structure is shown in all figures to compare to the original diffraction pattern.

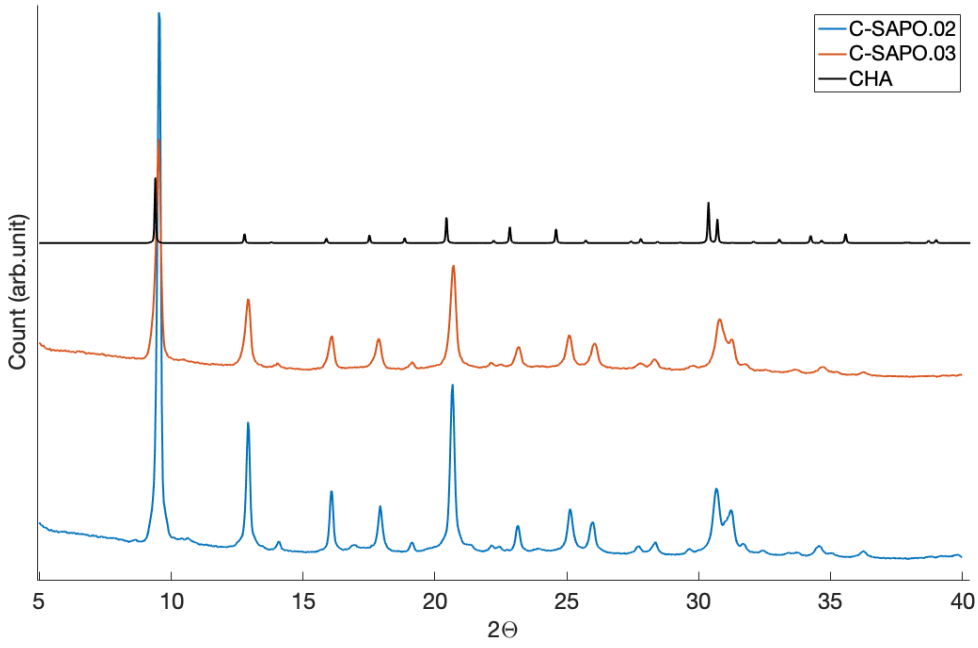

Figure 4.1: Diffractogram for SAPO-34 synthesized, C-SAPO_02 and C-SAPO_03, and the CHA-structure. The plot has arbitrary units at the vertical axis. Structure data for the CHA-structure is collected from IZA Synthesis Commission [15].

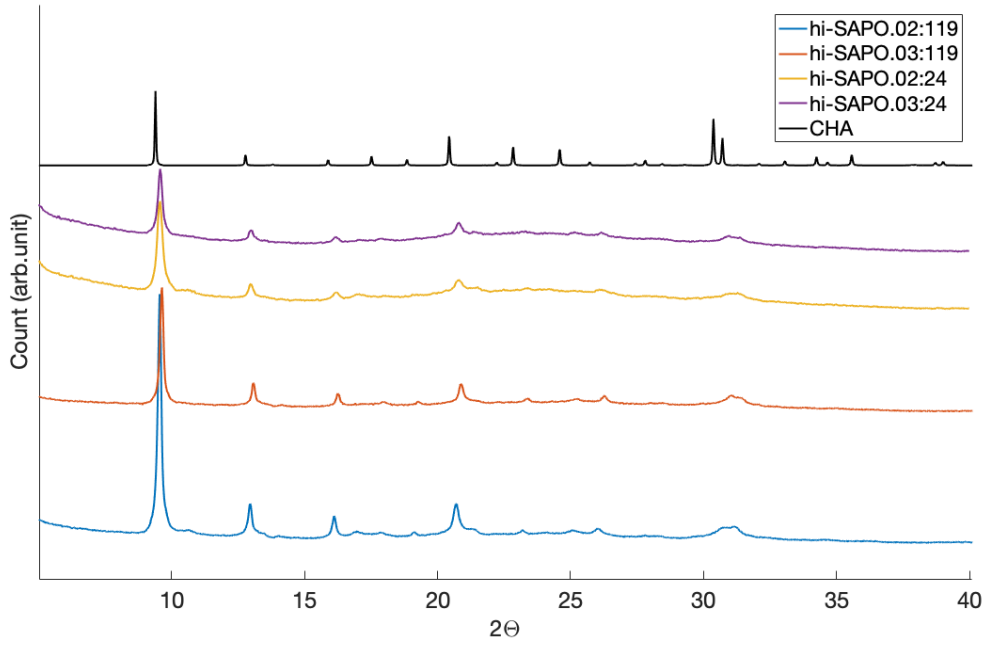

Figure 4.2: Diffractogram for the CHA-structure and hi-SAPO-34 zeotypes synthesized with two different crystallization times, 24 hours and 119 hours: hi-SAPO_02:24, hi-SAPO_03:24, hi-SAPO_02:119 and hi-SAPO_03:119. The plot has arbitrary units at the vertical axis. Structure data for the CHA-structure is collected from IZA Synthesis Commission [15].

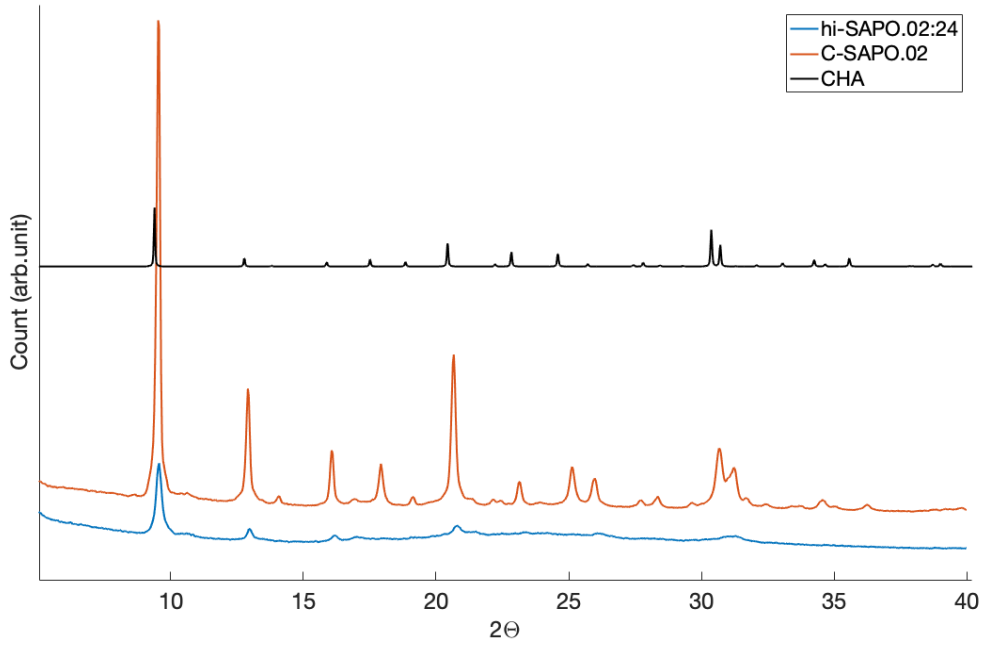

Figure 4.3: Diffractogram highlighting the difference in intensity between the C-SAPO-34 and hi-SAPO-34 zeotypes. C-SAPO_02 and hi-SAPO-_02:24 are plotted, in addition to the CHA-structure. The plot has arbitrary units at the vertical axis. Structure data for the CHA-structure is collected from IZA Synthesis Commission [15].

N_2 physisorption results are shown in Table 4.2 and in the Figures 4.4, 4.5 and 4.6. The samples were analyzed to characterize the pore distribution and surface area for the samples. BET surface area, pore size and pore volumes (total, micro and macro) are shown in Table 4.2. The figures show the adsorption and desorption isotherms and the BJH pore size distribution.

Table 4.2: N_2 physisorption results for the synthesized SAPO zeotypes. BET specific surface area, pore size, total pore volume (V_{total}), micropore volume (V_{micro}) and mesopore volume (V_{meso}) are listed. Descriptions of the sample names are given in Table 3.1.

Sample	Specific surface area ($m^2\,g^{-1}_{BET}$)	Pore size (BET) (nm)	V_{total} ($cm^3\,g^{-1}$)	V_{micro} ($cm^3\,g^{-1}$)	V_{meso} ($cm^3\,g^{-1}$)
C-SAPO_02	518	2.2	0.28	0.23	0.05
C-SAPO_03	488	2.0	0.25	0.21	0.04
hi-SAPO_02:24	346	5.4	0.46	0.07	0.39
hi-SAPO_03:24	318	6.2	0.49	0.05	0.44
hi-SAPO_02:119[a]	434	-	-	-	-
hi-SAPO_03:119	455	2.9	0.33	0.15	0.18

[a]The pore characterization for the hi-SAPO_02:119 sample was not measured due to errors for the analysis, however a BJH-curve and adsorption isotherm was measured and shown in Figure 4.6a.

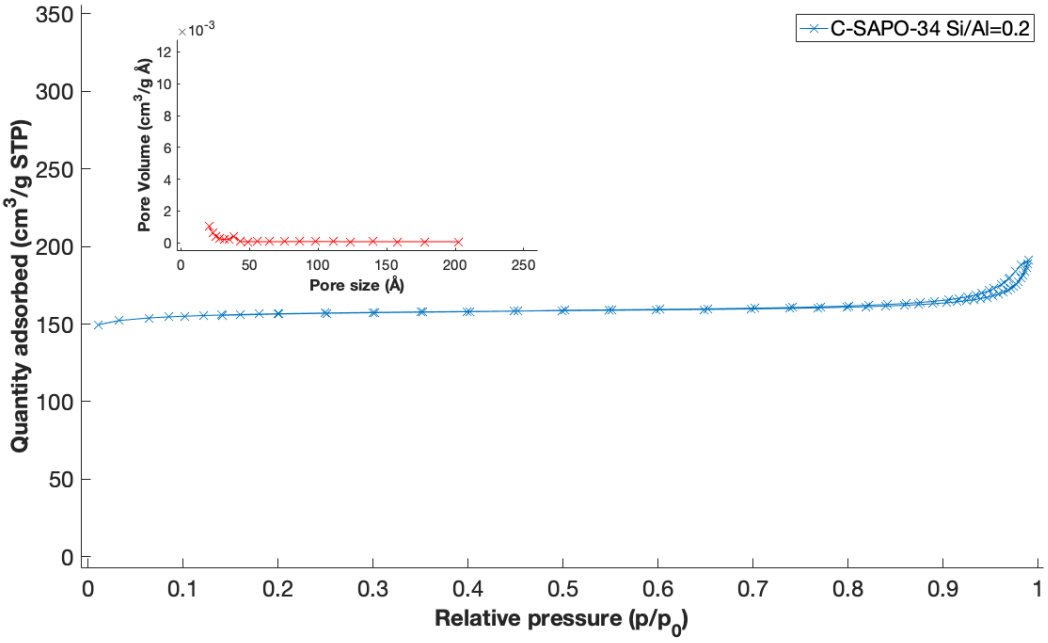

(a) C-SAPO_02.

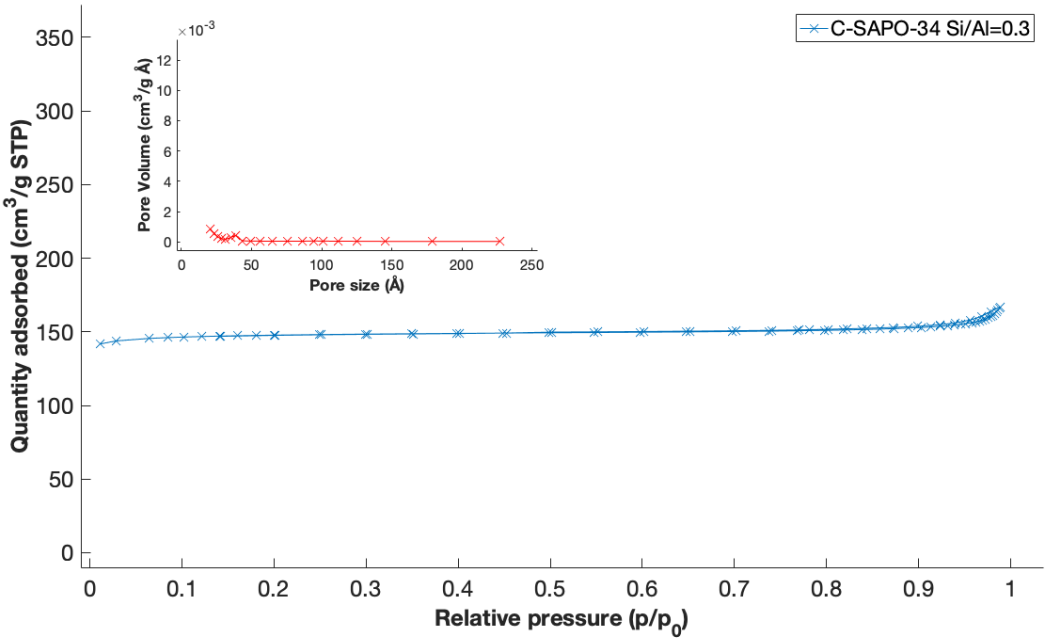

(b) C-SAPO_03

Figure 4.4: N_2 adsorption and desorption isotherm and BJH pore size distribution for synthesized C-SAPO-34 zeotypes. Note: the ole sample names are shown in the figure.

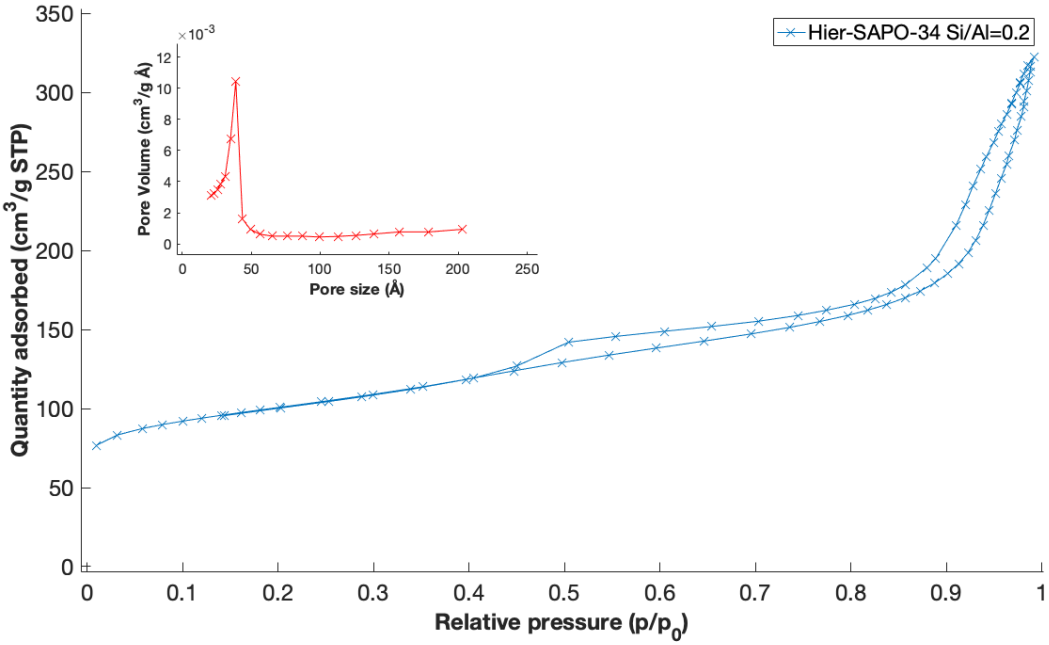

(a) hi-SAPO_02:24.

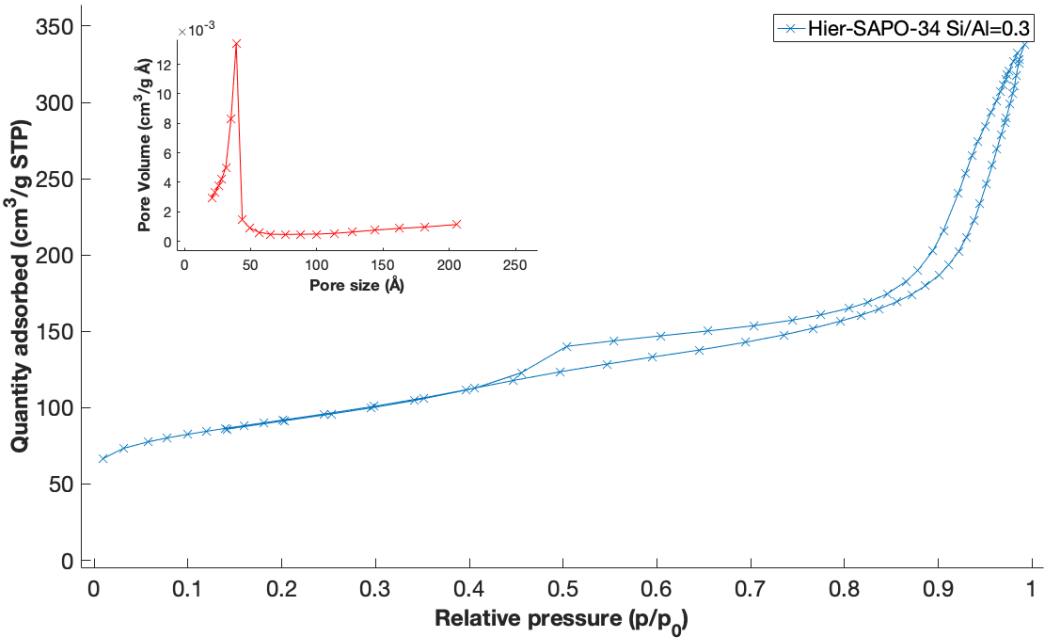

(b) hi-SAPO_03:24.

Figure 4.5: N_2 adsorption and desorption isotherm and BJH pore size distribution for hi-SAPO-34 zeotypes with 24 hour crystallization. Note: the ole sample names are shown in the figure.

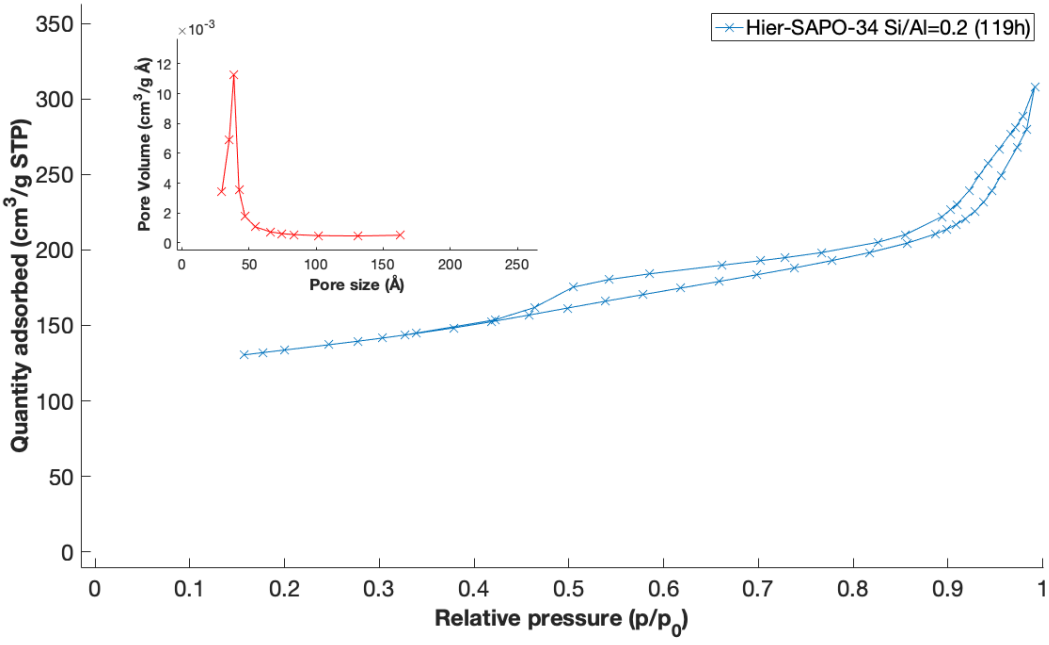

(a) hi-SAPO_02:119.

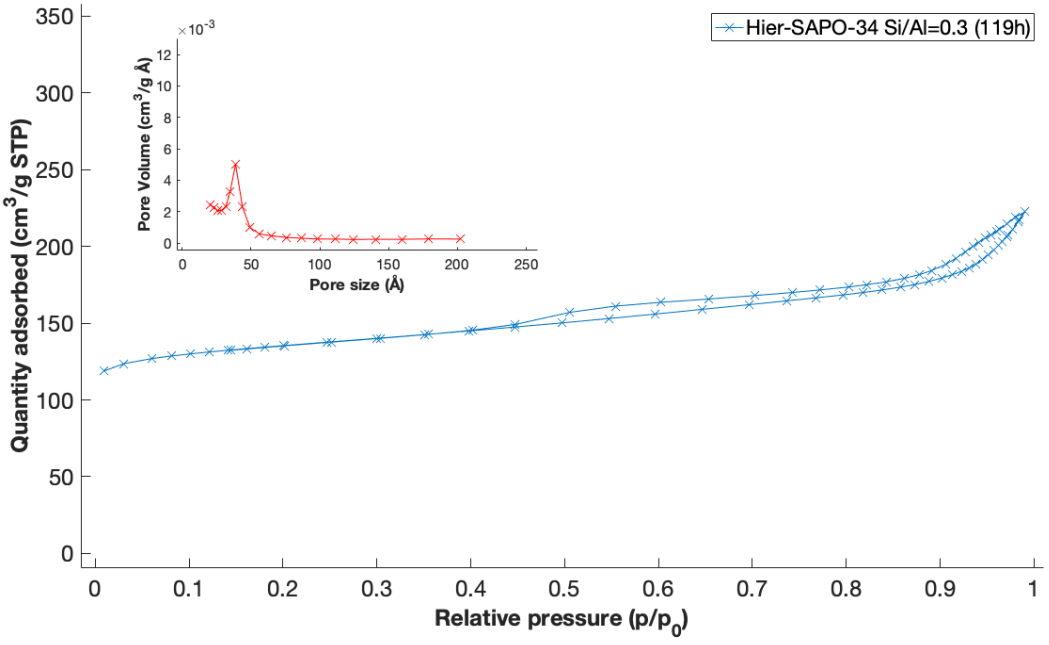

(b) hi-SAPO_03:119.

Figure 4.6: N_2 adsorption and desorption isotherm and BJH pore size distribution for hi-SAPO-34 zeotypes with 119 hour crystallization. Note: the ole sample names are shown in the figure.

4.2 Characterization of Fe-catalysts

Six Fe-ZSM-5, two Fe-C-SAPO-34 and two Fe-hi-SAPO-34 catalysts were prepared, and the characterization results from XRD, N_2 physisorption, TPR, ICP-MS and chemisorption are shown in the following subsections. The sample names are the same as described in Methods in Table 3.2. Note that the hi-SAPO-34 supports with 119 hours crystallization are those used as support for the catalysts, and those are named hi-FeSA.IEn_02 and hi-FeSA.IEn_03.

4.2.1 X-Ray Diffraction

Diffractogram obtained from XRD-analysis are shown in this subsection. Figure 4.7 shows the diffractogram for the six Fe-ZSM-5 catalysts with the MFI-structure from the angles 5 - 30 2θ (Figure 4.7a) and a diffractogram highlighting the last angles, 30 - 65 2θ (Figure 4.7b). In Appendix B.3 are the complete diffractogram from 5 - 65 2θ shown in Figure B.2. Further, the diffractogram for the Fe-C-SAPO-34 catalysts are shown in Figure 4.8. And for the Fe-hi-SAPO-34 catalysts are the diffraction pattern shown in Figure 4.9.

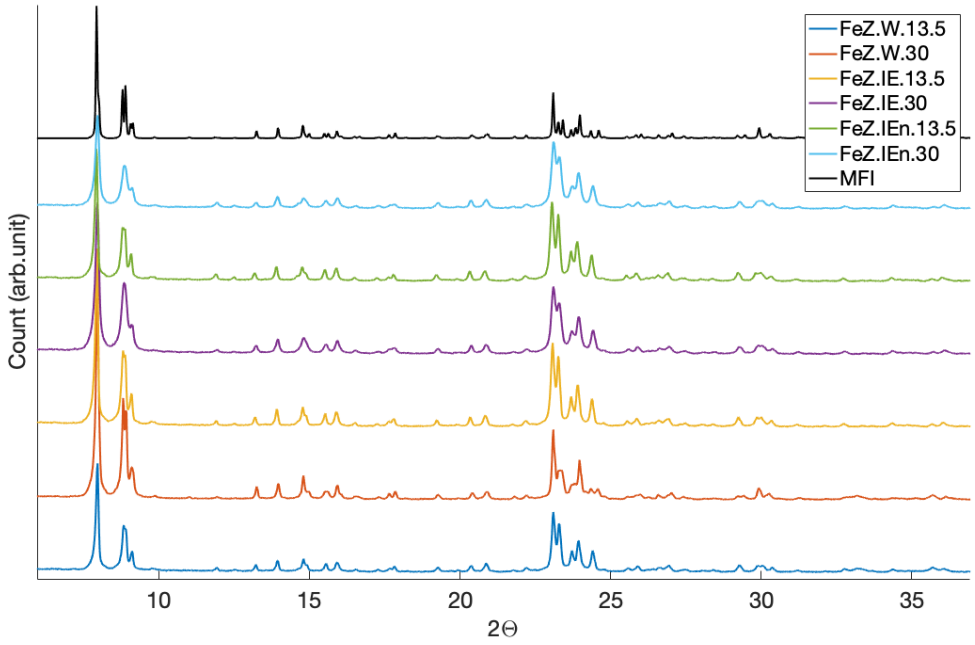

(a) $2\theta : 5 - 30$

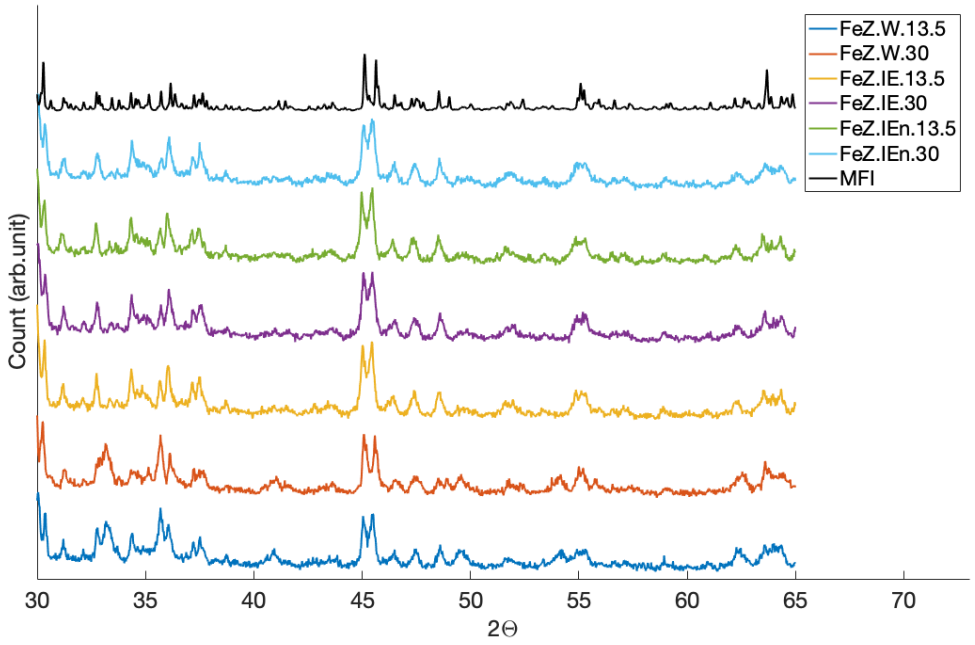

(b) $2\theta : 30 - 65$

Figure 4.7: Two diffractogram for Fe-ZSM-5 catalysts and the MFI-structure are illustrated: for $2\theta : 5 - 30$ (a) and for $2\theta : 30 - 65$ (b). The catalysts plotted are FeZ.W.13.5, FeZ.W.30, FeZ.IE.13.5, FeZ.IE.30, FeZ.IEn.13.5, FeZ.IEn.30. The plots has arbitrary units at the vertical axis. Structure data for the MFI-structure is collected from IZA Synthesis Commission [15].

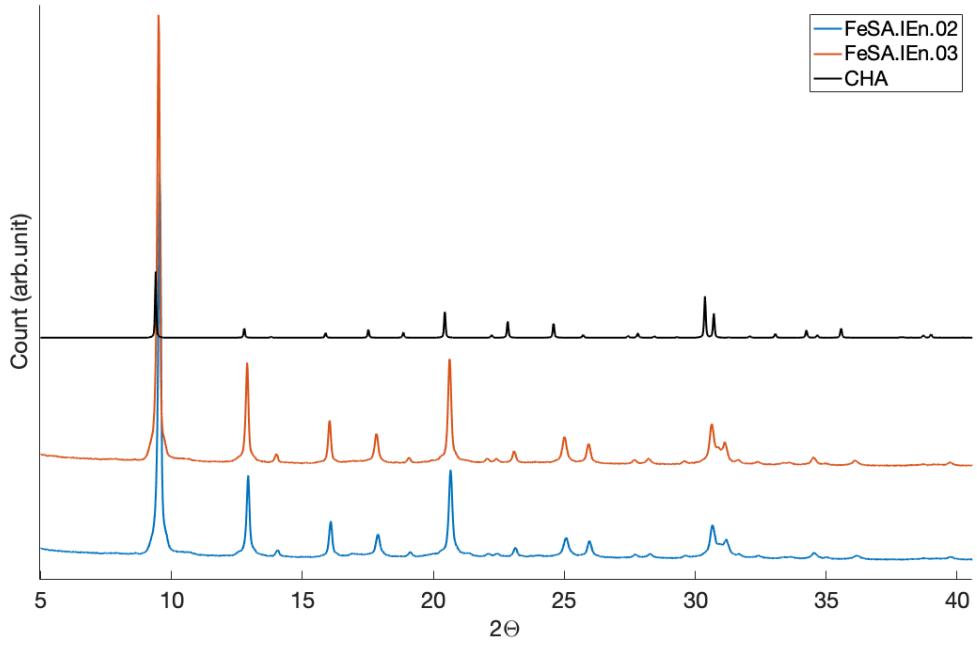

Figure 4.8: Diffractogram for Fe-C-SAPO-34 catalysts, FeSA.IEn.02 and FeSA.IEn.03, and the CHA-structure. The plot has arbitrary units at the vertical axis. Structure data for the CHA-structure is collected from IZA Synthesis Commission [15].

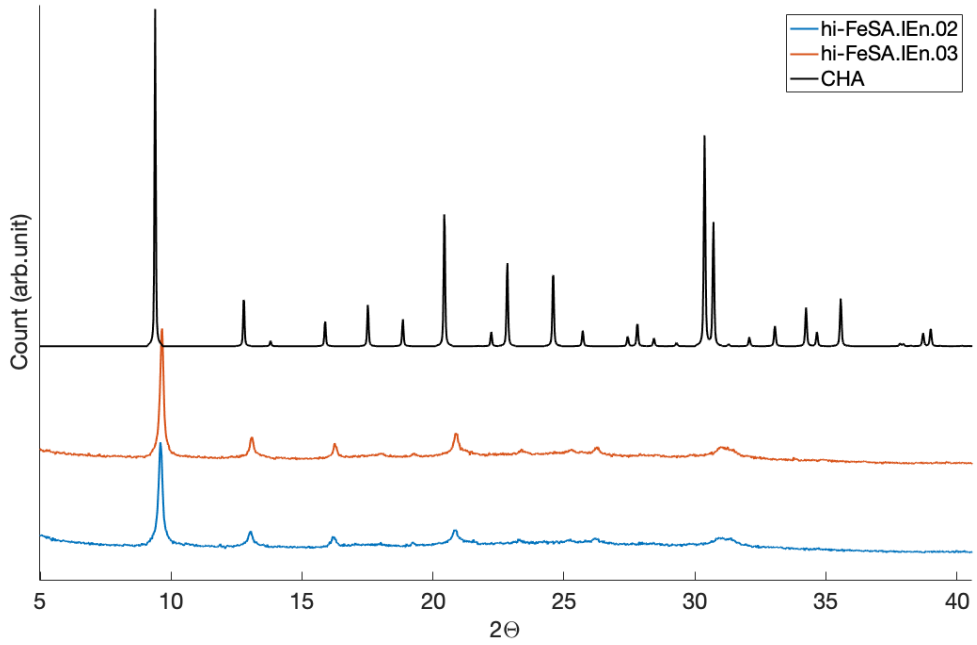

Figure 4.9: Diffractogram for Fe-hi-SAPO-34 catalysts, hi-FeSA.IEn.02 and hi-FeSA.IEn.03, and the CHA-structure. The plot has arbitrary units at the vertical axis. Structure data for the CHA-structure is collected from IZA Synthesis Commission [15].

4.2.2 N_2 Physisorption

N_2-physisorption was used to estimate the BET surface area and pore size for the Fe-ZSM-5 and Fe-C-SAPO-34 samples. In addition, the BJH pore size distribution was also determined for the Fe-hi-SAPO-34 sample hi-FeSA.IEn_03 to analyze presence of mesopores in the structure. Figure 4.10 show the BJH pore distribution and the adsorption and desorption isotherm for this sample. The adsorption and desorption isotherms for the other samples are shown in Appendix B.5. All samples were analyzed for N_2-physisorption, except hi-FeSA.IEn_02.

The following table lists the BET surface area and the pore size of the samples. The surface areas for Fe-ZSM-5 catalysts were in the range of 325-393 $m^2\,g_{BET}^{-1}$.

Table 4.3: N_2 physisorption results for the Fe-catalysts. BET surface area and the pore size are listed. Descriptions of the sample names are given in Table 3.2.

Catalyst	Specific surface area ($m^2\,g_{BET}^{-1}$)	Pore size (BET) (nm)
FeZ.W_13.5	393	1.4
FeZ.W_30	325	1.6
FeZ.IE_13.5	364	2.1[a]
FeZ.IE_30	377	1.5
FeZ.IEn_13.5	352	1.5
FeZ.IEn_30	340	1.5
FeSA.IEn_02	494	1.8
FeSA.IEn_03	464	-
hi-FeSA.IEn_02	NA	NA
hi-FeSA.IEn_03	380	3.2[a]

[a] N_2 physisorption was measured with two different instrument, and the samples (a) was measured with a different instrument compared to the rest.

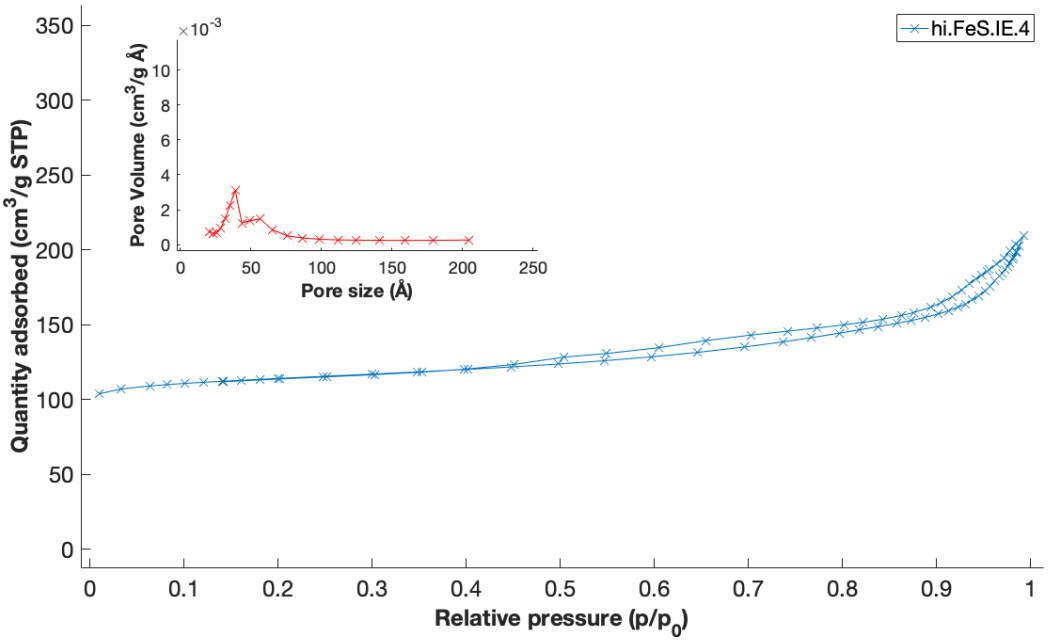

Figure 4.10: N_2 adsorption and desorption isotherm and the BJH pores size distribution for the sample hi-FeSA.IEn_03. Note: the ole sample name is shown in the figure.

4.2.3 Temperature-Programmed Reduction of H_2

Four samples were tested, and no H_2-consumption was detected for the ion-exchanged samples, FeZ.IE_13.5, FeZ.IEn_13.5 and FeSA.IEn_03. However, for the impregnated sample, FeZ.W_30, several peaks were located as shown in the H_2-TPR profile in Figure 4.11. The first peak was shown in the area of 380 ℃, the second at 580 ℃ and the third at 750 ℃.

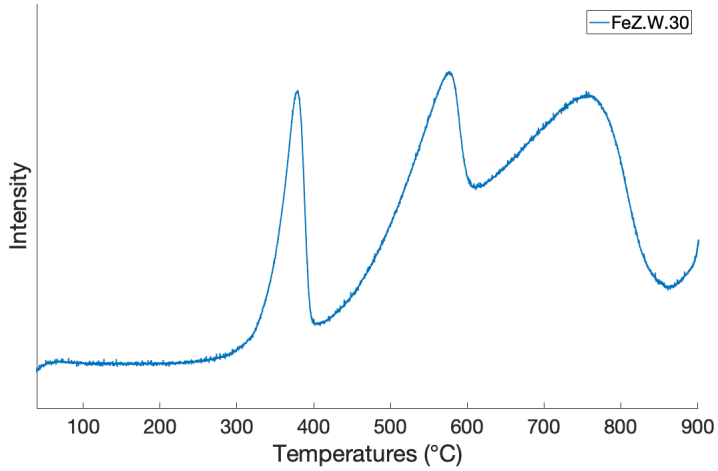

Figure 4.11: H_2-TPR profile for the FeZ.W_30 catalyst measured over a temperature range from 40 to 900 ℃.

4.2.4 ICP-MS and Chemisorption

The ICP-MS and chemisorption results are presented in Table 4.4. The Fe loading (wt.%) and the calculated Si/Al-ratios are listed from the elemental analysis. The Si/Al-calculations are explained in Appendix C.1.

The dispersion results and the measured adsorbed volume for the difference isotherm (irreversible chemisorption), are both shown in Table 4.4. The adsorption isotherms, upper, lower and difference, are illustrated for three of the samples in Appendix B.4, and the dispersion calculations are described in Appendix C.2. The Fe-hi-SAPO-34 catalysts are not analyzed with chemisorption, and the Fe-C-SAPO-34 catalysts showed no observed volume for the difference results, such that no dispersion calculation are measured.

Table 4.4: ICP-MS and chemisorption results for the Fe-catalysts. Iron loading, Si/Al-ratios and chemisorption difference results for dispersion and volume adsorbed gas are listed. Descriptions of the sample names are given in Table 3.2.

Catalyst	Fe loading (wt.%)	Si/Al	Si/Al (theo.)	Dispersion (%, diff.)	Volume adsorbed ($cm^3\,g^{-1}$, diff.)
FeZ.W_13.5	5.2	12.9	13.5	8	0.4
FeZ.W_30	4.8	146.5[a]	30	1	0.1
FeZ.IE_13.5	0.5	13.3	13.5	10	0.1
FeZ.IE_30	0.4	16.1	30	19	0.2
FeZ.IEn_13.5	1.1	13.3	13.5	38	0.8
FeZ.IEn_30	0.9	15.6	30	38	0.7
FeSA.IEn_02	0.8	0.2	0.2	NA	NA
FeSA.IEn_03	0.6	0.2	0.3	NA	0.0
hi-FeSA.IEn_02	0.6	0.2	0.2	NA	NA
hi-FeSA.IEn_03	0.4	0.3	0.3	NA	0.0

[a]The high Si/Al-ratio was due to a mix-up with the labeling of a impregnated samples ZSM-5 with a different Si/Al-ratio. See appendix A.1.

4.3 Activity measurements

Five catalysts were tested towards NH_3-SCR: FeZ.W_13.5, FeZ.IE_13.5, FeZ.IEn_13.5, FeSA.IEn_03 and hi-FeSA.IEn_03. The NO-conversion as a function of temperature are shown in Figure 4.12. Figure 4.12a shows the Fe-ZSM-5 catalysts and the H-ZSM-5 support. Figure 4.12b shows the Fe-SAPO-34 catalysts and their supports C-SAPO_03 and hi-SAPO_03:119. Further, the MS-data for NO and N_2 as a function of time are shown for Fe-ZSM-5 catalysts in Figure 4.13 and Fe-SAPO-34 catalysts in Figure 4.14.

Figure 4.12 shows NO-conversions for five temperatures, 450, 400, 350, 300 and 250 °C, with the error bar. The calculations are explained in Appendix C.3. For the SAPO-34

supports, seen in Figure 4.12b, the NO-conversions were set to 0 % as the NO-conversions measured were negative.

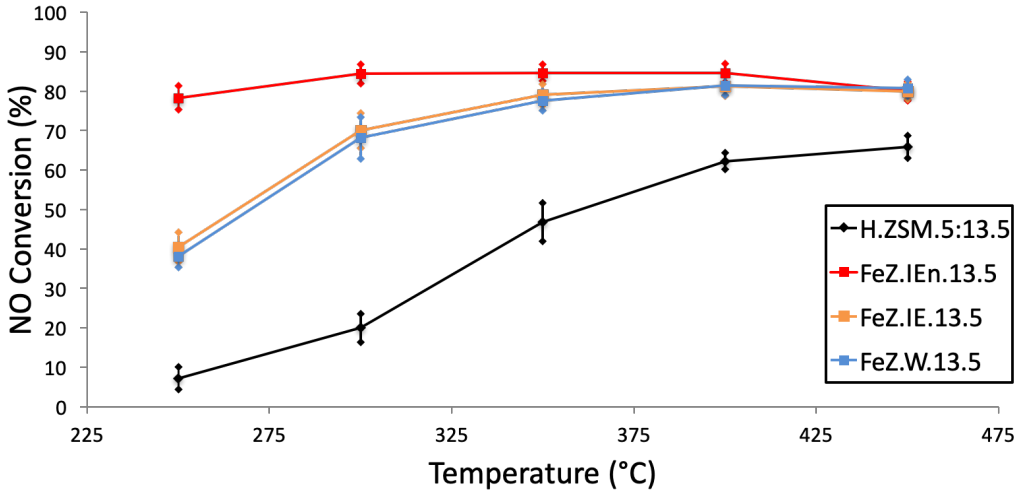

(a) Fe-ZSM-5

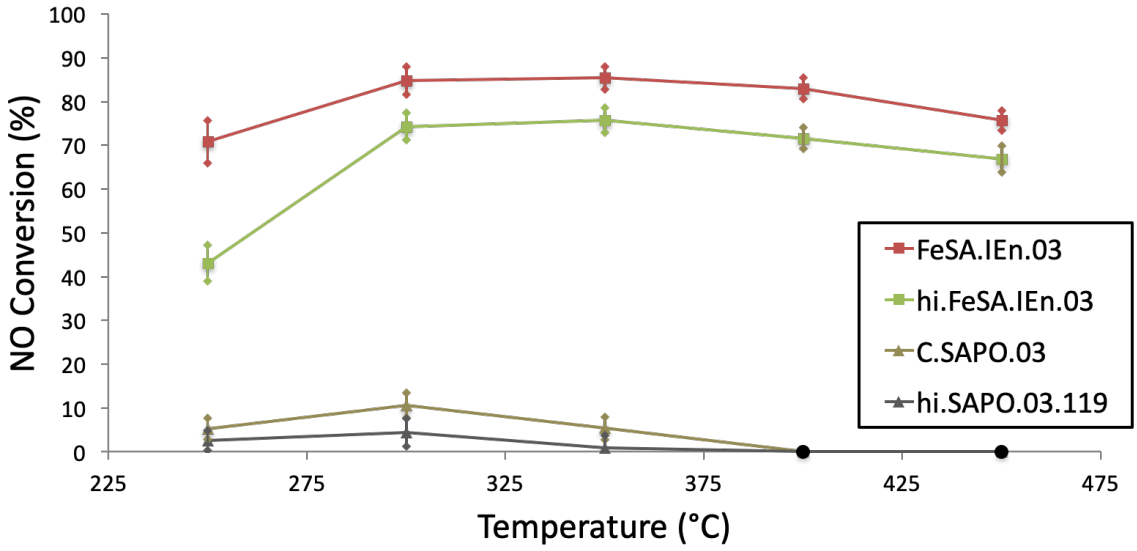

(b) Fe-SAPO-34

Figure 4.12: NO-conversion during NH_3-SCR as a function of temperature (°C) are shown for ZSM-5 catalysts (a) and SAPO-34 catalysts (b) with their support. The error-bars are also shown for each point, and the calculations are shown in Appendix C.3. For the SAPO-34 supports (b) were the conversion set to 0 % as the conversion measured was negative. Reaction conditions: Temperatures 450, 400, 350, 300 and 250 °C, the feed composition 600 ppm NO, 600 ppm NH_3 and 10 % O_2, 30000 mL g_{cat}^{-1} h^{-1} and 0.1 g catalysts mixed with SiC to a reactor volume of 3 mL.

The following figures display the MS-data as a function of time during the activity testing towards NH_3-SCR for the reactant NO and the product N_2. Five temperatures were tested and for each, three areas are shown: bypass on, the SCR-reaction and cooling step. The sessions are explained in Section 3.4

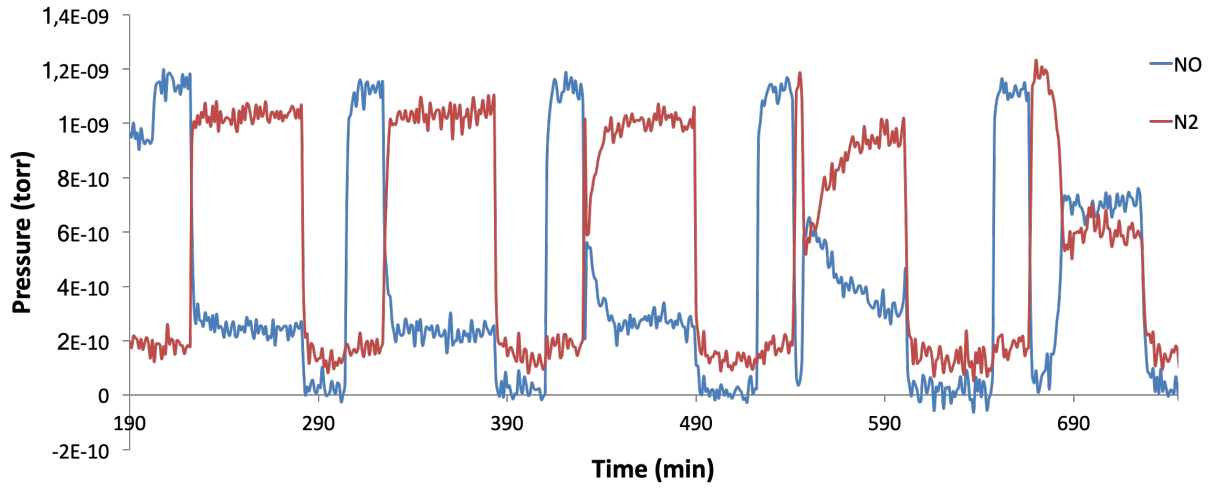

(a) FeZ.W_13.5

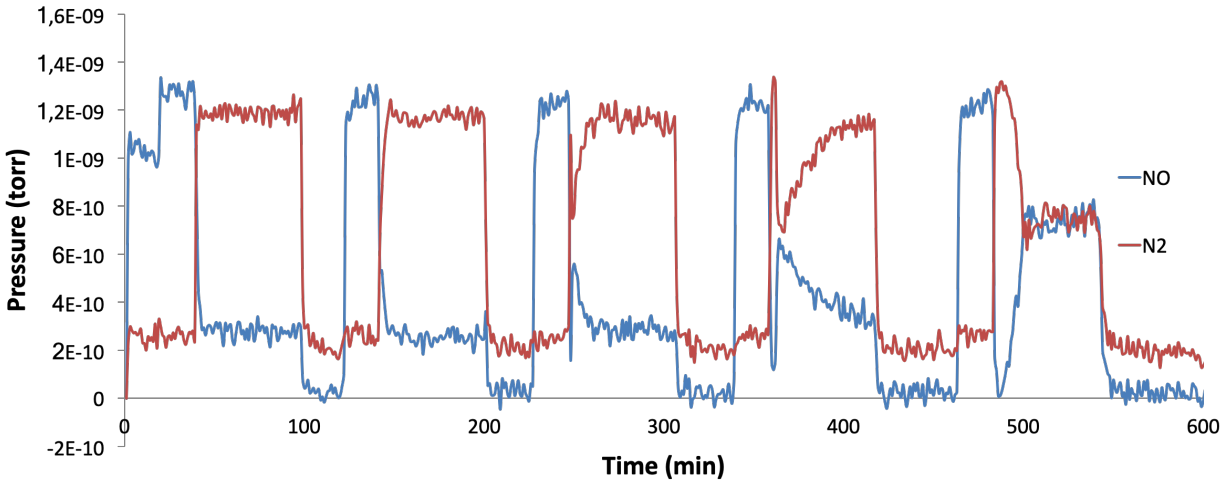

(b) FeZ.IE_13.5

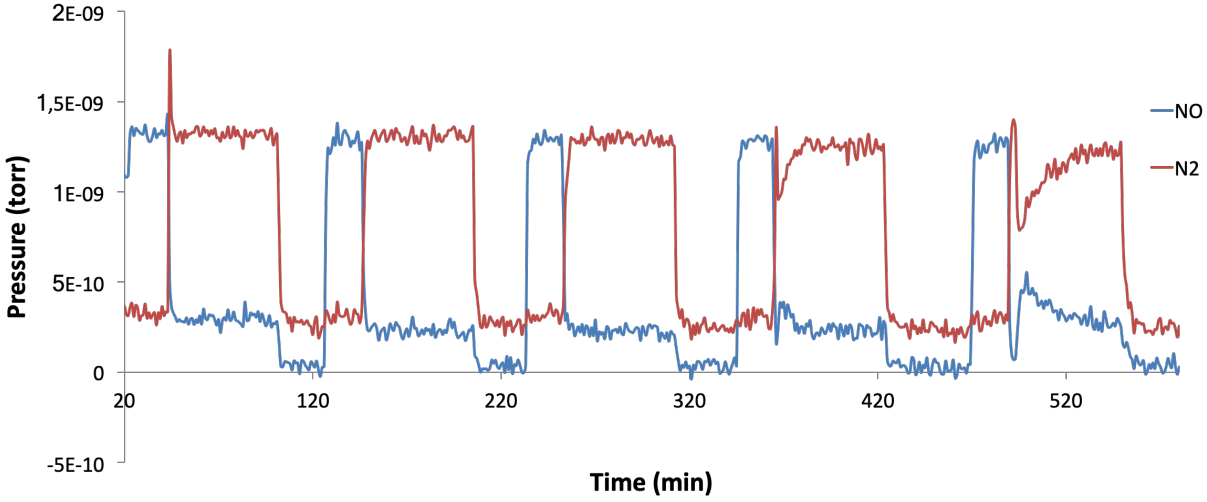

(c) FeZ.IEn_13.5.

Figure 4.13: MS-data for N_2 ($m/z = 28$ amu) and NO ($m/z = 30$ amu) during NH_3-SCR as a function of time (min) for the Fe-ZSM-5 catalysts. It was observed a peak of N_2 for FeZ.IEn_13.5 (c) after activation, probably a consequence of pressure drop when bypass is turned off. This is edited, such that the results is properly shown. Reaction conditions: Temperatures 450, 400, 350, 300 and 250 °C, the feed composition 600 ppm NO, 600 ppm NH_3 and 10 % O_2, 30000 mL g_{cat}^{-1} h^{-1} and 0.1 g catalysts mixed with SiC to a reactor volume of 3 mL.

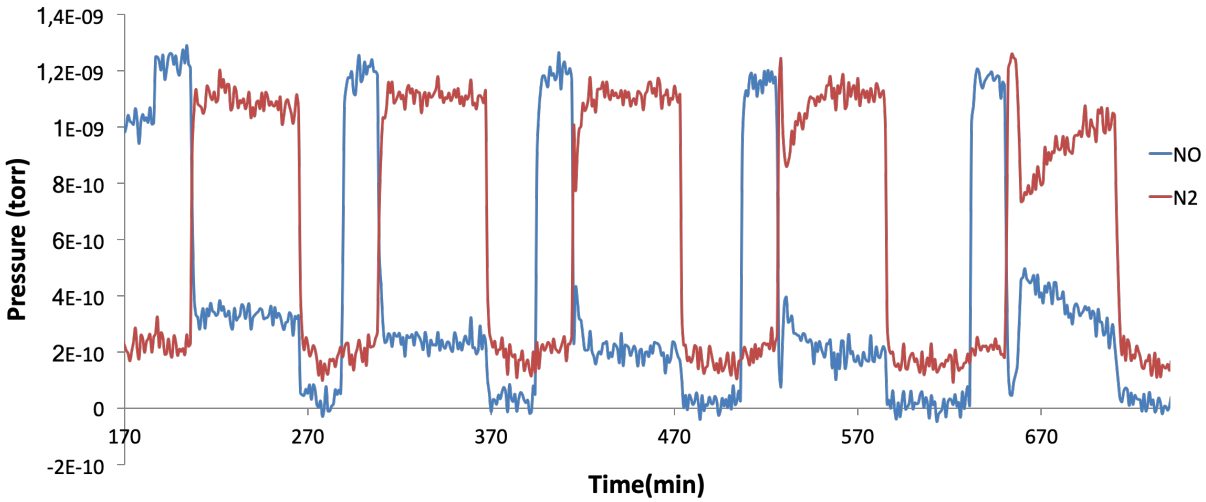

(a) FeSA.IEn_03

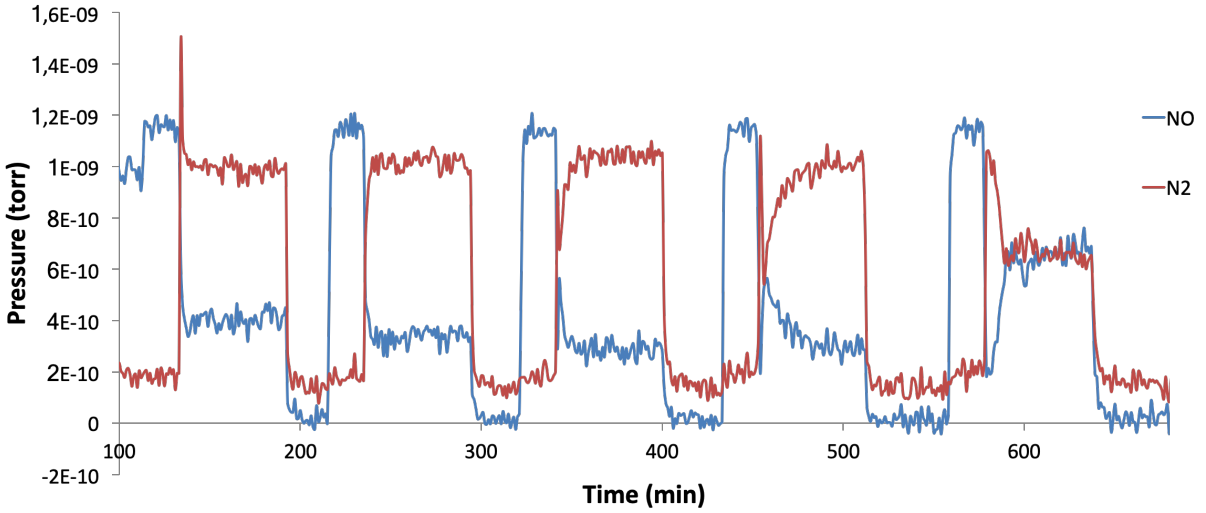

(b) hi-FeSA.IEn_03

Figure 4.14: MS-data for N_2 (m/z = 28 amu) and NO (m/z = 30 amu) during NH_3-SCR as a function of time (min) for the Fe-SAPO-34 catalysts. It was observed a peak of N_2 hi-FeSA.IEn_03 (b) after activation, probably a consequence of pressure drop when bypass is turned off. This is edited, such that the results is properly shown. Reaction conditions: Temperatures 450, 400, 350, 300 and 250 °C, the feed composition 600 ppm NO, 600 ppm NH_3 and 10 % O_2, 30000 mL g_{cat}^{-1} h^{-1} and 0.1 g catalysts mixed with SiC to a reactor volume of 3 mL.

Chapter 5

Discussion

The results presented in Chapter 4 are discussed in the following chapter. First, results from the characterization of the synthesized SAPO-34 supports are described to outline differences between the zeotypes. It is explained why the hi-SAPO-34 samples with 24 hours crystallization were not used as supports for iron catalysts. Second, the characterization results for the catalysts are discussed: XRD, N_2 physisorption, TPR, ICP-MS and chemisorption. Finally, the catalytic performance of the catalysts towards NH_3-SCR at lower temperatures are discussed.

5.1 Characterization of synthesized SAPO-34

The conventional SAPO-34 zeotypes C-SAPO_02 and C-SAPO_03, and the hierarchical SAPO-34 zeotypes with 119 hour crystallization, hi-SAPO_02:119 and hi-SAPO_03:119, were elected to be used as supports for catalysts based on the characterization results.

The conventional SAPO-34 samples appeared to be both crystalline and similar to the CHA-structure, as seen in the diffractogram in Figure 4.1. The diffraction patterns are relatively similar, however it can be observed some higher intensity for the C-SAPO_02 with a Si/Al-ratio of 0.2, compared to C-SAPO_03, indicating that this sample could be the most crystalline of the two.

The hierarchical SAPO-34 samples showed crystallinity, yet it was less intense than the C-SAPO-34 samples. Figure 4.2 shows the diffraction patterns for the hi-SAPO-34 samples. The overall intensity is much lower compared to the conventional one, which is illustrated in Figure 4.3. The reduced intensity is likely to be related to the mesopores in the hi-SAPO-34 structure, since the mesopores can interrupt the long-range order and therefore influence the intensity for the diffraction pattern.

The Si/Al-ratios, seen in Table 4.1, were close to the intended theoretical value for all samples except the C-SAPO_03 sample with a theoretical Si/Al-ratio value of 0.3, where a 50 % decrease in the value was observed. During preparation of SAPO-34 zeotypes, Si-atoms are incorporated into the P and Al structure replacing T-atoms (see Section 2.1). Since the Si/Al-ratio has decreased, this could indicate that not all the added silica was crystallized in the zeotype structure.

For this work, two preparations of hi-SAPO-34 zeotypes were preformed with different crystallization time to achieve a more crystalline sample. The characterization results from XRD, BET and SEM images of the hi-SAPO-34 samples with 24 hours crystallization, hi-SAPO_02:24 and hi-SAPO_03:24, showed that these zeotypes had a mix of phases. Therefore a new synthesis was done with 119 hours crystallization. As mentioned, diffractogram for the hi-SAPO-34 are shown in Figure 4.2. For the zeotypes with 24 hours crystallization, is the intensity weaker and the baseline slightly curved. This indicated that different phases could be present, such as amorph and crystalline phases. This was confirmed by SEM images shown in Figure B.1 (Appendix B.1). Here, the C-SAPO_02 sample has cubic formed particles, which is typical for the SAPO-34 material [22], whereas the hi-SAPO_02:24 sample has less cubic particles and several more amorphous particles. These more round particles can indicate that the hi-SAPO-34 samples with 24 hours crystallization were not phase-pure.

Further, the BET specific surface area (Table 4.2) of the hi-SAPO-34 samples with 24 hours crystallization are lower compared to the other samples. This could indicate some collapse in the pore structure for these samples. These trends are consistent with results found for the XRD diffractograms and the SEM images. The BET surface areas are highest for the conventional samples, which is to be expected as these samples mainly have micropores. For the hi-SAPO-34 samples the area is increased with increased crystallization.

It is worth mentioning that BET is not an optimal method for microporous samples. However, for an internal comparison between the samples and to locate possible change in the pore structure is still possible, and this is the main purpose of the N_2 physisorption measurements in this thesis.

Figure 4.2 shows that the new synthesized samples with 119 hours crystallization, hi-SAPO_02:119 and hi-SAPO_03:119, could have improved crystallinity. It is not observed peaks that do not occur for the CHA-structure, indicating that the samples probably have a structure similar to CHA. However the overall intensity is low, indicating that the sample may not be phase-pure.

The N_2 adsorption and desorption isotherms with the BJH-pore size distribution for the zeotypes are shown in Figures 4.4, 4.5 and 4.6. It can be seen that the hysteresis effect (Type IV isotherm) is more prominent for the hi-SAPO-34 samples, indicating that

these samples have presence of mesopores. The C-SAPO-34 samples have an isotherm with more resemblance to the Type I isotherm, confirming more microporous samples. Further, the BJH-pore size distribution for the hi-SAPO-34 samples have an intense peak in the mesopore range around 40 Å, which is not present for the C-SAPO-34 samples. In addition, the mesopore volume, V_{meso}, is much higher for the hi-SAPO-34 samples as shown in Table 4.2. These results confirm the possible presence of mesopores in the hi-SAPO-34 samples and micropores for the C-SAPO-34 samples. The small peak around 40 Å for the C-SAPO-34 samples could appear due to the TSE-effect (see Section 2.4.2), and not due to presence of mesopores. Micropores (< 20 $\AA$) were not possible to detect by the BJH-analysis.

When comparing the N_2-physisorption results (Figures 4.5 and 4.6) for the hi-SAPO-34 samples with 119 hours crystallization, hi-SAPO_02:119 and hi-SAPO_03:119, the results indicate more mesopores present for the hi-SAPO_02:119 zeotype. The hi-SAPO_03:119 sample's isotherm is in between Type IV and I, and has a much less intense peak in the BJH pore size distribution compared to the hi-SAPO_02:119. These results may indicate that hi-SAPO_02:119, which had the lower Si/Al-ratio, had more mesopores present.

5.2 Characterization of synthesized Fe-catalysts

In the following section are the characterization results of the catalysts prepared discussed. The catalysts prepared were iron supported by ZSM-5, Fe-ZSM-5, iron supported by conventional SAPO-34, Fe-C-SAPO-34, and iron supported by hierarchical SAPO-34, Fe-hi-SAPO-34.

5.2.1 X-Ray Diffraction

XRD-analysis of Fe-ZSM-5 catalysts seen in Figure 4.7a indicate that the catalysts have sustained the MFI-structure of the ZSM-5 zeolites. Further, it is not found any significant variation between the samples which could distinguish them. It is not observed peaks indicating other phases either. Iron oxides peaks are typically found around 2Θ equal to 30°, 35°, 43°and 63° [43]. Figure 4.7b displays the Fe-ZSM-5 catalysts diffractogram zoomed in for 2Θ angles between 30°and 65°, and no peaks are observed to confirm presence of iron oxide. Small particles as well as very dispersed particles are not possible to detect in XRD, as mentioned in Section B.3. The iron-loading for the samples were low, especially for the ion-exchanged samples (see Table 4.4), which could indicate that small and dispersed iron species were present.

The Fe-C-SAPO-34 catalysts show crystallinity and phases indicating the CHA-structure also after the ion-exchange, as seen in Figure 4.9. In contrast, XRD analysis of the

Fe-hi-SAPO-34 catalysts indicated that the samples have had some structural changes during the ion-exchange. The peak intensity for the catalysts (Figure 4.9) are lower when comparing to the peak intensity of the hi-SAPO-34 (119h) samples (Figure 4.2). This could indicate a structural change such as loss in the crystallinity.

In general, the diffractograms of the Fe-hi-SAPO-34 catalysts have peaks confirming that the samples display some crystallinity, and possibly have CHA phases present. However, the low intensity and lack of some peaks that the CHA structure do display, could indicate that other phases are present, for example amorphous phases. Presence of iron oxides are not confirmed for the SAPO-34 catalysts either. Only 2Θ angles below 40 ° were analyzed, so it could be that iron oxides were visible at higher angles. However, the iron loading are also low for these catalysts and could be too low for XRD-detection.

5.2.2 N_2 Physisorption

The Fe-ZSM-5 catalysts have BET surface areas (Table 4.3) in the range just below the commercial reference value of approximately 425 $m^2\,g^{-1}$ [19]. Some difference is observed, however handling micropores with BET implies uncertainty, as mentioned in Section 2.4.2. Therefore, the BET surface areas found are treated with caution. For this thesis, the BET-results were not the main focus, but rather used to indicate if the samples had maintained a relatively high surface area, which is a known property for molecular sieves, and to compare the samples internally.

The BET surface area results for the hi-FeSA.IEn_03 catalyst indicated that this catalyst had experienced some collapse in the structure upon the ion-exchange. This catalysts was the new catalyst not found reported in literature. The BET surface area of its support, hi-SAPO_03:119, was 455 $m^2\,g_{BET}^{-1}$ (Table 4.2), which was higher than the catalyst's 380 $m^2\,g_{BET}^{-1}$ (Table 4.3). Further, it was observed that the BET surface area for the hi-FeSA.IEn_03 catalyst was now closer to the BET surface area for the hi-SAPO-34 supports with 24 hours crystallization, which were 318 and 346 $m^2\,g_{BET}^{-1}$ (Table 4.3). Characterization results for these hi-SAPO-34 samples with 24 hours crystallization indicate that several phases may be present. The lower BET surface could therefore suggest that the hi-FeSA.IEn_03 catalyst's structure had become similar to these hi-SAPO-34, which were shown to be both amorph and crystalline. The iron catalysts with C-SAPO-34 as support, FeSA.IEn_02 and FeSA.IEn_03, had similar BET surface area before and after the ion exchange, as seen by comparing Table 4.2 with Table 4.3.

The pore distribution for the hi-FeSA.IEn_03 sample is shown in Figure 4.10. The adsorption and desorption isotherm and the BJH pore distribution are similar to the supports (Figure 4.6b). This could indicate presence of mesopores for these iron catalysts. However, the pore distribution has broader peaks in the mesopore range indicating that different mesopores could be present.

5.2.3 ICP-MS

The Si/Al-ratios calculated from elemental analysis by ICP-MS are compared to their theoretical values in Table 4.4. Two observations were found: First, the sample FeZ.W_30 was synthesized from NH_4-ZSM-5 with a Si/Al-ratio of 280 instead of 30 as a consequence of a mix-up with the samples (explained in Appendix A.1). Second, the intended Si/Al-ratio difference between the Fe-ZSM-5 catalysts from the synthesis were not present in the same degree. The Si/Al-ratios measured for Fe-ZSM-5 catalysts were in the range 12.9-16.1, regardless of whether it was synthesized from NH_4-ZSM-5 with a theoretical Si/Al-ratio equal 13.5 or 30. The original purchased NH_4-ZSM-5 with theoretical Si/Al-ratio equal to 30 was tested with ICP-MS, and the value was 15.6 (Table A.1), explaining why the catalysts have closer Si/Al-ratios. From these results, the catalysts FeZ.IE_13.5 and FeZ.IE_30 ended up more alike than intended, and so did FeZ.IEn_13.5 and FeZ.IEn_30.

Iron loadings were also calculated from ICP-MS analysis listed in Table 4.4. For the impregnated samples the iron loadings were much higher than the ion-exchanges catalysts. It was, however, observed a contrast in the color for these samples compared to the ion-exchanged samples (see Figure B.17 in appendix). The impregnated samples were more brown red, indicating that iron may be present as oxides particles. The catalysts ion-exchanged in an inert atmosphere with $FeCl_2$ resulted in 50 % more iron, compared to ion-exchange with $Fe(NO_3)_3$ (Table 4.4). This could be explained by the presence of Fe^{2+} instead of Fe^{3+}, which is smaller and therefore could more easily penetrate the pores of the ZSM-5 support, as mentioned in Section 2.3.1.

The accuracy of the ICP-MS analysis was partly checked: Two results from two different analyses were compared for the sample FeZ.W_30, in order to indicate the accuracy of the elemental analysis. The variation between the iron loading in the first analysis and the last was 0.05. This is then a indication of the uncertainty for the values found in ICP-MS.

5.2.4 Temperature-Programmed Reduction of H_2

TPR experiments were performed to determine the approximately reduction temperatures for further dispersion analysis by chemisorption. Four samples, FeZ.W_30, FeZ.IE_13.5, FeZ.IEn_13.5 and FeSA.IEn_03, were analyzed to cover the main groups of catalysts present: impregnated ZSM-5, ion-exchange ZSM-5 with $FeNO_3$, ion-exchange ZSM-5 inert with $FeCl_2$ and ion-exchange SAPO-34 inert with $FeCl_2$. There was observed no consumption of H_2 for the ion-exchange samples, probably because of the iron loading (Table 4.4) was too low to be registered by the detector in the TPR instrument. The Fe-catalyst supported by hi-SAPO-34 was not analyzed, however trends indicate no H_2 would be consumed for this sample since the iron loadings are lowest for these samples.

Uptake was detected for the impregnated sample shown in Figure 4.11. The impregnated samples had both a much higher Fe wt.% and a brown-red color compared to the whitish color of the ion-exchange samples (see Figure B.17 in appendix), indicating that the iron loading was high enough for TPR-detection.

The peaks from the TPR profile of the impregnated catalysts correlate to findings in literature, and suggests therefore presence of Fe^{3+}-species, iron oxides particles and Fe^{2+}. Delahay et al. [44] studied H_2-TPR profiles for Fe-ZSM-5 catalysts and found three temperature areas where peaks were detected: $240 - 480$ ℃, $480 - 680$ ℃ and above 680 ℃. In the low temperature range, reduction of Fe^{3+}-species occur. In the middle range, reduction of iron oxides particles occur over two peaks. And for the high temperature range, reduction of Fe^{2+} to Fe^0 takes place. From the TPR-analysis, it was assumed that iron present in the samples were all reduced to its metallic state for temperatures below 900 ℃.

5.2.5 Chemisorption

Chemisorption measurements were done to estimate the dispersion of iron for the catalysts. The dispersion found from chemisorption analysis and the iron leading are listed in Table 4.4. The Fe-ZSM-5 catalysts ion-exchange in inert atmosphere with $FeCl_2$ have the highest dispersion and stood out compared to the other catalysts. The catalysts FeZ.IE_13.5 and FeZ.IE_30 ion-exchanged with $Fe(NO_3)_3$ have 75 % and 50 % less dispersion respectively. Furthermore, the impregnated ZSM-5 catalysts have much lower dispersion. Last, for the SAPO-34 catalysts, all chemisorption were shown to be reversible and therefore no dispersion results were calculated.

Dispersion and elemental analysis show that the ion-exchanged catalysts display similar trends of higher dispersion along with lower iron loading, whereas opposite trends are found for the impregnated catalysts. The high iron loading along with lower dispersion for the impregnated catalysts, could indicate that the Fe atoms are not very dispersed over the surface, and rather present as iron particles such as iron oxides. Much lower iron loadings were observed for the ion-exchanged catalysts, however with much higher dispersion, indicating that a higher fraction of the iron present is available at the surface.

The chemisorption stoichiometry is assumed to have a value of 2, which is a value debated in literature [42]. The value influences the dispersion as shown in Equation 2.4.8. However, for this thesis, an internal comparison of the samples' dispersion is the focus, in contrast to comparing to others work. From that perspective, the exact value of the stoichiometry constant does not affect the internal comparison between the samples.

Furthermore, other sources of errors could impact the dispersion results. The calculations depend on the iron loading found in ICP-MS, the sample mass and the measured

chemisorbed gas, v_m, all of which contains uncertainties influencing the result.

5.3 Activity measurements

The main goal for this thesis was to investigate the catalytic activity towards NH_3-SCR at lower temperatures for the prepared catalysts. In this thesis the term catalytic performance is used to describe the ability to convert NO during NH_3-SCR. Five of the 10 catalysts synthesized were tested towards NH_3-SCR to determine the NO-conversion as a function of temperature. These catalysts were: FeZ.W_13.5, FeZ.IE_13.5 and FeZ.IEn_13.5, FeSA.IEn_03 and hi-FeSA.IEn_03. These prioritized samples are three Fe-ZSM-5 catalysts with a Si/Al=13.5, and two Fe-SAPO-34 catalysts with a Si/Al=0.3, one supported by C-SAPO-34 and one by hi-SAPO-34 synthesized with 119 hours crystallization.

The five catalysts were chosen on the basis of characterization results, and on the fact that work done in literature showed a trend of using ZSM-5 supports with a Si/Al-ratio of approximately 14 [11, 27]. Since the characterization results showed that all the catalysts were successfully synthesized, was it chosen to use the samples with the lowest ratios. However, it is worth mentioning that not all characterization results were established when the selection of samples was done, for example, dispersion and iron loading were not measured for all samples.

In retrospect, the dispersion results show that the FeZ.IE_30 had almost 50 % higher dispersion compared to FeZ.IE_13.5 (Table 4.4), which could have influenced the SCR-activity. In addition, the SCR-activity could have been improved for Fe-SAPO-34 catalysts synthesized from zeotypes with Si/Al=0.2, because of both a higher iron loading and higher BET-surface area. The Fe-ZSM-5 catalysts which were not tested were those synthesized from ZSM-5 Si/Al=30. However, as mentioned above, the Si/Al-ratio was not very different between these samples and those synthesized from ZSM-5 Si/Al=13.5, as seen in Table 4.4.

The activity measurements showed that the catalyst FeZ.IEn_13.5 had the best overall NO-conversion for all temperatures. At higher temperatures, all the catalysts show almost the same conversion. Figure 4.12 display the NO-conversion during NH_3-SCR for the catalysts and the supports. The catalyst FeZ.IEn_13.5 was supported by ZSM-5 with a Si/Al-ratio of 13.5 and prepared by inert ion-exchange with $FeCl_2$.

For the Fe-ZSM-5 catalysts, shown in Figure 4.12a, no significant difference is observed between FeZ.W_13.5 and FeZ.IE_13.5, whereas the FeZ.IEn_13.5 is standing out at lower temperatures with increased NO-conversion. For the Fe-SAPO-34 catalysts, shown in Figure 4.12b, the NO-conversion is highest for the catalyst supported by the conventional SAPO-34. Further, is it observed that the C-SAPO-34 and hi-SAPO-34 support are not

active, in contrast to the ZSM-5 support.

NO-conversion at 250 ℃, BET surface area, dispersion and preparation method for the catalysts are listed in the following Table 5.1 to highlight the correlation between NO-conversion at lower temperatures and other important properties.

Table 5.1: Correlation between low temperature (250 ℃) NO-conversion (X_{NO}), surface area, dispersion, preparation method and iron loading for the precursor for Fe-catalysts. The catalyst are listed in decreasing order of X_{NO} at 250 ℃. The results are collected from the tables 4.4 (ICP-MS), 4.3 (N_2 physisorption), and the synthesis method and precursor are listed in Table 3.2.

Sample	**X_{NO}, 250 ℃** (%)	Dispersion (%, diff.)	A_S ($m^2\,g_{BET}^{-1}$)	Synthesis method	Precursor
FeZ.IEn_13.5	**78**	38	352	I.E. (inert)	Fe^{2+}
FeSA.IEn_03	**71**	NA	464	I.E. (inert)	Fe^{2+}
hi-FeSA.IEn_03	**43**	3	380	I.E. (inert)	Fe^{2+}
FeZ.IE_13.5	**40**	10	364	I.E.	Fe^{3+}
FeZ.W_13.5	**38**	8	393	I.W.I.	Fe^{3+}

Consistent with the literature, the highest NO-conversion at lower temperatures were found for catalysts synthesized from ion-exchange in an inert atmosphere with $FeCl_2$ as precursor, FeZ.IEn_13.5 and FeSA.IEn_03. A relationship between this synthesis method and more presence of monomeric iron as active sites has been reported in the literature (see Section 2.2.1) [26]. Furthermore, presence of monomeric iron is suggested to be the active sites at temperatures below 300 ℃ (see Table 2.1). This suggest that the catalysts synthesized from this ion-exchange could have iron present as monomeric iron, and as a result have higher NO-conversion at temperatures below 300 ℃.

The increased activity for these catalysts could also be explained by the ion-exchange with Fe^{2+} which more easily can penetrate the small pores in the supports (see Section 2.3.1) [26]. Furthermore, a decrease in activity is observed from FeZ.IEn_13.5 to FeSA.IE.3. This could also be a consequence of the pore size: The ZSM-5 support has a theoretical larger pore diameter than the C-SAPO-34 support [12].

The decreased catalytic conversion at lower temperatures for the catalysts either synthesized by ion-exchange in air or by incipient wetness impregnation with $Fe(NO_3)_3$ as precursor, could be explained by presence of dimeric or larger iron clusters as active sites. The literature has suggests that dimeric iron and larger iron clusters contribute more to the activity at temperatures above 300 ℃ (see Table 2.1) [26]. This could indicate that these catalysts have more contribution of these iron species, and may be the reason for the lower activity.

The catalyst hi-FeSA.IEn_03 supported by a hierarchical SAPO-34 zeotype was a new catalyst not found reported on in the literature. This catalyst showed some activity towards NH_3-SCR (Figure 4.12), but lower conversion compared to the catalysts with best

performance in this thesis. It was suggested that the mesopores for the hi-SAPO-34 support could make the molecular transport more easy, and therefore increase the catalytic performance. The results show, however, that the catalysts supported by conventional SAPO-34 or ZSM-5, both being microporous supports, show higher NO-conversion.

However, it cannot be concluded how the mesoporous supports could influence the catalytic performance, due to the fact that the hi-FeSA.IEn_03 catalyst may not have been successfully prepared. As mentioned, characterization results indicate that the support structure for this catalyst could have been changed after the ion-exchange. This means that other phases can be present, such as amorphous phases, and that the sample therefore may not be phase-pure.

It is observed a correlation between NO converted and N_2 produced after SCR, indicating selectivity towards N_2. Figure 4.13 shows the MS-data for N_2 and NO after activity measurements. During the NH_3-SCR testing, it is a trend of the amount NO converted is approximately equal to the N_2 produced. These results indicate that N_2 is the main product, most likely resulting from the NH_3-SCR process.

Several different aspects could have influenced the results found in this thesis. A reference test run with SiC indicated no significant contribution of gas phase reaction influencing NO-conversion (See Figure B.16 in appendix). Further, this thesis covers only a primitive catalytic study towards NH_3-SCR, where aspects such as reaction mechanism, reaction rate or specific activity are not considered. The equilibrium conversion is not checked either, but it is used low concentrations, so the conversion should not be limited by the equilibrium conversion. In addition, the activity measurements were tested in absence of water. Presence of water may have a significant influence on the catalytic performance shown in literature [11].

Chapter 6

Conclusion

Iron-based catalysts supported by ZSM-5, conventional SAPO-34 and hierarchical SAPO-34 have been prepared by different preparation routes to test the catalytic performance towards NH_3-SCR at lower temperatures. The catalysts supported by hierarchical SAPO-34, a mesoporous zeotype, was a new catalyst not found reported in literature.

In addition, the supports C-SAPO-34 and hi-SAPO-34 have been produced successfully by hydrothermal synthesis. The hi-SAPO-34 zeotypes showed increased crystallinity when prepared with a longer crystallization time. N_2 physisorption results indicate that the C-SAPO-34 zeotypes were microporous and that the hi-SAPO-34 zeotypes had both micro- and mesopores.

The characterization results indicate that the Fe-ZSM-5 and Fe-C-ZSM-5 catalysts were successfully prepared. However, the catalysts supported by the hierarchical SAPO-34 may not maintained the same pore structure after the introducing of iron. This catalyst showed a reduced BET surface area after the ion-exchange which could indicate some collapse in the mesoporous structure.

The catalyst with highest NO-conversion towards NH_3-SCR at lower temperatures was a Fe-ZSM-5 catalyst ion-exchanged in an inert environment with $FeCl_2$, FeZ.IEn_13.5. In addition, the catalyst supported by conventional SAPO-34 with the same preparation route showed also a high NO-conversion, just below the FeZ.IEn_13.5 sample. The new catalyst supported by the mesoporous hierarchical SAPO-34, showed some activity towards NH_3-SCR. However, due to possible change in the pore structure after ion-exchange, it can not be concluded how the mesopores in this support influences the catalytic performance. Based on the results from the activity measurements, is it suggested that catalysts prepared by ion-exchange in an inert environment with an Fe^{2+}-precursor give an increased NO-conversion at lower temperatures. These catalysts had higher conversion compared to the other catalysts prepared by either incipient wetness impregnation or ion-exchange with an Fe^{3+}-precursor. To ion-exchange in an inert environment could

prohibit oxidation of Fe^{2+} which enables these smaller Fe-ions to penetrate the micropores of the support. Further, literature has suggested that this could result in more monomeric iron as the active sites, which are iron species shown to be more active at lower temperatures for NH_3-SCR [26]. Therefore, the activity results for the catalysts in this work follow the same trend as proposed in literature.

Chapter 7

Further Work

This thesis has only covered a simple screening of the catalytic performance towards NH_3-SCR at lower temperatures. Further work after this thesis could be to investigate the catalysts which showed improved NO-conversion at lower temperatures: The ion-exchanged ZSM-5 and C-SAPO-34 in an inert environment with $FeCl_2$ as precursor.

Possible aspects to investigate are which iron species that are present as the active sites. It can be checked if monomeric iron are present, which is suggested from literature to be the more active species at lower temperatures. Further, test the catalytic activity in presence of water. Water could influence the activity and stability for the catalysts, and especially influence the stability for the zeolites and zeotypes since they are typically sensitive for hydrothermal deactivation. In addition, measurements of the selectivity towards N_2, specific activity and the kinetic should be analyzed to get more understanding of the overall performance towards NH_3-SCR at lower temperatures.

It is also worth mentioning that a new catalysts, a Fe-hi-SAPO-34, was tried prepared. However, results indicate some collapse in the structure after the ion-exchange. Further work could therefore be to introduce the metal by a different method, for example coprecipitation.

Bibliography

[1] Shalini Arora and R Prasad. An overview on dry reforming of methane: strategies to reduce carbonaceous deactivation of catalysts. *RSC Advances*, 6(110):108668–108688, 2016.

[2] RK Srivastava, W Neuffer, D Grano, S Khan, JE Staudt, and W Jozewicz. Controlling nox emission from industrial sources. *Environmental progress*, 24(2):181–197, 2005.

[3] Sjøfartsdirektoratet / Norwegian Maritime Authority. Utslipp til luft; nox - nitrogenholdige oksider. https://www.sdir.no/sjofart/fartoy/miljo/forebygging-av-forurensning-fra-skip/utslipp-til-luft. Accessed: 2018-12-28.

[4] Ib. Chorkendorff and Johannes W. Niemantsverdriet. *Concepts of modern catalysis and kinetics*. John Wiley-VCH, 3 edition, 2013. :421-444.

[5] Soran Shwan. *Metal-exchanged zeolites for NH3-SCR applications-Activity and Deactivation studies*. Chalmers University of Technology, 2014. :11.

[6] Gerhard Ertl, Helmut Knözinger, Jens Weitkamp, et al. *Handbook of heterogeneous catalysis*, volume 1. Wiley-VCH, 2 edition, 2008. :Chapter 3, 13.18, 5.5 and 13.14.

[7] Stavros A Skarlis, David Berthout, André Nicolle, Christophe Dujardin, and Pascal Granger. Modeling nh3 storage over fe-and cu-zeolite based, urea-scr catalysts for mobile diesel engines. *Procedia-Social and Behavioral Sciences*, 48:1672–1682, 2012.

[8] Isabella Nova and Enrico Tronconi. *Urea-SCR technology for deNOx after treatment of diesel exhausts*. Springer, 2014.

[9] YARA. Nox reduction with scr technology. https://yaramarine.com/nox-cleaning-technology/. Accessed: 2018-12-31.

[10] Andreas Åberg. *Modelling and Operation of Diesel Engine Exhaust Gas Cleaning Systems*. PhD thesis, Danmarks Tekniske Universitet (DTU), 2017.

[11] Alexander Shishkin, Per-Anders Carlsson, Hanna Härelind, and Magnus Skoglundh.

Effect of preparation procedure on the catalytic properties of fe-zsm-5 as scr catalyst. *Topics in catalysis*, 56(9-10):567–575, 2013.

[12] Stanislava Andonova, Stefanie Tamm, Clifford Montreuil, Christine Lambert, and Louise Olsson. The effect of iron loading and hydrothermal aging on one-pot synthesized fe/sapo-34 for ammonia scr. *Applied Catalysis B: Environmental*, 180:775–787, 2016.

[13] Dong Zhang and Ralph T Yang. N2o formation pathways over zeolite-supported cu and fe catalysts in nh3-scr. *Energy & Fuels*, 32(2):2170–2182, 2018.

[14] Krijn P de Jong. *Synthesis of solid catalysts*. John Wiley & Sons, 2009.

[15] IZA Structure Commission. Database of zeolite structures: Mfi; cha. http://europe.iza-structure.org. Accessed: 2018-12-30.

[16] Sandro Brandenberger, Oliver Kröcher, Alexander Wokaun, Arno Tissler, and Roderik Althoff. The role of brønsted acidity in the selective catalytic reduction of no with ammonia over fe-zsm-5. *Journal of Catalysis*, 268(2):297–306, 2009.

[17] Gongshin Qi and Ralph T Yang. Selective catalytic oxidation (sco) of ammonia to nitrogen over fe/zsm-5 catalysts. *Applied Catalysis A: General*, 287(1):25–33, 2005.

[18] Brent M Lok, Celeste A Messina, R Lyle Patton, Richard T Gajek, Thomas R Cannan, and Edith M Flanigen. Silicoaluminophosphate molecular sieves: another new class of microporous crystalline inorganic solids. *Journal of the American Chemical Society*, 106(20):6092–6093, 1984.

[19] Zeolyst International. Zsm-5. https://www.zeolyst.com/our-products/standard-zeolite-powders/zsm-5.html. Accessed: 2019-01-06.

[20] ASC material. Zsm-5 series zeolite powder. https://www.acsmaterial.com/zsm-5-series-zeolite-powder-2387.html. Accessed: 2019-01-06.

[21] Koichi Momma and Fujio Izumi. Vesta 3 for three-dimensional visualization of crystal, volumetric and morphology data. *Journal of applied crystallography*, 44(6):1272–1276, 2011.

[22] ASC material. Technical data sheet (tds) acs material sapo-34. https://www.acsmaterial.com/sapo-1198.html. Accessed: 2019-01-06.

[23] Ivana Miletto, Chiara Ivaldi, Geo Paul, Stephanie Chapman, Leonardo Marchese, Robert Raja, and Enrica Gianotti. Hierarchical sapo-34 architectures with tailored acid sites using sustainable sugar templates. *ChemistryOpen*, 7(4):297–301, 2018.

[24] Sandro Brandenberger, Oliver Kröcher, Arno Tissler, and Roderik Althoff. The state

of the art in selective catalytic reduction of nox by ammonia using metal-exchanged zeolite catalysts. *Catalysis Reviews*, 50(4):492–531, 2008.

[25] Xiaoyan Shi, Fudong Liu, Lijuan Xie, Wenpo Shan, and Hong He. Nh3-scr performance of fresh and hydrothermally aged fe-zsm-5 in standard and fast selective catalytic reduction reactions. *Environmental science & technology*, 47(7):3293–3298, 2013.

[26] Ting Jiang and Raul F Lobo. *On the Mechanism of Ammonia SCR over Cu-and Fe-Containing Zeolite Catalysts*. Springer, 2018.

[27] Sandro Brandenberger, Oliver Kröcher, Arno Tissler, and Roderik Althoff. The determination of the activities of different iron species in fe-zsm-5 for scr of no by nh3. *Applied Catalysis B: Environmental*, 95(3-4):348–357, 2010.

[28] Soran Shwan, Jonas Jansson, Louise Olsson, and Magnus Skoglundh. Deactivation mechanisms of iron-exchanged zeolites for nh3-scr applications. *Catalysis Today*, 258:432–440, 2015.

[29] Mukundan Devadas, Oliver Kröcher, Martin Elsener, Alexander Wokaun, George Mitrikas, Nicola Söger, Marcus Pfeifer, Yvonne Demel, and Lothar Mussmann. Characterization and catalytic investigation of fe-zsm5 for urea-scr. *Catalysis Today*, 119(1-4):137–144, 2007.

[30] H. Scott Fogler. *Elements of Chemical Reaction Engineering*. Pearson, 4 edition, 2014. :Chapter 11,12.

[31] Jacob Kielland. Individual activity coefficients of ions in aqueous solutions. *Journal of the American Chemical Society*, 59(9):1675–1678, 1937.

[32] Shuangshuang Lai, Yong She, Wangcheng Zhan, Yun Guo, Yanglong Guo, Li Wang, and Guanzhong Lu. Performance of fe-zsm-5 for selective catalytic reduction of nox with nh3: Effect of the atmosphere during the preparation of catalysts. *Journal of molecular catalysis a: chemical*, 424:232–240, 2016.

[33] Minhong Xu, Jun Wang, Tie Yu, Jianqiang Wang, and Meiqing Shen. New insight into cu/sapo-34 preparation procedure: Impact of nh4-sapo-34 on the structure and cu distribution in cu-sapo-34 nh3-scr catalysts. *Applied Catalysis B: Environmental*, 220:161–170, 2018.

[34] Zhen Ma and Francisco Zaera. *Surface and Nanomolecular Catalysis*, chapter Characterization of Heterogeneous Catalysts, pages 1–37. Taylor and Francis (CRC Press), 2006.

[35] Francisco Tiago Leitao Muniz, Marcus Aurélio Ribeiro Miranda, Cássio Morilla dos

Santos, and José Marcos Sasaki. The scherrer equation and the dynamical theory of x-ray diffraction. *Acta Crystallographica Section A: Foundations and Advances*, 72(3):385–390, 2016.

[36] Stephen Brunauer, Paul Hugh Emmett, and Edward Teller. Adsorption of gases in multimolecular layers. *Journal of the American chemical society*, 60(2):309–319, 1938.

[37] Krista S Walton and Randall Q Snurr. Applicability of the bet method for determining surface areas of microporous metal- organic frameworks. *Journal of the American Chemical Society*, 129(27):8552–8556, 2007.

[38] J Rouquerol, D Avnir, CW Fairbridge, DH Everett, JM Haynes, N Pernicone, JDF Ramsay, KSW Sing, and KK Unger. Recommendations for the characterization of porous solids (technical report). *Pure and Applied Chemistry*, 66(8):1739–1758, 1994.

[39] Johan C Groen, Louk AA Peffer, and Javier Perez Ramires. Pore size determination in modified micro-and mesoporous materials. pitfalls and limitations in gas adsorption data analysis. *Microporous and mesoporous materials*, 60(1-3):1–17, 2003.

[40] Nicholas W Hurst, Stephen J Gentry, Alan Jones, and Brian D McNicol. Temperature programmed reduction. *Catalysis Reviews Science and Engineering*, 24(2):233–309, 1982.

[41] Israel Wachs. *Characterization of catalytic materials*. Momentum Press, 1993.

[42] M Boudart, A Delbouille, JA Dumesic, S Khammouma, and H Topsøe. Surface, catalytic and magnetic properties of small iron particles: I. preparation and characterization of samples. *Journal of Catalysis*, 37(3):486–502, 1975.

[43] Carlos Pecharroman, T Gonzalez-Carreno, and Juan E Iglesias. The infrared dielectric properties of maghemite, γ-fe 2 o 3, from reflectance measurement on pressed powders. *Physics and Chemistry of Minerals*, 22(1):21–29, 1995.

[44] Gérard Delahay, David Valade, Ariel Guzman-Vargas, and Bernard Coq. Selective catalytic reduction of nitric oxide with ammonia on fe-zsm-5 catalysts prepared by different methods. *Applied Catalysis B: Environmental*, 55(2):149–155, 2005.

[45] Raymond Chang et al. *General chemistry: the essential concepts*. Boston: McGraw-Hill,, 7th ed., international ed. edition, 2008.

Appendix A

Additional Information

A.1 Si/Al-ratios mix-up for impregnated ZSM-5 samples

During synthesis of Fe-ZSM-5 catalysts the labeling of the impregnated Fe-ZSM-5 Si/Al=30 was mixed with the impregnated Fe-ZSM-5 Si/Al=280. It was also impregnated H-ZSM-5 zeolites with a Si/Al-ratio of 280. After locating the possible mix-up, a ICP-MS analysis was done to check.

The results showed that the sample labeled with Si/Al=30 actually was the zeolite with a theretical Si/Al=280. The results are shown in Table A.1, and they show that the Si/Al-ratio for FeZ.W_30 is 146.5, which does not match the Si/Al-ratio of the support (=15.6). However, the Si/Al-ratio for the catalysts Fe-ZSM-W_280 match (=15.1).

Table A.1: ICP-MS results, Si/Al-ratios, for the impregnated ZSM-5 catalysts FeZ.W_30 compared to the H-ZSM-5 zeolite with a theoretical Si/Al-ratio of 30. In addition are results for a impregnated Fe-ZSM catalysts supported by a ZSM-5 with a theoretical Si/Al=280 shown.

Fe-catalyst	Si/Al (theo.)	Si/Al
H-ZSM-5	30	15.6
FeZ.W_30	30	146.5
Fe-ZSM-W_280	280	15.1

As a consequence, the characterization was not done for the indicated sample, Si/Al=30, but for the sample with a Si/Al=280. This was only the case for the impregnated samples.

Appendix B

Additional results

B.1 SEM images of zeotypes

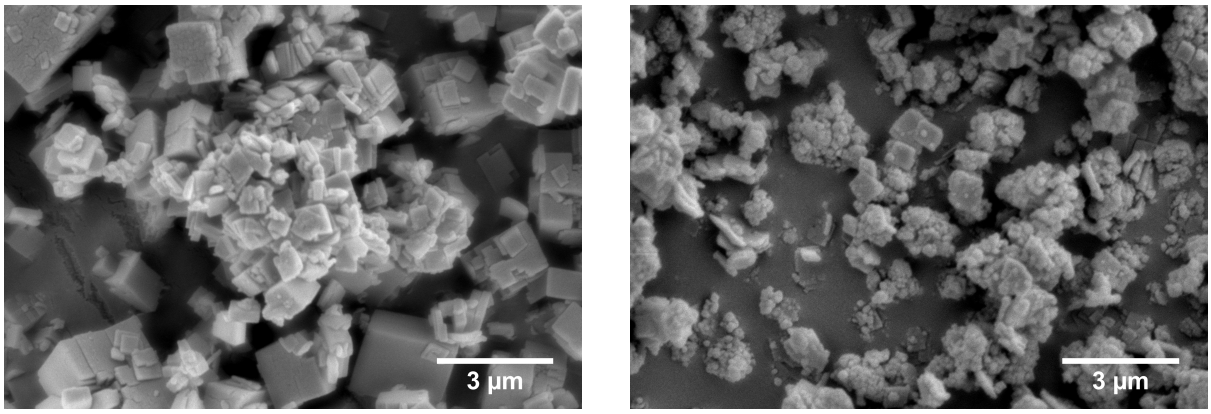

(a) C-SAPO_02 **(b)** Hi-SAPO_02:24

Figure B.1: SEM images showing the morphology and size of C-SAPO02 and Hi-SAPO02:24 particles, taken by Daniel Ali (IKJ, NTNU) with a Hitachi S-3400N Instrument. An Edwards Sputter Coater S150B was used to coat both samples with gold for 2 minutes each at a pressure of 0.15 atm. The ampere and voltage under the sputtering were 20 mAand 2.0 kV respectively. The SEM images were taken at a magnification of 8500X with an acceleration voltage of 10.0kV.

B.2 Element results from ICP-MS

Table B.1: Element results, wt.%, for all samples analyzed by ICP-MS.

Sample	wt.% Fe	wt.% Al	wt.% Si	wt.% P
C-SAPO_02	0.0	22.5	4.8	17.2
C-SAPO_03	0.0	22.5	3.9	17.9
hi-SAPO_02:24	NA	NA	NA	NA
hi-SAPO_03:24	NA	NA	NA	NA
hi-SAPO_02:119	0.0	22.0	5.9	17.3
hi-SAPO_03:119	0.0	23.7	8.6	18.6
FeZ.W_13.5	5.2	3.0	40.7	NA
FeZ.W_30	4.7	0.3	44.8	NA
FeZ.IE_13.5	0.5	3.0	42.3	NA
FeZ.IE_30	0.4	2.4	39.7	NA
FeZ.IEn_13.5	1.1	3.2	43.8	NA
FeZ.IEn_30	0.9	2.9	46.3	NA
FeSA.IEn_02	0.8	22.8	4.8	18.0
FeSA.IEn_03	0.6	22.9	3.9	18.6
hi-FeSA.IEn_02	0.6	23.5	4.9	18.0
hi-FeSA.IEn_03	0.4	17.6	5.8	13.5

B.3 XRD Diffractogram

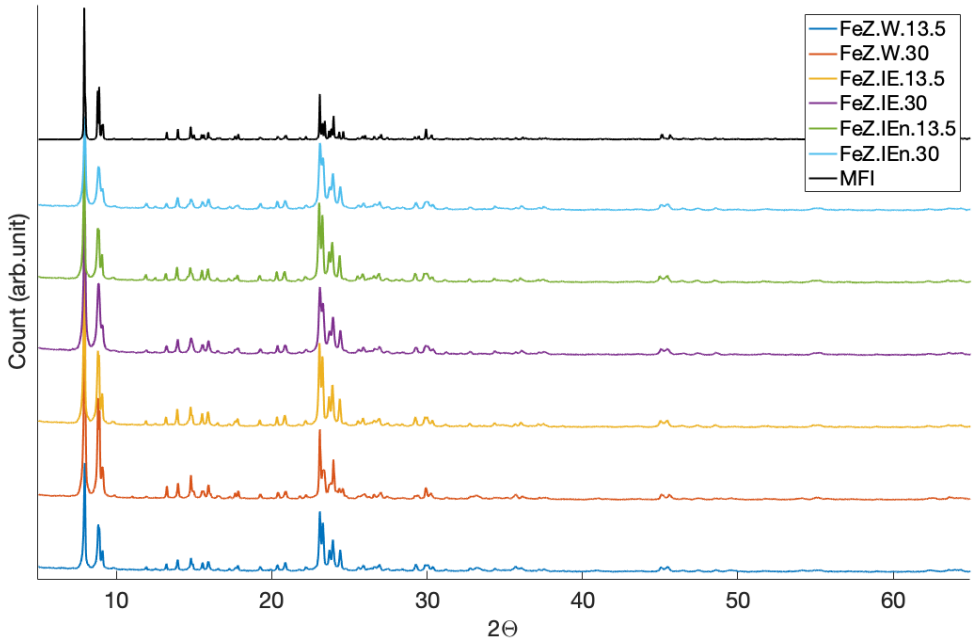

Figure B.2: Complete diffractogram plotted for the MFI-structure and Fe-ZSM-5 catalysts synthesized: FeZ.W.13.5, FeZ.W.30, FeZ.IE.13.5, FeZ.IE.30, FeZ.IEn.13.5, FeZ.IEn.30. The plot has arbitrary units at the vertical axis. Structure data for the MFI-structure is collected from IZA Synthesis Commission [15].

B.4 Chemisorption

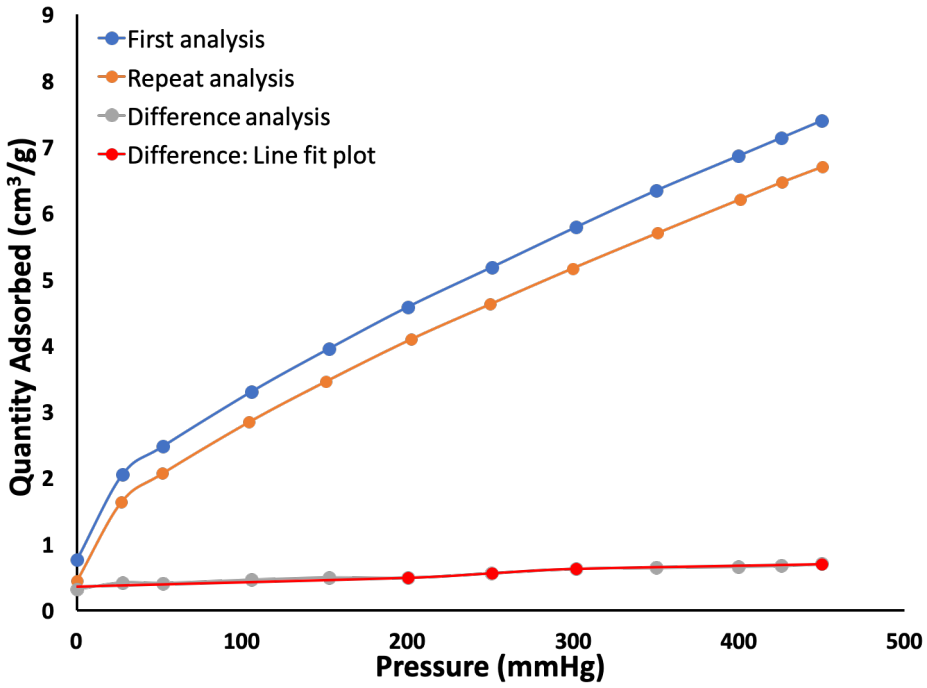

Figure B.3: Isotherms from CO chemisorption for FeZ.W_13.5: First (upper), repeated (lower) and the difference isotherm (analysis) are shown, in addition is the back-extrapolation to zero pressure shown. The red points are the selected points for the linear fit.

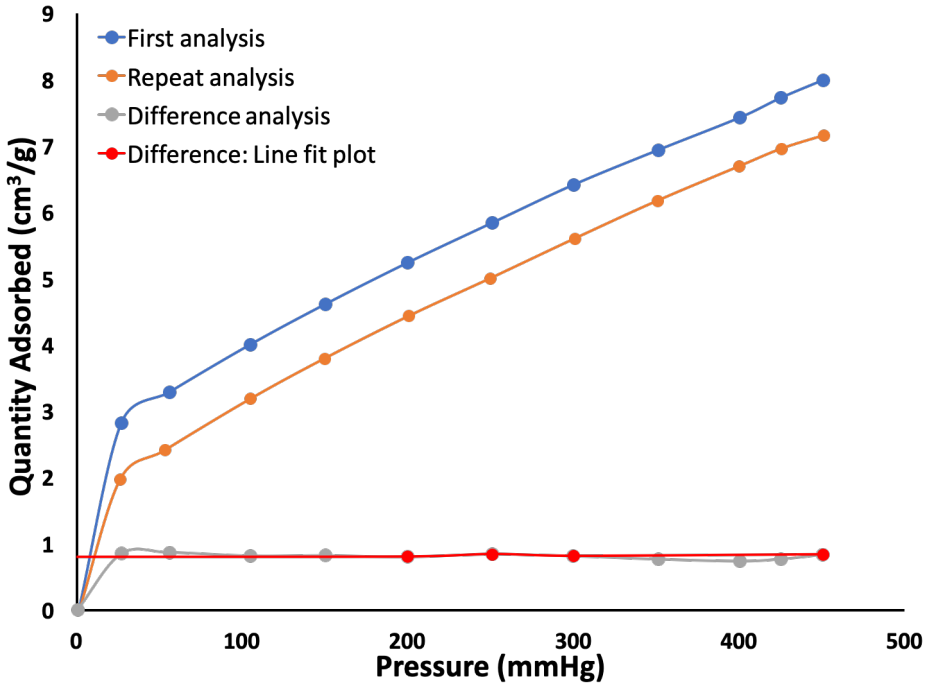

Figure B.4: Isotherms from CO chemisorption for FeZ.IEn_13.5: First (upper), repeated (lower) and the difference isotherm (analysis) are shown, in addition is the back-extrapolation to zero pressure shown. The red points are the selected points for the linear fit.

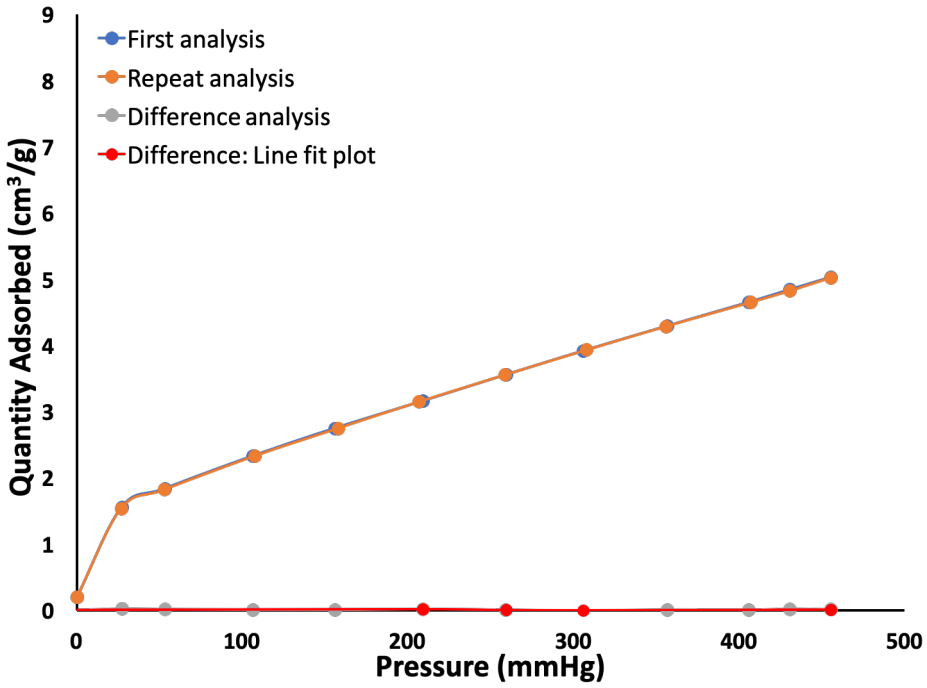

Figure B.5: Isotherms from CO chemisorption for FeSA.IEn_03: First (upper), repeated (lower) and the difference isotherm (analysis) are shown, in addition is the back-extrapolation to zero pressure shown. The red points are the selected points for the linear fit.

B.5 N_2 adsorption and desorption isotherms

Following are the adsorption and desorption isotherms from N_2-physisorption plotted. The labels shown in the figures are the previously labels, however the new labels are listed in the figure text.

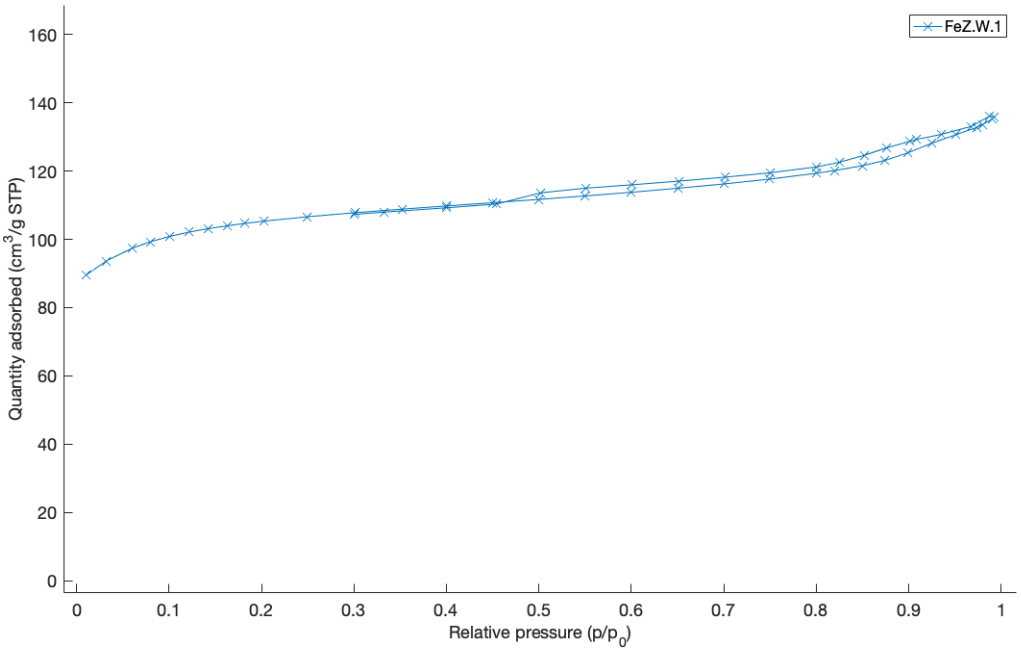

Figure B.6: N_2 adsorption and desorption isotherm for FeZ.W_13.5

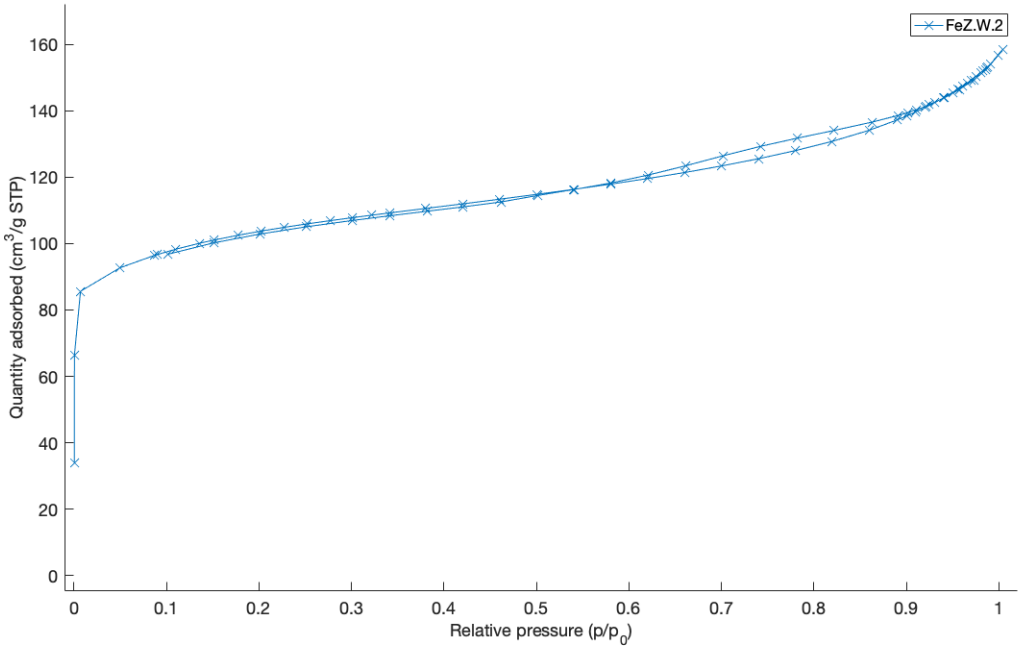

Figure B.7: N_2 adsorption and desorption isotherm for FeZ.W_30

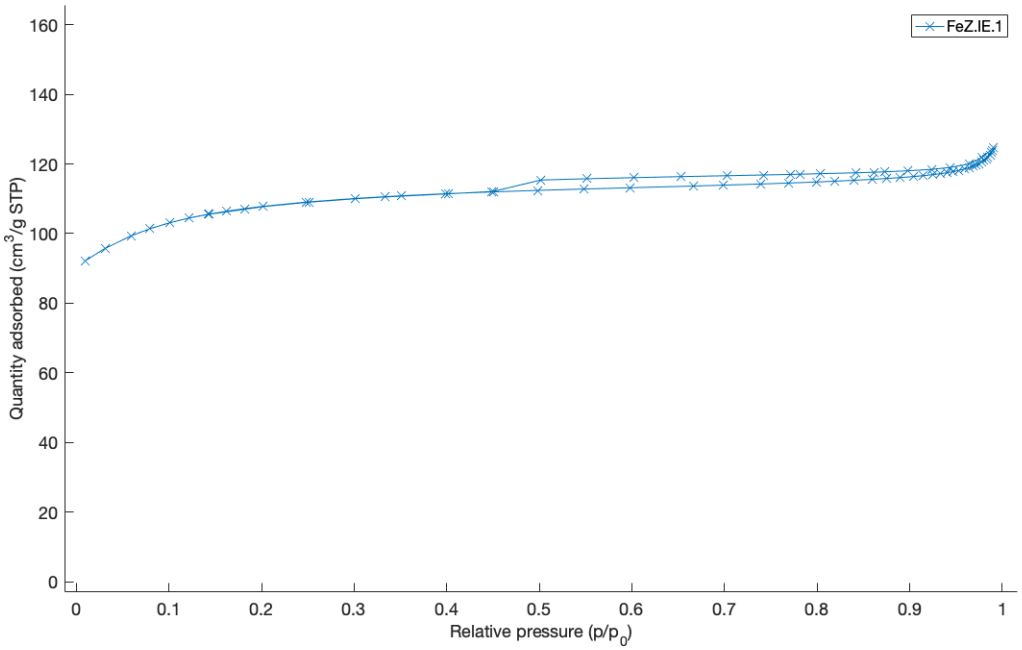

Figure B.8: N_2 adsorption and desorption isotherm for FeZ.IE_13.5

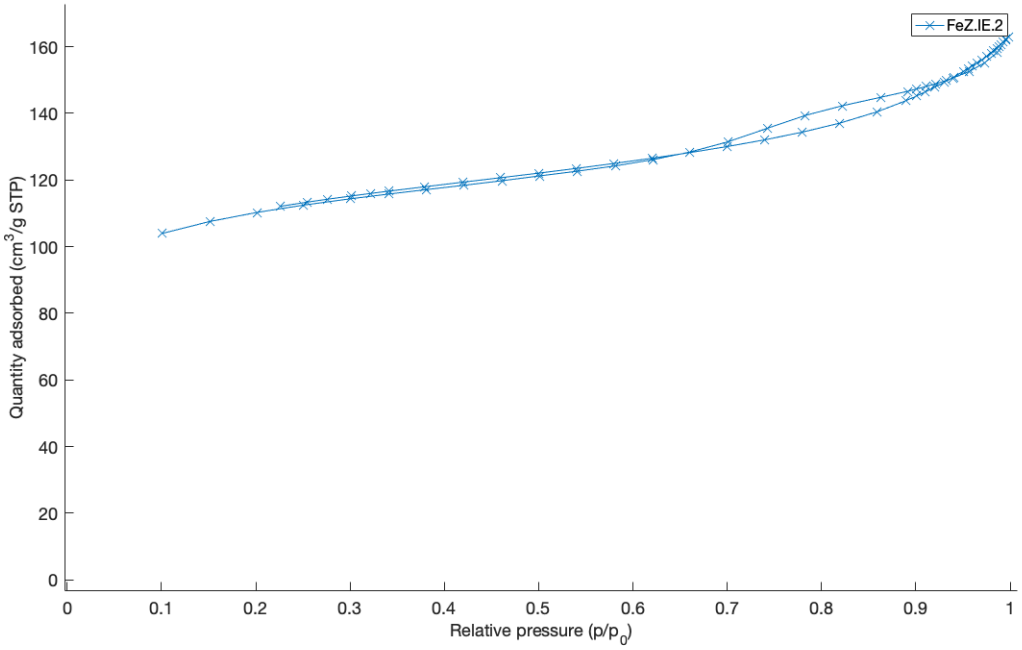

Figure B.9: N_2 adsorption and desorption isotherm for FeZ.IE_30

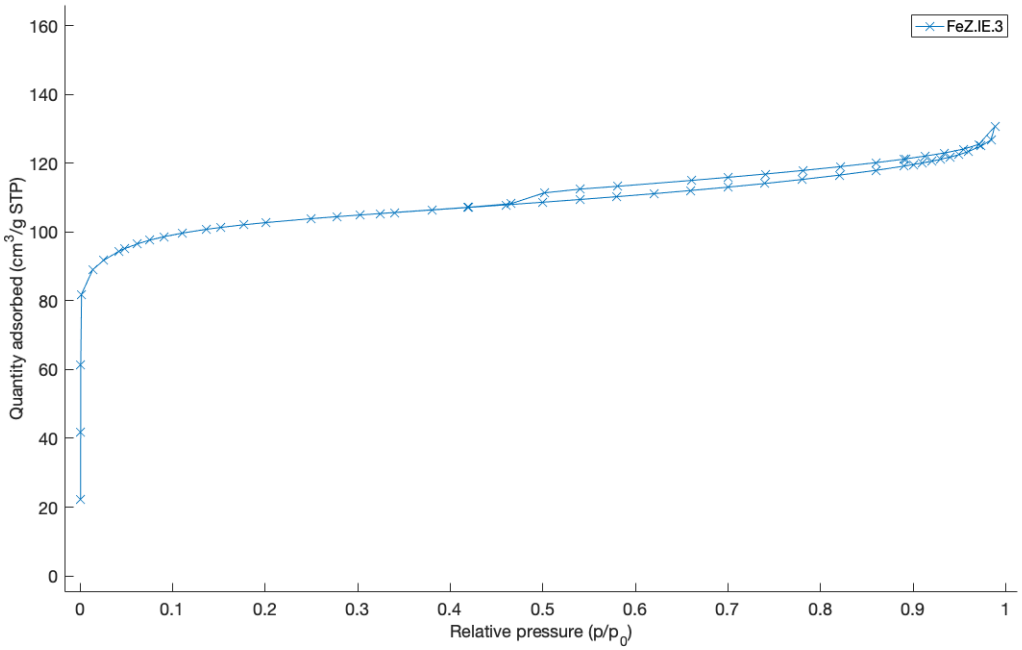

Figure B.10: N_2 adsorption and desorption isotherm for FeZ.IEn_13.5

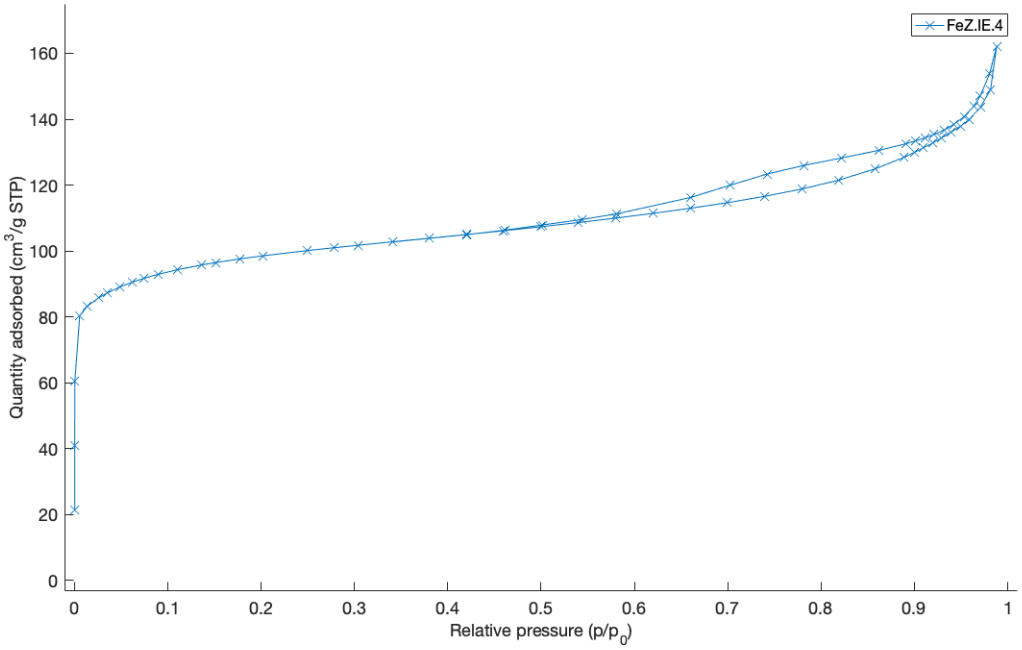

Figure B.11: N_2 adsorption and desorption isotherm for FeZ.IEn_30

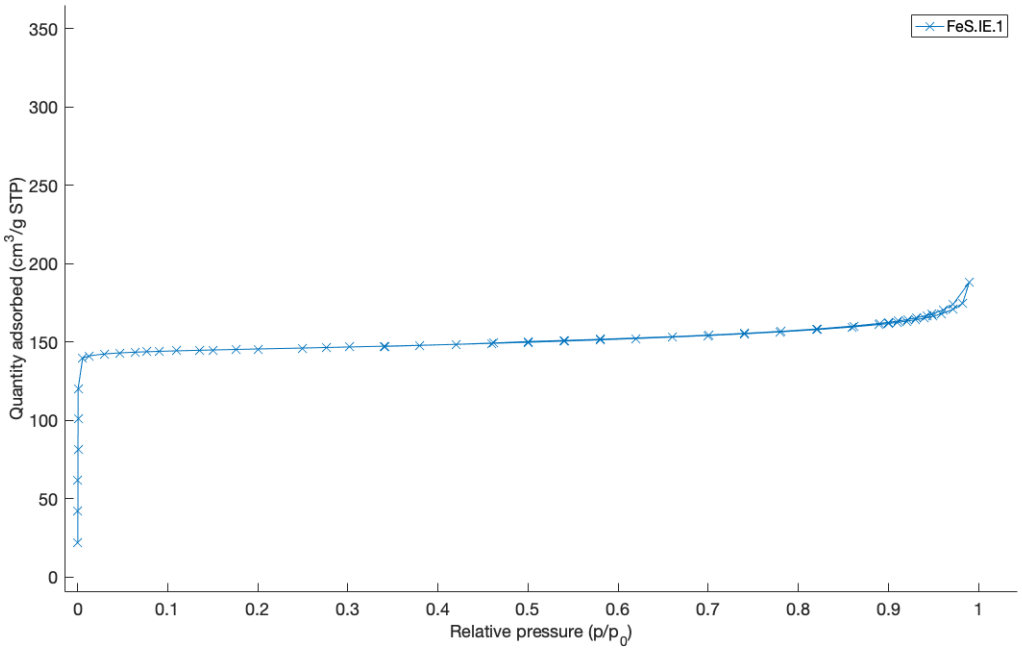

Figure B.12: N_2 adsorption and desorption isotherm for FeSA.IEn_02

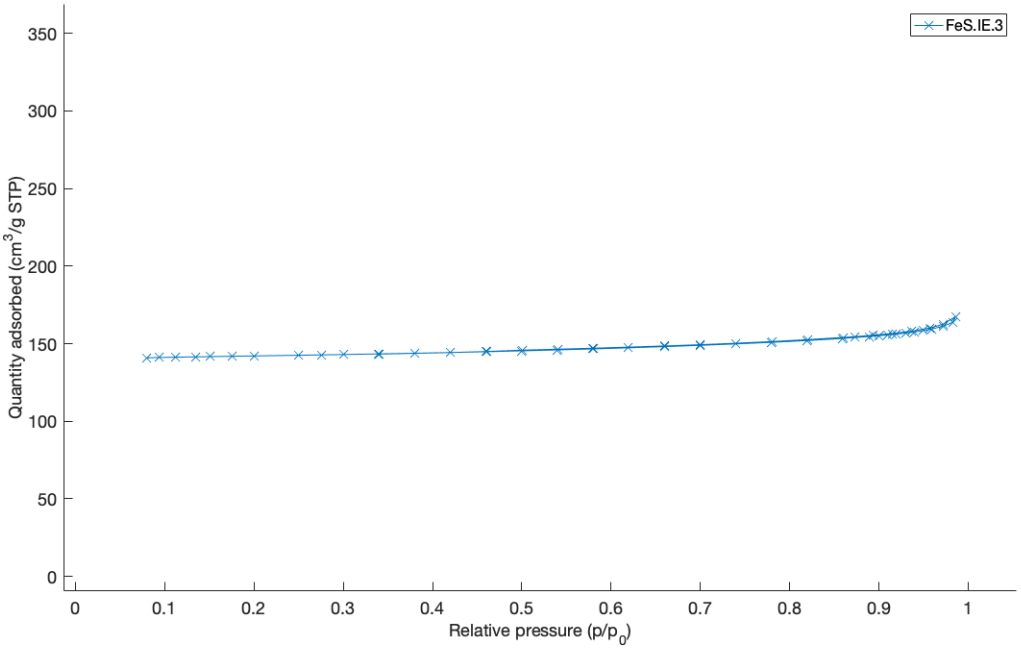

Figure B.13: N_2 adsorption and desorption isotherm for FeSA.IEn_03

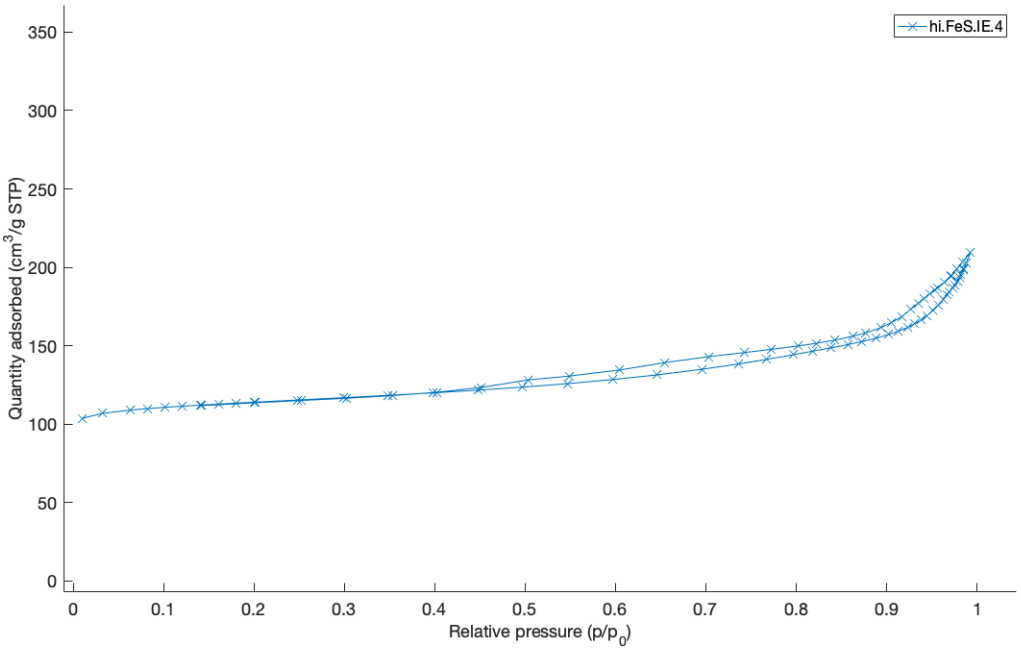

Figure B.14: N_2 adsorption and desorption isotherm for hi-FeSA.IEn_03

B.6 MS-data for NO and N_2: Supports and SiC

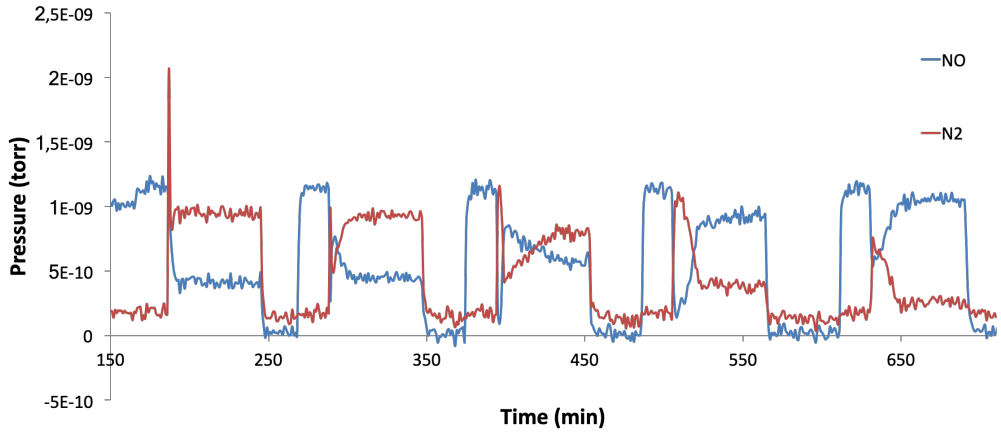

(a) H-ZSM-5 Si/Al=13.5

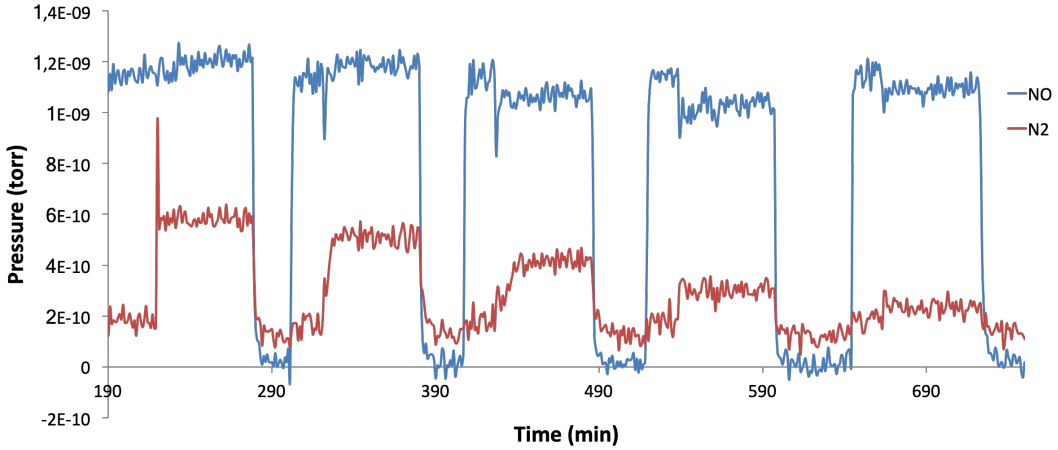

(b) C-SAPO.03

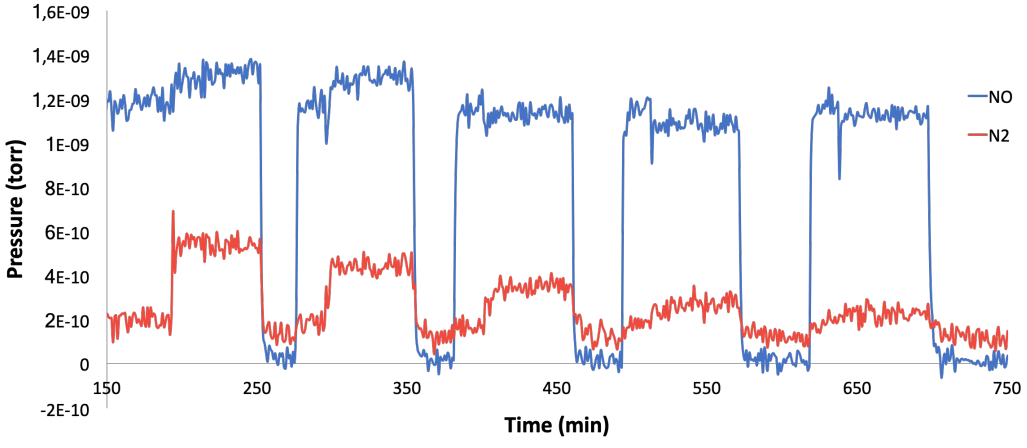

(c) hi-SAPO.03_119

Figure B.15: MS-data, pressures, during NH_3-SCR as a function of time (min) for the supports. Reaction conditions: Temperatures 450, 400, 350, 300 and 250 °C, the feed composition 600 ppm NO, 600 ppm NH_3 and 10 % O_2, 30000 mL g_{cat}^{-1} h^{-1} and 0.1 g catalysts mixed with SiC to a reactor volume of 3 mL.

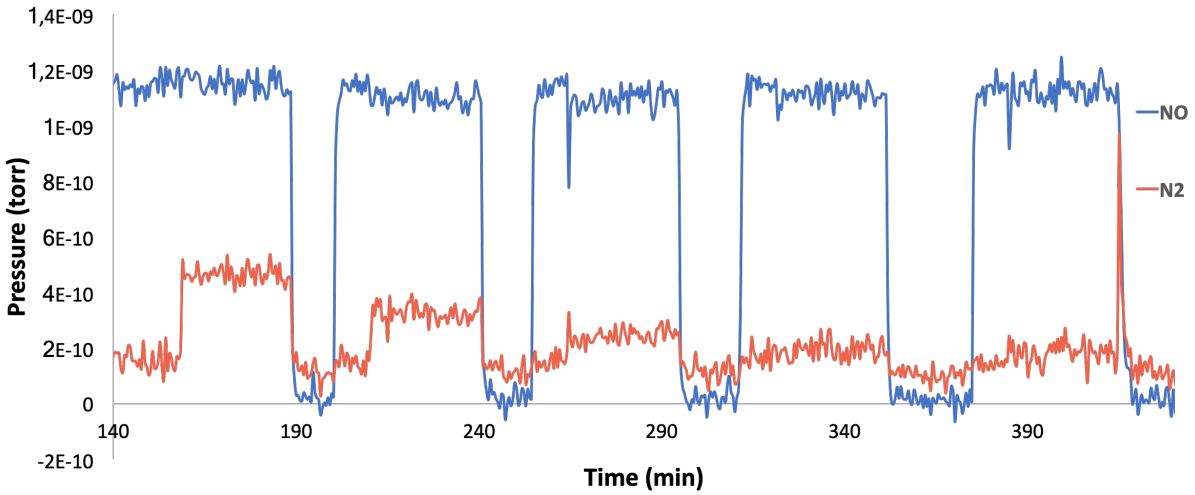

Figure B.16: MS-data for N_2 ($m/z = 28$ amu) and NO ($m/z = 30$ amu) during NH_3-SCR as a function of time (min) for the SiC. Reaction conditions: Temperatures 450, 400, 350, 300 and 250 ℃, the feed composition 600 ppm NO, 600 ppm NH_3 and 10 % O_2, 30000 mL g_{cat}^{-1} h^{-1} and 0.1 g catalysts mixed with SiC to a reactor volume of 3 mL.

B.7 Pictures of samples

(a) Impregnated: FeZ.W_13.5

(b) Ion-exchanged: FeZ.IEn_13.5

Figure B.17: Pictures showing the color difference between an impregnated catalyst and an ion-exchanged catalyst.

Appendix C

Calculations

C.1 Si/Al-ratio

An example of a Si/Al-ratio calculation is shown in this section. The following is the calculation of the sample FeZ.IEn_13.5.

Loading (wt.%) found from ICP-MS (Table B.1) and the molar mass (M) are listed in the following:

	wt.% [%]	M [g mol^{-1}] [45]
Al	3.17	26.98
Si	43.82	28.09

The Si/Al-ratio was calculated by

$$Si/Al = \frac{m_{Si}}{M_{Si}} / \frac{m_{Al}}{M_{Al}} = \frac{0.4382\text{g}}{28.09\text{g mol}^{-1}} / \frac{0.0317\text{g}}{26.98\text{g mol}^{-1}} = 13.3 \tag{C.1.1}$$

C.2 Dispersion

An example of a dispersion calculation (Equation 2.4.8) is shown in the following section. The dispersion results listed in this thesis were collected from the data report given by the chemisorption analysis.

The following is the calculation for the sample FeZ.IEn_13.5. The Fe loading was 1.05 (wt.%), $v_m/m = 0.8\ \mathrm{cm^3\,g^{-1}}$ (difference, sample mass = 0.1921g) and the molar mass of Fe = $55.85\ \mathrm{g\,mol^{-1}}$ [45]. The stoichiometry constant was assumed equal 2.

$$D = \frac{v_m/m\ s\ 100M}{V_M\ wt} = \frac{0.779\ \mathrm{cm^3} \cdot 2 \cdot 100 \cdot 55.854\ \mathrm{g\,mol^{-1}}}{22414\ \mathrm{cm^3\,mol^{-1}} \cdot 1.05} = 0.379 = 38\ \% \qquad \text{(C.2.1)}$$

C.3 NO-conversion calculations

Description of the analyses of the MS-data collected from NH_3-SCR measurements are described in the following section. ExCel is used to calculate and plot the results. It is explained how the NO-conversion is calculated, and as example is the sample FeZ.IE_13.5 chosen and the dispersion at 300 ℃ with error bars derived.

The MS-results are given as in the following:

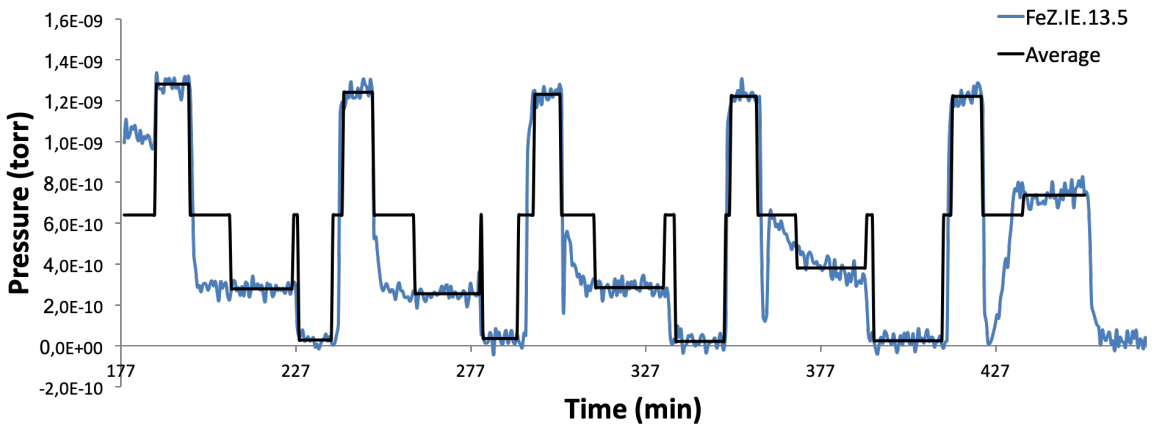

Figure C.1: Illustration NO-conversion calculation. The catalysts FeZ.IE_13.5 is shown as an example. The MS-data during NH_3-SCR is listed as a function of time, as well as the average value for different ranges in the catalytic testing.

The NO signals and the average are plotted. By average means the calculated average value of the NO signals for the relevant range. These ranges were: 0%, bypass on and the SCR reaction. Values at the mid range (6.40E-10) are NO signal not included in any

relevant range. The following figure shows the ranges zoomed in for 300 ℃:

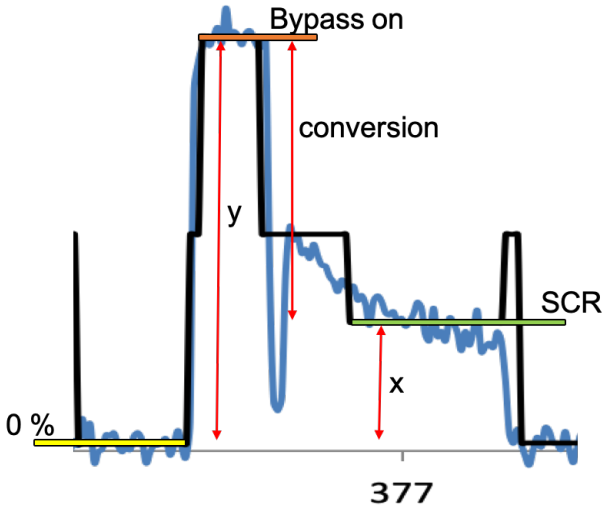

Figure C.2: Illustration of values used for calculation of the NO-conversion for a specific temperature. MS-data for FeZ.IE_13.5 at 300 ℃ is shown.

0 %:	Set as the value for zero concentration.
Bypass on:	Set as the value corresponding to the feed amount of NO.
SCR:	Set as the value corresponding to amount NO left after SCR.

The average values for the SCR range are the values after 10 minutes. It is assumed that steady-state is achieved after this. Further, it was observed approximately 0 % NO_2 signal, such that it is assumed no contribution of NO_2 for the signal for NO ($m/z = 30$ amu).

The conversion is further calculated by:

$$Conversion = (1 - \frac{x}{y}) \cdot 100\%, \tag{C.3.1}$$

where "y = average-bypass on - average-0%" and "x = average-SCR - average-0%". For this sample is the calculation as followed:

$$y = 1.22 \cdot 10^{-09} \quad - \quad 2.22 \cdot 10^{-11} = 1.20 \cdot 10^{-09} \tag{C.3.2}$$

$$x = 3.81 \cdot 10^{-10} \quad - \quad 2.22 \cdot 10^{-11} = 3.59 \cdot 10^{-10} \tag{C.3.3}$$

$$Conversion = (1 - \frac{3.59 \cdot 10^{-10}}{1.20 \cdot 10^{-09}}) \cdot 100\% = 70\% \tag{C.3.4}$$

Uncertainty of the measurements: Error bars

The final conversion plots shown in Figure 4.12 are plotted with errors bars. These error

bars are based on the standard deviation on the SCR-average, as MS-values indicate most deviation for these values. This is illustrated in the following:

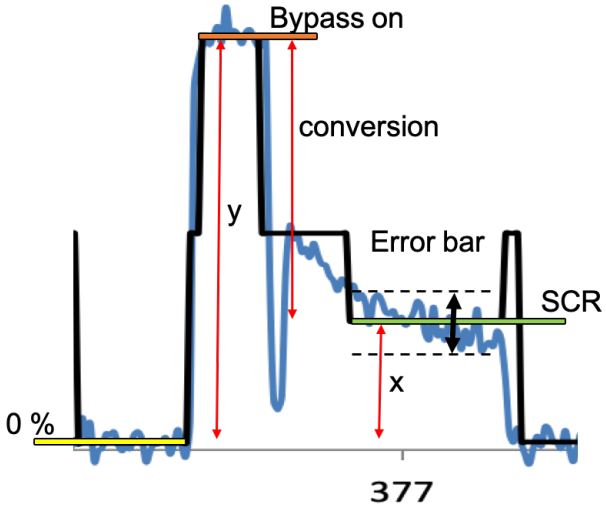

Figure C.3: Illustration of values used for calculation of the NO-conversion for a specific temperature with **the error bar shown**. MS-data for FeZ.IE_13.5 at 300 ℃ is shown.

For this example, the standard deviation of the "SCR-range" is equal 5.36E-11. This is then converted to "conversion", equal ±4.4 % NO-conversion:

$$"SCR-average" \ and \ std \ = 3.59 \cdot 10^{-10} \ + \ 5.36 \cdot 10^{-11} = 4.13 \cdot 10^{-10} \tag{C.3.5}$$

$$Conversion(SCR + std) = (1 - \frac{4.13 \cdot 10^{-10}}{1.20 \cdot 10^{-09}}) \cdot 100\% = 65.6 \ \% \tag{C.3.6}$$

$$Conversion(std) = 70 \ \% \ - \ 65.6 \ \% = 4.4 \ \% \tag{C.3.7}$$

This results in the NO-conversion for FeZ.IE_13.5 at 300 ℃ is: 70 ± 4.4 %.

C.4 Calculation Incipient Wetness Impregnation

Calculations: synthesis 5(wt%)/ZSM-5 incipient wetness impregnation

Pore volume test: result a [mL/g(ZSM-5)]

V(pore)=a*m(ZSM-5)

Amount Fe(NO3)3x9H20 (weight measured):

m = n(Fe3+)*Mm(Fe(NO3)3x9H20)=1/19*m(ZSM-5)*(1/Mm(Fe)*Mm(Fe(NO3)3x9H20)

m: 0,380753118 *m(ZSM-5)

Sample	Dilute	a [mL/g(ZSM-5)]	m(ZSM-5) [g]	V(pore) [mL]	m(ZSM-5) [g]	m(Fe(NO3)3x9H20) [g]: Theoretical	m(Fe(NO3)3x9H20) [g]: Measured
H-ZSM-5 Si/Al=30	water	1	4,9825	4,9825	4,9825	1,8971	1,9238
H-ZSM-5 Si/Al=280	water	0,75	6,1906	4,6430	6,1906	2,3571	2,3570
H-ZSM-5 Si/Al=13,5	50 vol% methanol	2,063	4,4609	9,2028	4,4609	1,6985	1,7000
		(poretest)	(choose)		(choose)		(weight measured)

	Mm. [g/mol]	
Fe	55,845	https://pubchem.ncbi.nlm.nih.gov/compound/iron#section=Top
Fe(NO3)3x9H20	404,00	https://www.sigmaaldrich.com/catalog/product/aldrich/529303?lang=en&region=NO

Figure C.4: Calculation for the incipient wetness impregnation preparation.

C.5 Mass Flow Control Calibration

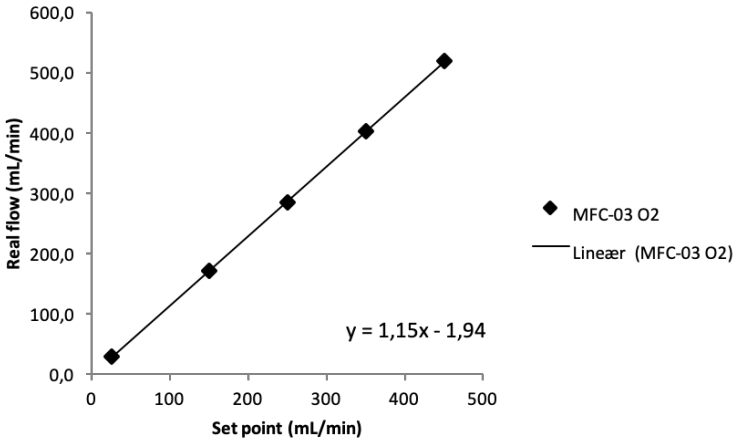

(a) O_2: MFC-03

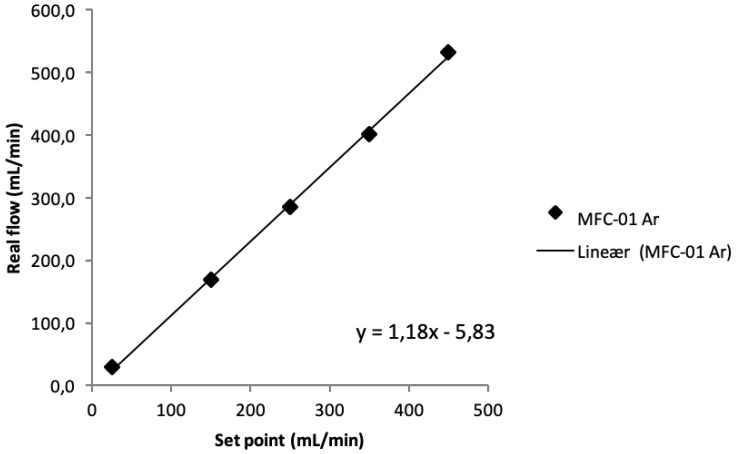

(b) Ar: MFC-01

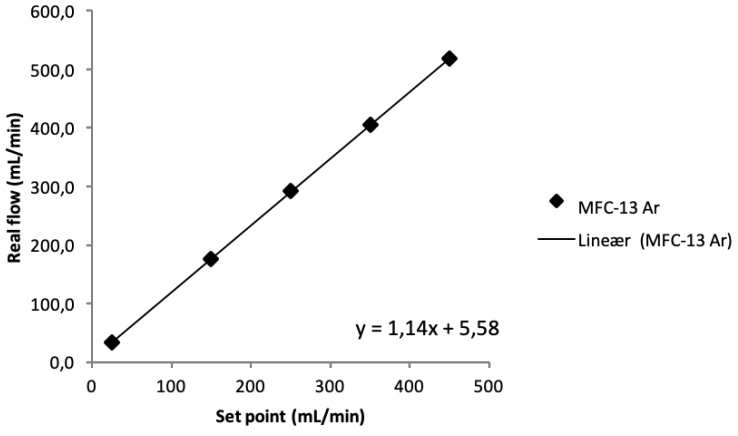

(c) Ar: MFC-13

Figure C.5: Mass flow control calibration curve for O_2, MFC-03, and two for Argon, MFC-01 and MFC-13. Maximum flow set point is 500 mL/min. A bubble column are used.

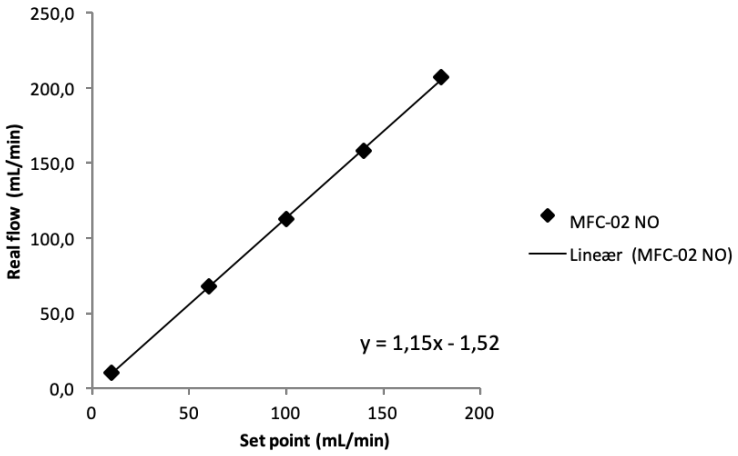

(a) NO: MFC-02

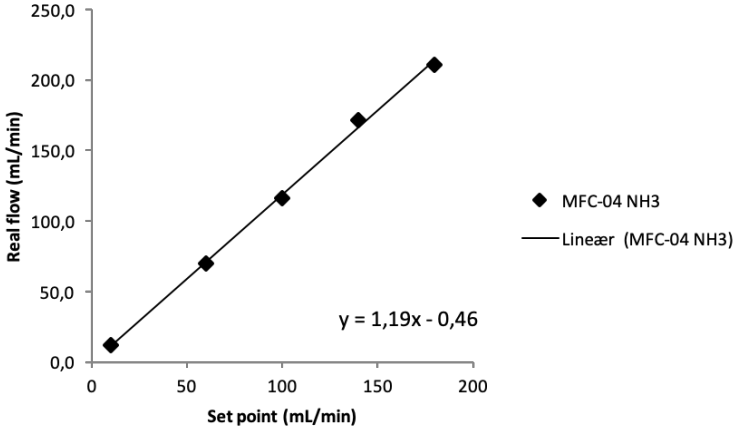

(b) NH_3: MFC-04

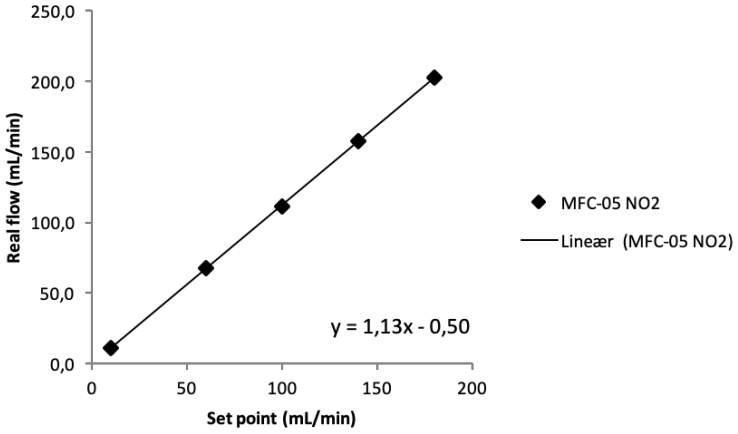

(c) NO_2: MFC-05

Figure C.6: Mass flow control calibration curve for NO, MFC-02, NH_3, MFC-04 and NO_2, MFC-05. Maximum flow set point is 200 mL/min. A bubble column are used.